



Universidade de Aveiro Departamento de Química
2018

**CAMILLE
MARIE
MONGIS**

TERMÓMETROS FOTOLUMINESCENTES BASEADOS EM LANTANOSSILICATOS

PHOTOLUMINESCENT THERMOMETERS BASED ON LANTHANIDE SILICATES

Dissertação apresentada à Universidade de Aveiro para cumprimento dos requisitos necessários à obtenção do grau de Mestrado em Química/ Functionalized Advanced Materials and Engineering (FAME), realizada sob a orientação científica do Doutor João Carlos Matias Celestino Gomes da Rocha, Professor Catedrático do Departamento de Química da Universidade de Aveiro, e Duarte Ananias Marques, Investigador de pós-doutoramento do Departamento de Química da Universidade de Aveiro.

o júri

presidente

Prof. Doutor João Rocha

professor Catedrático do Departamento de Química da Universidade de Aveiro

Prof. Doutor Luís Carlos

professor Catedrático do Departamento de física da Universidade de Aveiro

Prof. Doutora Ana Timmons

Professora auxiliar do Departamento de Química da Universidade de Aveiro

agradecimentos

Quero expressar a minha gratidão ao Prof. João Rocha e ao Doutor Duarte Ananias pela supervisão desta tese de mestrado e por todas as discussões úteis.

Desejo, também, agradecer ao apoio no uso de métodos de caracterização no departamento de Química dado pela Doutora Maria do Rosário Teixeira Soares (XRD), Dra. Maria Celeste Coimbra Azevedo (FTIR e Raman) e Doutora Paula Cristina Ramos Soares e Santos (NMR).

Devo, também, agradecer o financiamento dado pelo programa Erasmus Mundus no quadro do mestrado europeu FAME (Functionalized Advanced Materials and Engineering).

Finalmente, gostaria de agradecer à minha amiga Anna Andreykanich o grande apoio que deu à realização da minha tese de mestrado.

palavras-chave

lantanosilicatos, fotoluminescência, termômetro, transferência de energia, europium, terbium, yttrium, erbium

resumo

A síntese hidrotérmica e a caracterização estrutural de silicatos de lantanídeo, NaLnSiO_4 ($\text{Ln} = \text{Gd}^{3+}, \text{Eu}^{3+}, \text{Tb}^{3+}, \text{Y}^{3+}, \text{Er}^{3+}$ e Yb^{3+}), são relatadas. A pureza cristalina destes sólidos foi analisada por difracção de raios-X de pó e adicionalmente caracterizados por microscopia electrónica de varrimento, RNM de ^{29}Si MAS e espectroscopias de infravermelho, Raman e de fotoluminescência. Após a determinação dos melhores parâmetros de síntese para a obtenção dos compostos, avaliou-se a adequabilidade dos compostos $\text{NaGd}_{1-x-y}\text{Eu}_x\text{Tb}_y\text{SiO}_4$ e $\text{Na}[(\text{Gd}_{0.85}\text{Yb}_{0.10}\text{Er}_{0.05})\text{SiO}_4]$ para actuarem como termómetros raciométricos fotoluminescentes (Eu^{3+} e Tb^{3+} são emissores visíveis, e Er^{3+} e Yb^{3+} são emissores infravermelhos). As transferências de energia entre do Tb^{3+} para o Eu^{3+} e do Yb^{3+} para o Er^{3+} foram detectadas, as quais levam a uma dependência com a temperatura dos rácios entre as transições $^5\text{D}_4 \rightarrow ^7\text{F}_2$ (Tb^{3+}) e $^5\text{D}_0 \rightarrow ^7\text{F}_2$ (Eu^{3+}) para $\text{NaGd}_{1-x-y}\text{Eu}_x\text{Tb}_y\text{SiO}_4$ e entre as transições $^2\text{F}_{5/2} \rightarrow ^2\text{F}_{7/2}$ (Yb^{3+}) e $^4\text{I}_{13/2} \rightarrow ^4\text{I}_{15/2}$ (Er^{3+}) para $\text{Na}[(\text{Gd}_{0.85}\text{Yb}_{0.10}\text{Er}_{0.05})\text{SiO}_4]$. Esses rácios permitem determinar a sensibilidade dos compostos para actuar como termómetros. A temperaturas criogénicas, a sensibilidade obtida depende dos parâmetros de composição x e y para $\text{NaGd}_{1-x-y}\text{Eu}_x\text{Tb}_y\text{SiO}_4$. O termómetro raciométrico luminescente no infravermelho, $\text{Na}[(\text{Gd}_{0.85}\text{Yb}_{0.10}\text{Er}_{0.05})\text{SiO}_4]$, apresenta o melhor desempenho em termos de sensibilidade.

keywords

Lanthanide silicate, photoluminescence, thermometer, energy transfer, europium, terbium, yttrium, erbium

abstract

The hydrothermal synthesis and structural characterization of lanthanide silicates NaLnSiO_4 , $\text{Ln} = \text{Gd}^{3+}$, Eu^{3+} , Tb^{3+} , Er^{3+} and Yb^{3+} are reported. The crystal phase purity of these solid was analysed by powder X-ray diffraction and further characterized by scanning electron microscopy, ^{29}Si MAS NMR, Infra-Red, Raman and photoluminescence spectroscopy. After having determined the best synthesis parameters to obtain the compounds, the suitability of the compounds $\text{NaGd}_{1-x-y}\text{Eu}_x\text{Tb}_y\text{SiO}_4$ and $\text{Na}[(\text{Gd}_{0.85}\text{Yb}_{0.10}\text{Er}_{0.05})\text{SiO}_4]$ to act as ratiometric photoluminescent thermometers was assessed (Eu^{3+} and Tb^{3+} are visible emitters, and Er^{3+} and Yb^{3+} infra-red emitters). The Tb^{3+} to Eu^{3+} and Yb^{3+} to Er^{3+} energy transfers were detected, leading to a temperature dependence of the emission ratio between the $\text{Tb}^{3+} {}^5\text{D}_4 \rightarrow {}^7\text{F}_{5-0}$ and $\text{Eu}^{3+} {}^5\text{D}_0 \rightarrow {}^7\text{F}_{0-4}$ transitions for $\text{NaGd}_{1-x-y}\text{Eu}_x\text{Tb}_y\text{SiO}_4$ and between $\text{Yb}^{3+} {}^2\text{F}_{5/2} \rightarrow {}^2\text{F}_{7/2}$ and $\text{Er}^{3+} {}^4\text{I}_{13/2} \rightarrow {}^4\text{I}_{15/2}$ transitions for $\text{Na}[(\text{Gd}_{0.85}\text{Yb}_{0.10}\text{Er}_{0.05})\text{SiO}_4]$. This ratio allows the determining the sensitivity of the compounds to act as thermometers. At cryogenic temperatures, the sensitivity obtained depends on the composition parameters x and y for $\text{Na}[(\text{Gd}_{0.85}\text{Yb}_{0.10}\text{Er}_{0.05})\text{SiO}_4]$. The infrared ratiometric luminescent thermometer $\text{NaGd}_{1-x-y}\text{Er}_x\text{Yb}_y\text{SiO}_4$ presents the best performance in terms of sensitivity.

TABLE OF CONTENT

I-INTRODUCTION	1
1.1 LANTHANIDE PHOTOLUMINESCENCE.....	2
1.1.1 Basics of photoluminescence	2
1.1.2 Lanthanide ions	3
1.1.3 Sensitized luminescence	5
1.1.4 Charge transfer.....	5
1.2 STRUCTURE AND SYNTHESIS	6
1.2.1 Zeolites	6
1.2.2 Lanthanide silicates	8
1.2.3 Zeolite synthesis.....	9
1.2.4 Lanthanide silicates synthesis	9
1.3 THERMOMETRY AND LANTHANIDE SILICATES.....	10
1.3.1 Luminescent thermometry	10
1.3.2 Parameters of a ratiometric luminescent thermometer	11
1.4 STATE-OF-THE-ART OF LANTHANIDE LUMINESCENT THERMOMETRY	12
II Experimental part.....	15
2.1 AIM OF STUDY	15
2.2 SYNTHESIS	16
2.3 INSTRUMENTATION	16
2.3.1 Powder X-Ray diffraction	16
2.3.2 Scanning Electron Microscopy	16
2.3.3 Raman spectroscopy	16
2.3.4 Infra-red spectroscopy	17
2.3.5 Photoluminescence spectroscopy.....	17
2.3.6 NMR spectroscopy	17
III Results and discussion.....	19
3.1 SYNTHESIS PARAMETERS VARIATION.....	19
3.1.1- Temperature variation	19
3.1.2- Time variation	22
3.1.3- Lanthanide: Silicon ratio	23
3.1.4- Silicate:sodium ratio	25
3.1.5- Na[LnSiO ₄] with Ln = Gd, Eu, Tb	27

3.1.6- Na[LnSiO ₄] with Ln = Gd, Er, Yb	29
3.1.7- NaYSiO ₄	30
3.2 RAMAN AND INFRARED SPECTROSCOPIES	32
3.2.1- Raman spectroscopy	32
3.2.2- Infrared spectroscopy	33
3.3 NMR SPECTROSCOPY	33
3.4 PHOTOLUMINESCENCE CHARACTERIZATION	34
3.4.1 Photoluminescence characterization of NaGd _{0,9} Eu _{0,1} SiO ₄ , NaGd _{0,5} Eu _{0,5} SiO ₄ , NaEuSiO ₄ and NaGd _{0,9} Tb _{0,1} SiO ₄	34
3.4.2 Visible ratiometric luminescent thermometers	42
3.4.3 Infrared ratiometric luminescent thermometer	50
IV Conclusion.....	55
V Bibliography	57
VI Annexes.....	59
6.1 CRYSTAL DATA.....	59
6.2 SYNTHESIS	59

INDEX OF FIGURES

Figure 1: Scheme representing the ground state and an excited energy state of an entity. The transition R corresponds to a radiative emission and NR to a non-radiative.	1
Figure 2 : Electronic configuration of a singlet ground state, singlet excited state and triplet excited state.	3
Figure 4: Energy level diagram of the 4f orbitals of trivalent lanthanide ions [8].	4
Figure 5: Mechanisms of energy transfer from the ligand to the lanthanide ion (S0: singlet ground state; S1: singlet excited state; T1: triplet excited state; ISC: intersystem crossing; ET: energy transfer).....	5
Figure 6: Typical structure of zeolites.	7
Figure 7: Crystal structure of ETS-10. Titanium oxide chains are represented by orange rods and siliceous matrix with corner-shared $[\text{SiO}_4]^{4-}$ units is depicted in blue (oxygen atoms have been omitted for clarity) [8].	7
.....	13
Figure 8: Temperature dependence of $\text{Na}[(\text{Gd}_{0.99}\text{Eu}_{0.01})\text{SiO}_4]$ emission spectra in the $^5\text{D}_0 \rightarrow ^7\text{F}_1$ transition region [25].	13
Figure 9: Emission spectra of $\text{Na}[(\text{Gd}_{0.8}\text{Eu}_{0.1}\text{Tb}_{0.1})\text{SiO}_4]$ under 483.5 Tb^{3+} excitation [25].	14
Figure 10: Crystalline structure of NaGdSiO_4 showing the tetrameric units of hexacoordinated Gd^{3+} [28].	15
Figure 11 : Experimental and simulated powder XRD patterns of the sample synthesized at 245 °C and of tetragonal NaGdSiO_4 (ICSD 16188) [29].	20
Figure 12: Powder XRD patterns of samples prepared at the oven temperatures depicted.	20
Figure 13: SEM and STEM images of the compounds synthesized at different temperatures.	21
Figure 15: SEM and STEM images of the compounds synthesized at different times.	23
Figure 16 : Powder XRD patterns of samples with different Ln:Si ratios. (*) depict impurities.	24
Figure 17: SEM images of the compounds with a Si:Ln ratio of 5:1, 4:1 and 1:4.	25
Figure 18 : Powder XRD patterns of samples prepared with different Si:Na ratios. (*) depicts impurities.	26
Figure 19: SEM images of the compounds with a Si:Na ratio of 1:14, 1:10, 1:9.	27
Figure 20: Powder XRD patterns of samples prepared with the indicated Gd:Eu:Tb ratios.	28
Figure 21: SEM images of $\text{NaGd}_{0.80}\text{Tb}_{0.15}\text{Eu}_{0.05}\text{SiO}_4$ and $\text{NaGd}_{0.80}\text{Tb}_{0.167}\text{Eu}_{0.033}\text{SiO}_4$	28
Figure 22: Powder XRD patterns of $\text{Na}[\text{LnSiO}_4]$ with Ln = Gd, Er, Yb samples with Si:Ln ratio of 2:1. (*) depicts an impurity.	29
Figure 23 : SEM images of the $\text{Na}[\text{LnSiO}_4]$ with Ln = Gd, Er, Yb.	30
Figure 24 : Powder XRD patterns of $\text{NaYSiO}_4/1^{\text{st}}$ for the first synthesis and $\text{NaYSiO}_4/2^{\text{nd}}$ for the second synthesis. The simulated pattern of tetragonal NaGdSiO_4 is also shown (ICSD 16188) [29].	31

Figure 25: SEM images of NaYSiO ₄	31
Figure 26 : Raman spectra of Na[(Gd _{0.84} Tb _{0.12} Eu _{0.04})SiO ₄], of Na[(Gd _{0.80} Tb _{0.15} Eu _{0.05})SiO ₄], of Na[(Gd _{0.80} Tb _{0.167} Eu _{0.033})SiO ₄] and of Na[(Gd _{0.85} Tb _{0.10} Eu _{0.05})SiO ₄].	32
Figure 27: Infrared spectra of Na[(Gd _{0.80} Tb _{0.15} Eu _{0.05})SiO ₄], Na[(Gd _{0.80} Tb _{0.167} Eu _{0.033})SiO ₄], Na[(Gd _{0.85} Tb _{0.10} Eu _{0.05})SiO ₄] and Na[(Gd _{0.80} Tb _{0.16} Er _{0.04})SiO ₄].....	33
Figure 28: ²⁹ Si MAS NMR spectrum of NaYSiO ₄	34
Figure 29: Excitation spectra of NaGd _{0.9} Eu _{0.1} SiO ₄ (λ _{Em} =614.5 nm) recorded at room temperature (black line) and 12 K (red line).....	35
Figure 30 : Emission spectra of NaGd _{0.9} Eu _{0.1} SiO ₄ (λ _{Ext.} = 394 nm) recorded 294 K (black) and 12K (red).....	36
Figure 31 : ⁵ D ₀ decay curves of NaGd _{0.9} Eu _{0.1} SiO ₄ recorded at 294 K (black) and 12 K (red) with excitation at 394 nm and emission at 614.5 nm. The solid lines are the best fits to a first order exponential decay functions ($I = I_0 + A_1 e^{-x/\tau}$).....	36
Figure 32: Excitation spectra of NaGd _{0.9} Eu _{0.1} SiO ₄ (green line), NaGd _{0.5} Eu _{0.50} SiO ₄ (red line) and NaEuSiO ₄ (blue line) (λ _{Em} =614.5 nm).....	37
Figure 33: Emission spectra of NaGd _{0.9} Eu _{0.1} SiO ₄ (green line), NaGd _{0.5} Eu _{0.50} SiO ₄ (red) and NaEuSiO ₄ (blue) (λ _{Em} =394 nm).....	38
Figure 34 : ⁵ D ₀ decay curves of NaGd _{0.9} Eu _{0.1} SiO ₄ (green), NaGd _{0.5} Eu _{0.50} SiO ₄ (red) and NaEuSiO ₄ (blue) recorded at 294 K, with excitation at 394 nm and emission at 614.5 nm. The solid lines are the best fits to first order ($I = I_0 + A_1 e^{-x/\tau}$) and second-order ($I = I_0 + A_1 e^{-x/\tau} + A_2 e^{-x/\tau_2}$) decay functions. The average lifetime is defined as $(A_1\tau_1 + A_2\tau_2)/(A_1 + A_2)$	39
Figure 35: Photographs, from left to right, NaGd _{0.90} Eu _{0.10} SiO ₄ , NaGd _{0.50} Eu _{0.50} SiO ₄ and NaEuSiO ₄ luminescence under an excitation wavelength of 254 nm.	39
Figure 36: Excitation spectra of NaGd _{0.9} Tb _{0.1} SiO ₄ (λ _{Em} =543.5 nm) recorded at room temperature (black line) and 12 K (red line).....	40
Figure 37: Emission spectra of NaGd _{0.9} Tb _{0.1} SiO ₄ (λ _{Ext.} = 375 nm) recorded at 294 K (black line) and 12 K (red line). The inset depicts, a photograph of NaGd _{0.9} Tb _{0.1} SiO ₄ under 254 nm irradiation.	41
Figure 38 : ⁵ D ₄ decay curves of NaGd _{0.9} Tb _{0.1} SiO ₄ recorded at 294K (black) and 12K (red) with excitation at 375 nm and emission at 543.5 nm. The solid lines are the best fits to first-order exponential functions ($I = I_0 + A_1 e^{-x/\tau}$).	41
Figure 39: Room-temperature emission spectra of compounds NaLnSiO ₄ with Ln=Gd, Tb, Eu, under excitation at 368 nm.....	42
Figure 40: Photographs, from left to right, NaGd _{0.90} Eu _{0.10} SiO ₄ , NaGd _{0.82} Tb _{0.09} Eu _{0.09} SiO ₄ , NaGd _{0.82} Tb _{0.135} Eu _{0.045} SiO ₄ and NaGd _{0.90} Tb _{0.10} SiO ₄ luminescence under an excitation wavelength of 254 nm.	43
Figure 41: Excitation spectra of Na[(Gd _{0.82} Tb _{0.135} Eu _{0.045})SiO ₄] at 294 K (black lines) and 12 K (red lines) with the emission fixed at 614.5 nm (bottom) and 543.5 nm (top).....	44

Figure 42: a) Emission spectra of $\text{Na}[(\text{Gd}_{0.666}\text{Tb}_{0.292}\text{Eu}_{0.042})\text{SiO}_4]$ in the range 12 – 410 K with the excitation fixed at 375 nm. b) Emission spectra of $\text{Na}[(\text{Gd}_{0.82}\text{Tb}_{0.135}\text{Eu}_{0.045})\text{SiO}_4]$ in the range 12 – 450 K with the excitation fixed at 375 nm.	45
Fig. 43 - Temperature dependence of the I_{Tb} (green) and I_{Eu} (red) parameters of $\text{Na}[(\text{Gd}_{0.666}\text{Tb}_{0.292}\text{Eu}_{0.042})\text{SiO}_4]$ in the range 12K-410K (a) and $\text{Na}[(\text{Gd}_{0.82}\text{Tb}_{0.135}\text{Eu}_{0.045})\text{SiO}_4]$ in the range 12 – 450 K (b)	46
Figure 44: Temperature dependence of the parameter Δ from 12 K to 410 K for $\text{Na}[(\text{Gd}_{0.666}\text{Tb}_{0.292}\text{Eu}_{0.042})\text{SiO}_4]$ (a) and from 12 K to 450 K for $\text{Na}[(\text{Gd}_{0.82}\text{Tb}_{0.135}\text{Eu}_{0.045})\text{SiO}_4]$ (b) excited at 375nm. The solid lines are the calibration curves resulting from the fits considering a Mott-Seitz model.	47
Figure 45: Relative thermal sensitivities from 12 K to 410 K for $\text{Na}[(\text{Gd}_{0.666}\text{Tb}_{0.292}\text{Eu}_{0.042})\text{SiO}_4]$ (a) and from 12 K to 450 K for $\text{Na}[(\text{Gd}_{0.82}\text{Tb}_{0.135}\text{Eu}_{0.045})\text{SiO}_4]$ (b).	48
Figure 46: Decay curves of $\text{Na}[(\text{Gd}_{0.666}\text{Tb}_{0.292}\text{Eu}_{0.042})\text{SiO}_4]$ recorded at 543 nm (a), $^5\text{D}_4$ decay, and 614nm (b), $^5\text{D}_0$ decay, with a fixed excitation at 375 nm. The black curves were measured at 12 K while the red ones at 294 K. The lines are best fits to first-order ($I = I_0 + A1e^{-x/\tau}$) and second-order ($I = I_0 + A1e^{-x/\tau} + A2e^{-x/\tau}$) decay functions. Average lifetime defined as $(A1\tau_1 + A2\tau_2)/(A1 + A2)$	49
Figure 47: Decay curves of $\text{Na}[(\text{Gd}_{0.82}\text{Tb}_{0.135}\text{Eu}_{0.045})\text{SiO}_4]$ recorded at 543 nm (a), $^5\text{D}_4$ decay, and 614 nm (b), $^5\text{D}_0$ decay, with a fixed excitation at 375 nm. The black curves are the decay measured at 12 K while the red ones at 294 K. The lines are best fits to first-order ($I = I_0 + A1e^{-x/\tau}$) and second-order ($I = I_0 + A1e^{-x/\tau} + A2e^{-x/\tau}$) decay functions. Average lifetime defined as $(A1\tau_1 + A2\tau_2)/(A1 + A2)$	49
Figure 48: Excitation spectra of $\text{Na}[(\text{Gd}_{0.85}\text{Yb}_{0.10}\text{Er}_{0.05})\text{SiO}_4]$ at 294 K (black) and 12 K (red) with the emission fixed at 1520 nm.	51
Figure 49: Emission spectra of $\text{Na}[(\text{Gd}_{0.85}\text{Yb}_{0.10}\text{Er}_{0.05})\text{SiO}_4]$ at 294 K (black) and 12 K (red) with the excitation fixed at 961 nm.	51
Figure 50: Emission spectra of $\text{Na}[(\text{Gd}_{0.85}\text{Yb}_{0.10}\text{Er}_{0.05})\text{SiO}_4]$ in the range 12 – 390 K with the excitation fixed at 916 nm.	52
Figure 51: Temperature dependence of the I_{Yb} (red) and I_{Er} (green) parameters of $\text{Na}[(\text{Gd}_{0.85}\text{Yb}_{0.10}\text{Er}_{0.05})\text{SiO}_4]$	53
Figure 52: a) Temperature dependence of the parameter Δ from 12K to 390K for $\text{Na}[(\text{Gd}_{0.85}\text{Yb}_{0.10}\text{Er}_{0.05})\text{SiO}_4]$ excited at 916 nm. The solid line is the calibration curve, resulting from the fit considering a Mott-Seitz model. b) Corresponding relative thermal sensitivity in the same temperature range.	53

INDEX OF TABLES

Table 2: Representative cryogenic luminescent ratiometric thermometers; S_m is the maximum relative sensitivity at temperature T_m . ΔT is the temperature range with a relative sensitivity $S_r > 1.0 \%K^{-1}$ for a specified temperature range [36].	47
Table A1: Synthesis conditions of the compounds synthesized at different temperatures.	59
Table A2: Synthesis conditions of the compounds synthesized with different oven times.	59
Table A3: Synthesis conditions of the compounds synthesized with different Si:Ln ratios.	60
Table A4: Synthesis conditions of the compounds synthesized with different Si:Na ratios.	60
Table A5: Synthesis conditions of the compounds synthesized with different Gd:Eu:Tb ratios.	61
Table A6: Synthesis conditions of the compounds synthesized with different Gd:Er:Yb ratios.	61
Table A7: Synthesis conditions of the compounds $NaYSiO_4$.	62

ABBREVIATIONS

ED	Electric dipole
MD	Magnetic dipole
XRD	X-Ray Diffraction
SEM	Scanning Electron Microscopy
STEM	Scanning Transmission Electron Microscopy
SSS	Sodium silicate solution

I-INTRODUCTION

Luminescence is light emission not produced by heating. It is a process that can be observed in daily life, for example in neon or fluorescent light, television, in living matter such as fireflies or glow-worms. It can also be seen in natural phenomena such as aurora borealis.

In luminescence, the light emission occurs after the absorption of energy by an optically active entity from its environment, for example from radiation or chemical reaction, but there are numerous different excitation sources. Absorbing this external energy will lift the atom (or molecule) into an excited state but due to the instability of the excited states, the entity undergoes a transition back to the ground state. This transition is only possible by reemitting energy, either as heat, non-radiative emission, or as light, radiative emission, i.e., luminescence (Fig. 1).

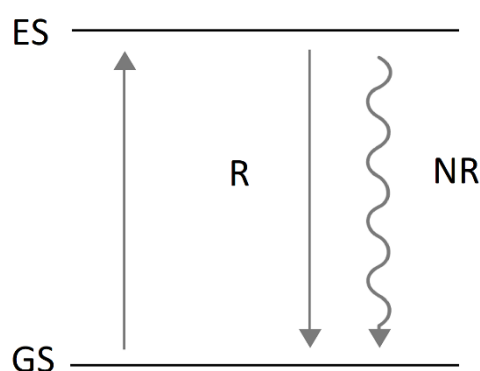


Figure 1: Scheme representing the ground state and an excited energy state of an entity. The transition R corresponds to a radiative emission and NR to a non-radiative.

Each different excitation source leads to a different kind of luminescence, such as photoluminescence, cathodoluminescence, chemiluminescence, electroluminescence and thermoluminescence.

This study will focus on photoluminescence, which is caused by the absorption of electromagnetic radiation that can range from gamma radiation to infrared light. In the case of down-conversion photoluminescence, the emitted light is nearly always of equal or lower energy than the absorbed light, thus leading to an equal or higher wavelength of light emission. This loss of energy is due to the non-radiative emission of the absorbed light. However, in the so-called up-conversion process, emitted light of higher energy can be observed, for instance, visible light generated by intense infrared irradiation by a LASER beam.

The bright red colour of the ruby, crystalline α -alumina doped with chromium ($\text{Al}_2\text{O}_3:\text{Cr}^{3+}$), is partially explained by fluorescence. The introduction of Cr^{3+} ions into the colourless Al_2O_3 crystal structure

originates absorption in the ultraviolet, violet, and yellow-green regions of the spectrum. Additionally, absorption at any of the above wavelengths stimulates the Cr^{3+} red emission at 694 nm, which intensify the perceived deep red colour of the ruby [1].

Like chromium in ruby, the photoluminescence is originated from ions or molecules that are light sensitive, absorbing higher energy light than the emitted one. Those ions must have an energy gap fitting with the photon's energy of the light, to be able to be excited by it before emitting back through a radiative process. The most common ones are the transition metal and rare-earth ions. They have already proved their capacity and large range of emission in photoluminescent materials [2]–[4].

Lanthanide ions show unusual electronic properties due to their incomplete f orbitals, making them perfect for photoluminescence, their exceptional luminescence features are already used in many applications like phosphors or optical amplifiers. An optical amplifier is a device that amplifies an optical signal without the need to first convert it to an electrical signal, they are useful to transmit signals over long distances since it decreased the attenuation losses, the most used is an erbium-doped fibre amplifier [5].

Lanthanide ions show potential in other sectors, particularly in luminescent thermometry. Their optical properties can be used in nonintrusive thermometers, the medium is observed remotely, based on changes in the emission intensity upon temperature variation.

Nowadays, thermometer measurements are accomplished with heat flow to an invasive probe, which makes all those thermometer measurement instruments unsuitable for measuring fast-moving, or microscale object [6]. However, accurate and non-invasive temperature measurements with submicrometric resolution are necessary to understand the working processes, such as thermal transport, heat transfer or dissipation of micro and nanoscale electronic or photonic devices. In the medical field, determining the temperature of a living cell would be a huge help to analyse its pathology or physiology, especially of cancer cells, since their temperatures are higher than healthy cells.

Using Ln^{3+} ions may lead to a non-contact thermometry technique through an optical detection system by analysing the variation of the luminescence intensities. Rare-earth silicates, including dense, layered and microporous materials, have been shown to be efficient light-emitting material. Indeed, the reported microporous Ln^{3+} silicates display unique and unusual photoluminescence. Thus, silicates and zeolites are promising matrices to host the luminescent lanthanide ions for thermometry purposes.

1.1 LANTHANIDE PHOTOLUMINESCENCE

1.1.1 Basics of photoluminescence

A photoluminescent compound, where luminescence is caused by light excitation, may exhibit fluorescence or phosphorescence. The distinction originates from the process involved in the excitation of the ground state to the emitting state of an atom or molecule. First, in the so-called singlet spin state, two electrons have a spin of opposite direction. After absorbing radiation one of the electrons of the valence band of the atom is promoted to a higher energy level, an excited state. This electron, when excited will generally keep its spin creating a singlet-excited state, but it can also change spin and thus create a triplet-excited state (Fig. 2).

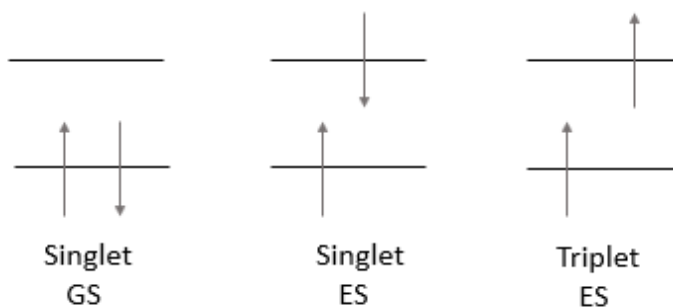


Figure 2 : Electronic configuration of a singlet ground state, singlet excited state and triplet excited state.

When the electron returns to its ground state luminescence happens. Emission from a singlet-excited state leads to fluorescence while the emission from a triplet excited state leads to phosphorescence.

Singlet excited states are short-lived, the electron rapidly loses its energy in a radiative or a non-radiative way. Non-radiative routes comprise vibrational relaxation, internal conversion or intersystem crossing. Fluorescence lifetime is generally of the order of nanoseconds.

Phosphorescence is relatively rare because the corresponding emission transition is forbidden by spin ($\Delta S=1$) while fluorescence is spin-allowed ($\Delta S=0$). It occurs when the excited molecule in the singlet excited state relax through the inter-crossing phenomena to the lower triplet excited state, it is characterized by a long lifetime ($10^3 - 10^0 \text{ s}^{-1}$) leading to the emission of light after removal of the excitation source. Heavy atoms facilitate inter-crossing, thus increase phosphorescence [7].

The use of lanthanide ions as fluorescence materials requires the non-radiative relaxation process to be reduced to a minimum to maximise the emission intensity.

1.1.2 Lanthanide ions

Lanthanide ions are characterized by an incomplete filled 4f shell. The more stable oxidation state of lanthanide ions is Ln(III), that is gradually filled from $4f^0$ (La^{3+}) to $4f^{14}$ (Lu^{3+}) (Fig 3). Thus, they have the general electronic configuration $[\text{Xe}] 4f^n$.

H																	He
Li	Be											B	C	N	O	F	Ne
Na	Mg											Al	Si	P	S	Cl	Ar
K	Ca	Sc	Ti	V	Cr	Mn	Fe	Co	Ni	Cu	Zn	Ga	Ge	As	Se	Br	Kr
Rb	Sr	Y	Zr	Nb	Mo	Tc	Ru	Rh	Pd	Ag	Cd	In	Sn	Sb	Te	I	Xe
Cs	Ba	La	Hf	Ta	W	Re	Os	Ir	Pt	Au	Hg	Tl	Pb	Bi	Po	At	Rn
Fr	Ra	Ac	Rf	Db	Sg	Bh	Hs	Mt	Ds	Rg	Cn	Nh	Fl	Mc	Lv	Ts	Og

Ce	Pr	Nd	Pm	Sm	Eu	Gd	Tb	Dy	Ho	Er	Tm	Yb	Lu
Th	Pa	U	Np	Pu	Am	Cm	Bk	Cf	Es	Fm	Md	No	Lr

Figure 3: Lanthanides in the periodic table.

Their 4f shell is surrounded by the filled $5s^2$ and $5p^6$, therefore well shielded from the surrounding environment leading to a small influence of the host lattice on the luminescence properties within the 4f configuration. Indeed, the colour of the emission depends almost solely on the lanthanide ion itself, the luminescence properties are dependent on the intraconfigurational 4f shell. Lanthanide ions exhibit luminescence in the UV domain to the visible and near IR region when excited by UV light.

Ln^{3+} ions offer a large range of colour emissions over the entire spectral range: near infrared (Nd^{3+} , Er^{3+}), red (Eu^{3+} , Pr^{3+} , Sm^{3+}), green (Er^{3+} , Tb^{3+}), blue (Tm^{3+} , Ce^{3+}) and UV region (Gd^{3+}) [1], [4].

The photoluminescence of trivalent lanthanide ions originates from 4f-4f transitions. Figure 4 shows the energy level diagram of the 4f orbitals of the most common trivalent lanthanide ions with their typical transitions emission. Their energy states are noted as $(^{2S+1})L_J$, a typical notation that will be explained later.

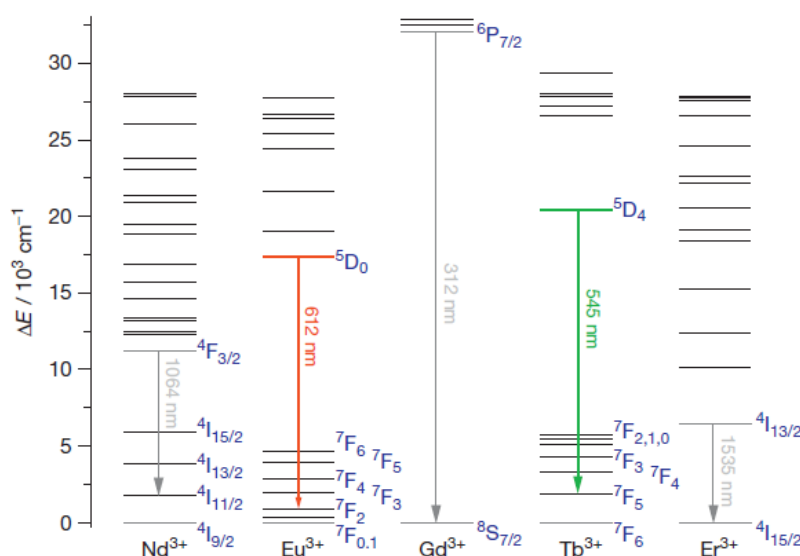


Figure 4: Energy level diagram of the 4f orbitals of trivalent lanthanide ions [8].

1.1.3 Sensitized luminescence

Luminescence intensity is proportional to the amount of light absorbed, thus it is an important aspect, especially since some lanthanide ions, like Eu^{3+} , have weak light absorption cross-sections comparing with the transition ions and organic molecules. This problem can be overcome by sensitization such as by the so-called “antenna effect”. This phenomenon is the results of a chromophore being able to absorb more light than the lanthanide ion and transferring this excitation energy to the rare earth ion through radiationless processes.

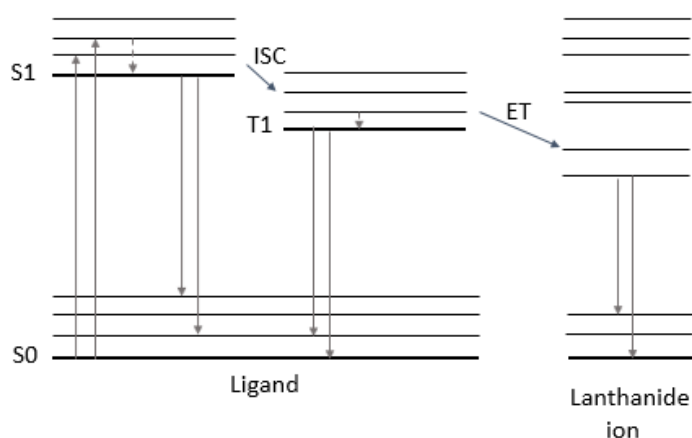


Figure 5: Mechanisms of energy transfer from the ligand to the lanthanide ion (S0: singlet ground state; S1: singlet excited state; T1: triplet excited state; ISC: intersystem crossing; ET: energy transfer).

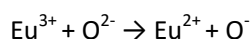
The energy transfer mechanisms are the following: the ligand is excited to a singlet state S1 by absorbing light, and next the energy is transferred to a triplet states T1 through intersystem crossing. Then, the energy of the triplet state can be transfer to a level of the lanthanide ion via an electron exchange mechanism, such as the Dexter mechanism [9] (Fig. 5) which requires the overlap between ligand and the lanthanide ion orbitals. Therefore, the energy transfer is strongly distance-dependent. In order to get an efficient energy transfer, the triplet state of the ligands should be located at least 1500 cm^{-1} above the emitting states of the lanthanide ion. If the energy difference is not large enough then back transfer can occur and the efficiency of the energy transfer will drastically decrease.

The sensitizing element can also be inorganic, such as in the Tb^{3+} -to- Eu^{3+} energy transfer, where the emission of Eu^{3+} can be strongly improved with a concomitant decrease of the Tb^{3+} emission.

1.1.4 Charge transfer

Charge transfer is another common type of transition observed with some lanthanide ions. It is also an allowed transition and, therefore, gives intense and broad spectral bands in the UV region. This transition is generally found only in lanthanides that are prone to be reduced, such as Eu^{3+} and Yb^{3+} have a tendency to become divalent, they are perfect for charge transfer transitions. While the f-d transitions are more common for ions with a tendency to oxidize, for example, Ce^{3+} , Tb^{3+} , Pr^{3+} , all trivalent ions with a propensity to become tetravalent, will show broad spectral band corresponding to f-d transitions [1].

Electron charge transfer involves the transfer of an electron from an entity to another one, in this case between a metal ion, the lanthanide, and the ligand. For example, the following transfer between the europium ion and an oxygen:



This phenomenon is responsible for the strong efficiency of the red emitting $\text{Y}_2\text{O}_3:\text{Eu}^{3+}$ material by allowing a strong absorption in the UV region.

Charge transfer can be used for sensitization of europium luminescence, they can act as an antenna to absorb the light and transfer it to the excited states of the lanthanide ion, for example in the red phosphor $\text{Y}_2\text{O}_3:\text{Eu}^{3+}$ [10], [11].

1.2 STRUCTURE AND SYNTHESIS

1.2.1 Zeolites

Zeolites are three-dimensional crystal structures, well known for their open frameworks. They are crystalline hydrated aluminosilicates made out of tetrahedral aluminium $[\text{AlO}_4]^{5-}$ units and tetrahedral silicon $[\text{SiO}_4]^{4-}$ units interconnected by the corners [8]. Thus, all oxygen atoms are shared and form intracrystalline hollow spaces or channels of molecular dimension. Those large open pores are of the size of small molecules.

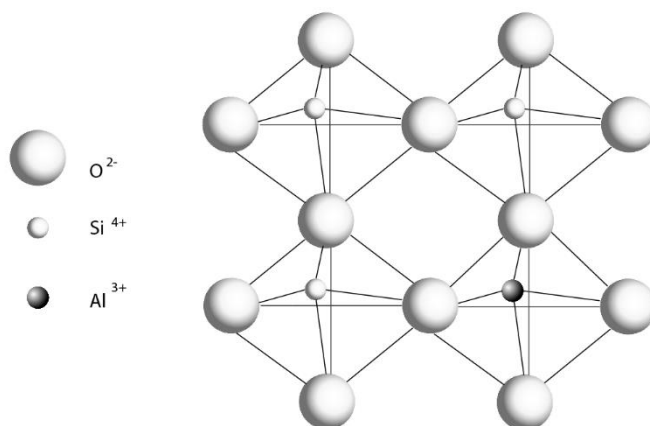


Figure 6: Typical structure of zeolites.

There are around 40 natural zeolites and dozens more artificial materials, presenting attractive properties. They are very stable, resisting challenging conditions, have a high melting point, over 1000 °C, resist high pressure, do not dissolve in water or other inorganic solvents, and do not oxidize in the air.

Due to their high stability, their attractiveness relies on the porous character, which allows trapping and separating molecules. The negative charge of the zeolite frameworks is compensated by ions trapped inside the pores of the structure. The most common are alkaline-earth metal cations, such as sodium, potassium or magnesium. The zeolite voids are also filled with water (or other) molecules. The trapped ions may be exchanged in a process known as cation exchange. Zeolites may also easily lose and gain water reversibly. Since their pores have a fixed size, only molecules that fit in are trapped, the bigger molecules are sieved out. Zeolites are, thus, also known as “molecular sieves”.

Since 1980 zeolites with new chemical makeup started to appear, the oldest being AIPOs built-up from alternating corner-sharing $[\text{AlO}_4]^{5-}$ and $[\text{PO}_4]^{3-}$ tetrahedral [8]. Also, based on those aluminophosphates, many novel microporous framework structures appeared, by doping with silicon or transitions metals, for example. While those aluminophosphates and zeolites are built of similar tetrahedral building blocks, many new structures also comprise new building units such as octahedra or pentahedra (OPT materials). For example, a lot of research has been carried out on the microporous titanosilicate ETS-10, composed of tetrahedral $[\text{SiO}_4]^{4-}$ and octahedral $[\text{TiO}_6]^{8-}$ units [8].

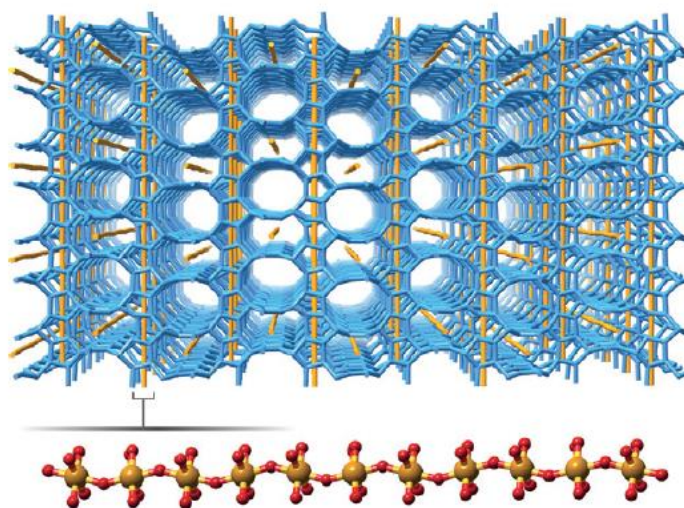


Figure 7: Crystal structure of ETS-10. Titanium oxide chains are represented by orange rods and siliceous matrix with corner-shared $[\text{SiO}_4]^{4-}$ units is depicted in blue (oxygen atoms have been omitted for clarity) [8].

The new structures and chemistry of microporous heteropolyhedra prompted research into their potential use in catalysis, separation and ion exchange.

1.2.2 Lanthanide silicates

Another interesting feature of such microporous structures is the possibility of introducing photoluminescent trivalent lanthanide centres into the framework. Those new structures combining silicates and lanthanides cannot be considered as conventional zeolites anymore but are referred to as microporous lanthanide silicates.

The beginning of the lanthanide silicate research started in 1997 by Rocha et al. For example, among the first of those new materials is AV-5, $(\text{Na}_4[\text{K}_2\text{Ce}_2\text{Si}_{16}\text{O}_{38}]\cdot 10\text{H}_2\text{O})$, a montregianite-related compound. This structure is made out of 2 different layers: a double silicate sheet and an open octahedral sheet composed of $[\text{YO}_6]$ and three distinct $[\text{NaO}_4(\text{H}_2\text{O})_2]$ octahedra. It exhibits a weak blue emission and a broad-band with two overlapping peaks at 377 nm and 410 nm, upon excitation at 325 nm [8].

Tuning the optical properties of lanthanide ions in a microporous structure is an important aspect. It can be done in many ways: further doping of the materials with heteroatoms, changing the structural dimensionality of the lanthanides, by introducing guest species that can act as antennae for the lanthanide ions and many other ways. This leads to many properties of lanthanide silicates and opened the possibility of creating photoluminescent thermometers.

The first example of microporous europium and terbium silicates has been reported by Ananias et al., the structure being $\text{Na}_4\text{K}_2\text{X}_2\text{Si}_{16}\text{O}_{38}\cdot 10\text{H}_2\text{O}$, $\text{X}=\text{Eu}, \text{Tb}$ and was called AV-9, it is also a montregianite-related compound. The structure is composed of 2 different types of layers alternating along the [100] direction. A double silicate sheet, where the single silicate sheet is of the apophyllite type with 4- and 8- membered rings and an open octahedral sheet, composed of two non-equivalent LnO_6 octahedra and two distinct $\text{NaO}_4(\text{H}_2\text{O})_2$ octahedra. The luminescence studies on this materials with europium, Eu-AV-9, shows the presence of two distinct Eu(III) local environment, while the studies on Tb-AV-9 do not allow the identification of more than one local Tb(III) local environment. However, the corresponding decay $^5\text{D}_4$ curves of Tb(III) were fitted by biexponential functions, confirming the presence of two distinct metal site environment [12], [13].

Ananias et al., reported the layered lanthanide silicates, $\text{K}_3[\text{M}_{1-a}\text{Ln}_a\text{Si}_3\text{O}_8(\text{OH})_2]$ with $\text{M}=\text{Y}^{3+}, \text{Tb}^{3+}$ and $\text{Ln}=\text{Eu}^{3+}, \text{Er}^{3+}, \text{Tb}^{3+}, \text{Gd}^{3+}$ named AV-22. The structure contains a single crystallographic Ln^{3+} centre coordinated to six SiO_4 tetrahedra, two distinct silicon tetrahedral, and two crystallographic sites for the potassium cations. The structure of these material permits the inclusion of different Ln^{3+} cations in one solid, allowing the fine-tuning of their photoluminescent properties [13]. The Er-AV-22 material is a room-temperature infrared emitter, while Tb- and Eu-AV-22 are visible emitters with output efficiencies comparable to standards used in commercial lamps [14]. The mixed $\text{Tb}^{3+}/\text{Eu}^{3+}$ materials shows evidence of the inclusion of Eu^{3+} ions in the interlayer space by replacing K^+ ions, allowing the activation of Tb^{3+} -to- Eu^{3+} energy transfer mechanism [14].

Kostova et al., reported the AV-23 materials, $K_3[MSi_3O_9]$ ($M=Y^{3+}, Tb^{3+}$), from calcination of AV-22 at 650 °C. Similar to AV-22, the structure of AV-23 contains a single crystallographically independent Ln^{3+} metal centre coordinated to six SiO_4 tetrahedra in a distorted octahedral geometry. Individual LnO_6 octahedra are isolated from each other by wollastonite-type siliceous chains $[Si_6O_{17}]_n^{10n-}$, running parallel to the a axis. A main difference between the two structures is the type of channels. The 7-membered pores in the layer of AV-22 align upon condensation along the a axis of AV-23. The condensation also generates more regular channels with 8-membered elliptical rings. Although the crystal structure reveals the presence of a single independent Ln^{3+} environment, the photoluminescent studies exhibits the presence of two or three Ln^{3+} local environment. Investigations by recording their decay curves on the ${}^7F_{0-2}$ confirm the existence of two or three Ln^{3+} sites [13].

More recently, in 2016, studies on the microporous silicate Eu-AV-20 showed promising ion exchange capabilities of these solids for cesium removal from aqueous solutions. The structure of Eu-AV-20 resembles the tobermorite structure; where two Ca^{2+} are substituted by one Eu^{3+} and one Na^+ , both with seven coordination. Some europium cations are disordered over the sodium sites, and thus columns of Eu/Na polyhedral running along [110] direction and neighbouring in each layer exist in the AV-20 form. The Eu/Na polyhedral layers are connected through the double silicate chains building a frameworks with channels running along the [110] direction [13]. The uptake of Cs^+ modifies the local environment of the Eu^{3+} emitter resulting in changes in the two ${}^5D_0 \rightarrow {}^7F_0$ transition intensities and line positions, indicating the potential of Eu-AV-20 for sensing purposes [15].

1.2.3 Zeolite synthesis

The synthesis of zeolites started around 1940, firstly developed by Barrer and Milton, who have tried to reproduce the natural conditions in which the zeolites are created, i.e., high pressure and temperature [16]. Therefore, they used hydrothermal treatment, which became the standard method employed to synthesised such materials.

Hydrothermal treatment involves a synthesis gel, with a basic character, pH 10-13, heated in an autoclave, generally Teflon-lined, at temperatures between 130 and 240 °C, under autogenous pressure. The reaction times vary between a few hours and one month. Sometimes, microwave irradiation is used allowing shortening the reaction time. To prepare the desired gel, a silicon source is used, like a sodium silicate solution, a base like sodium hydroxide to adjust the pH and to work as a mineralizing agent, water and the desired metals. Structure directing agents (organic molecules or cations that act as a template for the formation of the pores in the framework structure) may be added.

1.2.4 Lanthanide silicates synthesis

The synthesis of lanthanide silicate is similar to zeolite synthesis. They are synthesized in Teflon lined autoclaves under static hydrothermal conditions. A first solution made out of sodium silicate with

sodium hydroxide and water is prepared, then under strong stirring, the lanthanide ions solutions are added. Generally, nitrates or chlorides lanthanide solutions are used. Once in the autoclaves, the samples are put in an oven at the desired temperature (below 240 °C).

1.3 THERMOMETRY AND LANTHANIDE SILICATES

1.3.1 Luminescent thermometry

Thermometry measurements can be classified into three different categories, depending on the nature of the contact between the sensor and the object to probe:

- Invasive: the thermometer is in direct contact with the medium of interest, e.g. thermocouple-based technology.
- Semi-invasive: The medium of interest is treated in some manner to enable remote observation, e.g. imaging of thermally sensitive paints.
- Non-invasive: The medium of interest is observed remotely, e.g. infrared and luminescence thermography [17].

Traditional contact thermometry is not suitable for temperature measurements under 10 μm and since it generally requires conductive heat transfer, it disturbs the actual temperature of the sample during the measurement. This is especially true for objects small compared to the sensor head [18]. Today, the need for non-invasive thermometers is great.

As explained earlier, the emission of lanthanide ions is temperature dependent, and the increase of temperature may lead to a decrease in emission intensity. This phenomenon is being studied by many groups interested in temperature sensing.

In luminescence thermometry, there are three main techniques to measure temperature: spectral shift of a certain transition; variation of the integrated emission intensity of a single transition or a pair of transitions; and lifetime measurements by observing the decay profiles of the emitting excited states of the luminescent centre [19].

Different matrices may be used to observe the lanthanide luminescence, for example, silicates or metal organic frameworks (MOFs). The latter are used because they offer an excellent platform to engineer and adjust the luminescent properties due to their numerous potential sources of light emissions, like metals ions, ligands, guest ions or molecules. Also leading to different luminescence features like metal sensitization by ligands (*antenna effect*) and host-guest interactions. Silicates also show great potential as lanthanide luminescence matrices and are the focus of this study.

Optical thermometers based on the intensity ratio of two separate electronic transitions are called dual-centre thermometers. This is the most common way of creating ratiometric thermometers. They may comprise a ligand and a lanthanide ion or two lanthanide ions.

1.3.2 Parameters of a ratiometric luminescent thermometer

To determine the temperature experimentally, the thermometric parameter $\Delta(T)$ is used and is equal to the ratio between the integrated intensities of two emitting transitions (I_1 and I_2) from the same or from two distinct emitting entities:

$$\Delta(T) = \frac{I_1}{I_2} \quad (5)$$

The performance of a luminescence thermometer is determined by 4 parameters [19]:

- The relative thermal sensitivity S_r that indicates the relative change of the thermometric parameter per degree of temperature change:

$$S_r = \frac{1}{\Delta} \left| \frac{\partial \Delta}{\partial T} \right| \quad (6)$$

S_r allows the direct comparison of thermometer systems since it is independent of the nature of the thermometer, be it mechanical, electrical or luminescent.

- The temperature uncertainty δT gives the smallest temperature change that can be ascertained during a measurement:

$$\delta T = \frac{1}{S_r} \frac{\delta \Delta}{\Delta} \quad (7)$$

Experimentally δT is determined by the distribution of temperature readouts when the thermometer is at a certain reference temperature T .

- The spatial resolution, δX , is defined as the minimum distance between points showing a difference in temperature larger than the temperature uncertainty δT :

$$\delta X = \frac{\delta T}{|\vec{\nabla} T|_{max}} \quad (8)$$

Where $|\vec{\nabla} T|_{max}$ is the maximum temperature gradient of the mapping.

$$\delta t = \frac{\delta T}{|\partial T / \partial t|_{max}} \quad (9)$$

The temporal resolution is the minimum time interval between measurements with a temperature higher than δT :

Where $|\partial T / \partial t|_{max}$ is the maximum temperature change per unit of time.

- Repeatability and reproducibility indicate the variation in repeat measurements realised under identical measurements.:

$$R = 1 - \frac{\max(|\Delta_c - \Delta_i|)}{\Delta} \quad (10)$$

Where Δ_c is the mean thermometric parameter and Δ_i the value of each measurement of the thermometric parameter. Generally, 10 measurements are carried out to obtained a significant value of R.

1.4 STATE-OF-THE-ART OF LANTHANIDE LUMINESCENT THERMOMETRY

Lanthanide silicates are emerging materials that still need to be explored. Recently they showed potential in the field of wastewater remediation by removing unwanted cations through ion exchange [15], [20].

Many different microporous silicates containing lanthanides have already been studied by different research groups. Rocha et al., reported structural analogs of mineral montregianite, AV-5 (Ln = Ce³⁺) [21] and AV-9 (Ln=Eu³⁺, Tb³⁺), a microporous Eu(III) and Tb(III) silicates, which explore the possibility of combining microporosity and optical properties [12]. These materials showed potential in photonic applications, as light sources, detector systems and light-emitting diode [13]. Ferreira et al., reported materials related to tobermorites, hydrated calcium silicate minerals, AV-20 (Ln= Eu, Tb, Sm and Ce) [22]. Tsapatsis et al., reported Na_{4.8}Ce₂Si₁₂O₃₀·4H₂O made out of [Si₂O₅²⁻] silicate layers with 5-, 8-rings connected by CeO₆ octahedra [23]. Wang et al., reported the microporous lanthanide silicate LnSiO-CJn (n = 1-6, Ln = Ce, Tb, or Eu) built up from SiO₄ tetrahedra and Ln-centered polyhedra (LnO₆, LnO₇ or LnO₈) to form three-dimensional open frameworks [24].

Regarding the use of lanthanide silicates to act as a non-invasive thermometers one study has already been made. It explored the compound Na[(Gd_{1-a}Eu_a)SiO₄], a lanthanide silicate orthorhombic system showing great potential for ratiometric thermometry [25]. This compound shows structural disorder and a temperature phase transition. The distinct thermal behaviour of both rare-earth ions, europium and terbium, was detected as well as a temperature dependence of an emission ratio between the

two following transitions Tb^{3+} ($^5\text{D}_4 \rightarrow ^7\text{F}_{5-0}$) and Eu^{3+} ($^5\text{D}_0 \rightarrow ^7\text{F}_{0-4}$) of those lanthanides. This emission ratio gives to $\text{Na}[(\text{Gd}_{1-a}\text{Eu}_a)\text{SiO}_4]$ the potential to be used as ratiometric thermometer.

This compound was made under hydrothermal conditions and its crystalline structure was analysed at 100 K and 30 K.

The single-crystal studies showed that at 100 K the lanthanide silicate adopts a centrosymmetric orthorhombic space group $Pnma$, with some structural disorder. The analysis of the structure at 30 K shows a reduction of the structural disorder, and unit cell change to body-centred and space group to $Imma$. The disorder around the lanthanide ions is greatly reduced at low temperature. Therefore, a phase transition happens between 30 K and 100 K, reducing but not eliminating the structural disorder.

The structural modification observed is confirmed by Eu^{3+} photoluminescence studies in the range 12 K to 296 K. The typical $^5\text{D}_0 \rightarrow ^7\text{F}_1$ transition of Eu^{3+} shows proof of the structural modification from $Pnma$ to $Imma$ space groups with decreasing temperature (Fig 8).

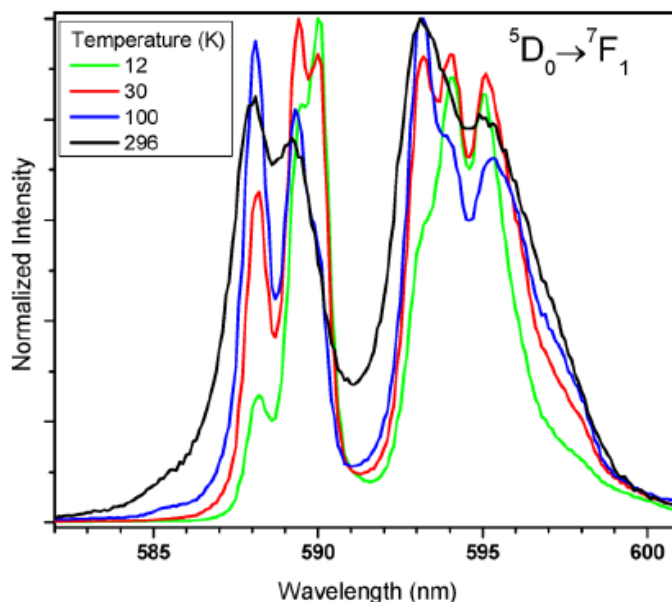


Figure 8: Temperature dependence of $\text{Na}[(\text{Gd}_{0.99}\text{Eu}_{0.01})\text{SiO}_4]$ emission spectra in the $^5\text{D}_0 \rightarrow ^7\text{F}_1$ transition region [25].

Indeed, the emission lines can be gathered in two groups, the first one for the temperatures of 12 K and 30 K and the second for 100 K and 296 K. Also, at 296 K the structure is assumed to be $Pnma$, because the experimental powder XRD diffractogram obtained at room temperature is in accordance

with the simulated one obtained at 100 K from the single-crystal data. Therefore, the first group corresponds to the *Imma* space group while the second to the *Pnma*.

This compound shows energy transfer from Gd^{3+} to Eu^{3+} and to Tb^{3+} and from Tb^{3+} to Eu^{3+} , with the last one very dependent on the temperature. For the compound $\text{Na}[(\text{Gd}_{0.8}\text{Eu}_{0.1}\text{Tb}_{0.1})\text{SiO}_4]$, the emission spectra have been recorded from 12 to 300 K under the Tb^{3+} excitation at 483 nm, corresponding to the $^7\text{F}_6 \rightarrow ^5\text{D}_4$ transition, to observe the effect of the temperature on the intensity of the Eu^{3+} and Tb^{3+} emissions (Fig 9).

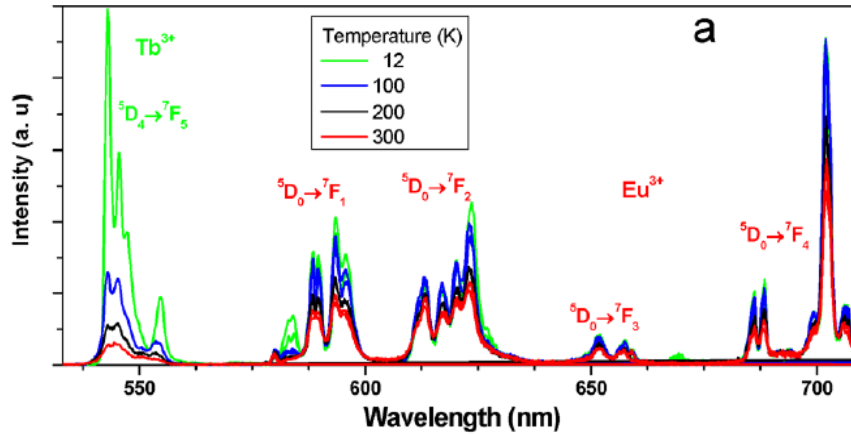


Figure 9: Emission spectra of $\text{Na}[(\text{Gd}_{0.8}\text{Eu}_{0.1}\text{Tb}_{0.1})\text{SiO}_4]$ under 483.5 Tb^{3+} excitation [25].

The emission spectrum presents both the Tb^{3+} ($^5\text{D}_4 \rightarrow ^7\text{F}_{5-0}$) and Eu^{3+} ($^5\text{D}_0 \rightarrow ^7\text{F}_{0-4}$) transitions whose intensities depend on the temperature. With increasing temperature, the Tb^{3+} -to- Eu^{3+} energy transfer is promoted, leading to a change of colour from yellow at 12 K to red at 300 K where the emission is essentially due to the Eu^{3+} transitions. To determine the absolute temperature, the measurement is made through the experimental parameter Δ defined as the integrated intensity ratio of the Tb^{3+} ($^5\text{D}_4 \rightarrow ^7\text{F}_5$) and Eu^{3+} ($^5\text{D}_0 \rightarrow ^7\text{F}_4$) transitions. Therefore, the thermometric capacity of this compound would rely on the temperature dependence of the energy transfer between the Tb^{3+} and Eu^{3+} ion.

This lanthanide silicate was one of the first examples of a ratiometric thermometer for cryogenic temperature under 100 K whose performance is determined by a structural transition, with a robust and very stable silicate.

II EXPERIMENTAL PART

2.1 AIM OF STUDY

The aim of this study is to evaluate the potential of tetragonal NaLnSiO_4 with $\text{Ln} = \text{Gd}, \text{Eu}, \text{Tb}$ to be used as a ratiometric thermometer. The single-crystal structure of NaGdSiO_4 has been investigated (Fig 10). It crystallizes in the space group $I4/m$ (n 87) with the following unit cell dimensions: $a=b=11.63 \text{ \AA}$ and $c=5.41 \text{ \AA}$; $\alpha=\beta=\gamma=90^\circ$; $Z=8$.

The structure is built up from SiO_4 tetrahedra units and GdO_6 polyhedra with square bipyramidal geometry. The Hexacoordinated Gd^{3+} forms tetrameric unities (Fig 10, right) connected by the isolated silicon units. The Na^+ are the charge balancing cations.

Related, but distinct compounds, with our material, such as $\text{NaSmSiO}_4 \cdot 0.25\text{NaF}$ [26] and $\text{NaGdSiO}_4 \cdot x\text{NaOH}$ ($x \approx 0.2$) [27] have been reported.

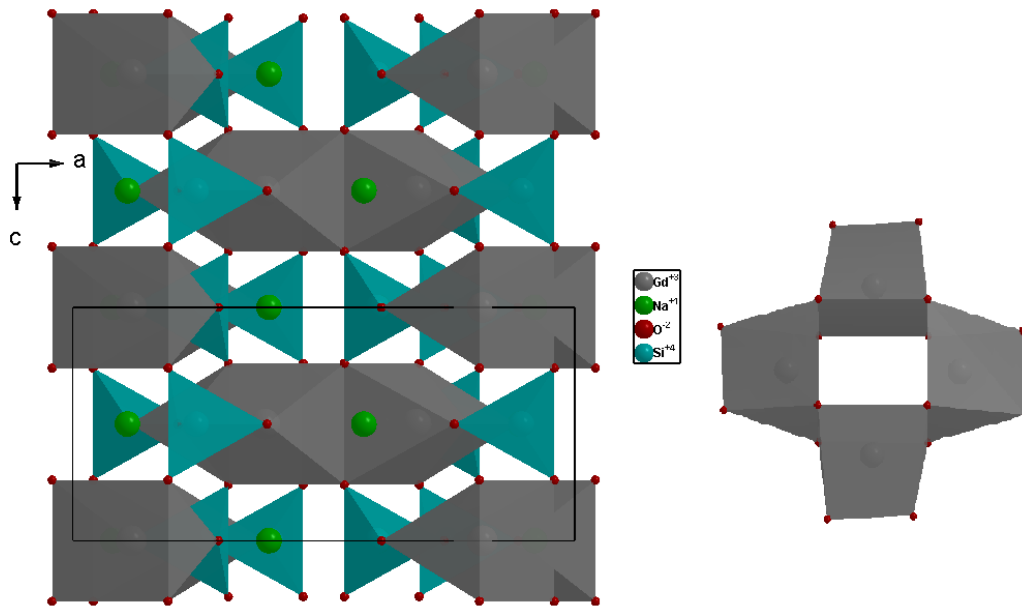


Figure 10: Crystalline structure of NaGdSiO_4 showing the tetrameric units of hexacoordinated Gd^{3+} [28].

The first example of a luminescent ratiometric thermometer based on Ln silicates compound was reported in 2015 by Ananias et al. [25]; $\text{Na}[\text{LnSiO}_4]$ with $\text{Ln} = \text{Gd}, \text{Eu}, \text{Tb}$ in an orthorhombic structure and proved its potential as a photoluminescent. The composition is identical to our material.

2.2 SYNTHESIS

Syntheses were realised in hydrothermal conditions. They were carried out in Teflon lined autoclaves of either 21 or 12 mL. To obtain the starting gel an alkaline solution was made by mixing sodium silicate solution (SSS) (27% m/m SiO₂, 8% m/m Na₂O Merck) with water and sodium hydroxide (99%, AnalaR Normapur). Then the lanthanide nitrate solutions were added slowly under stirring. The lanthanide nitrates were prepared by dissolving the corresponding lanthanide oxides (99.99% purity) with stoichiometric amounts of diluted nitric acid under heating to obtain the following solutions: Tb(NO₃)₃ 0.5 M, Eu(NO₃)₃ 0.5 M, Gd(NO₃)₃ 0.4 M, Yb(NO₃)₃ 0.4 M and Er(NO₃)₃ 0.4 M. After two hours of stirring, the solutions in the autoclaves were transferred to the oven from 1 hour to 7 days at 150-245 °C, next the autoclaves were cool down with cold water. The samples, collected by precipitation, were washed at least 4 times with distilled water. Details for each synthesis are given in the annex 1.2.

2.3 INSTRUMENTATION

2.3.1 Powder X-Ray diffraction

Powder X-Ray Diffraction data were collected at room temperature on a Philips Analytical Empyrean (Cu K α _{1,2} X-radiation, $\lambda_1=1.540598$ Å; $\lambda_2=1.544426$ Å), equipped with an PIXcel 1D detector and a flat-plate sample holder in a Bragg-Brentano para-focusing optics configuration (45 kV, 40 mA). Intensity data were collected by the step-counting method (step 0.04°), in continuous mode, in the ca. $5 \leq 2\theta \leq 50^\circ$ range.

2.3.2 Scanning Electron Microscopy

Scanning electron microscopy (SEM) images were obtained in a Hitachi SU-70 microscope to assess crystal dimensions (equivalent particle diameter) and morphology.

2.3.3 Raman spectroscopy

The FT Raman spectra were recorded on a RFS-100 Bruker FT- spectrometer, equipped with a Nd:YAG laser with an excitation wavelength of 1064 nm. 200 scans were taken from 4000 to -2000 cm⁻¹ with a resolution of 4 cm⁻¹ and laser power set at 300 mW.

2.3.4 Infra-red spectroscopy

Infrared spectra were recorded on a Mattson 7000 FTIR spectrometer in the transmission mode. Semi-transparent pellets were made out of 1.2 mg of each sample mixed with approximately 200 mg of KBr and pressed with 9 tones for 2 minutes and semi-transparent pallets were obtained. 256 scans were taken for wavenumbers between 300 and 4000 cm^{-1} with a resolution 7 cm^{-1} and 4 cm^{-1} .

2.3.5 Photoluminescence spectroscopy

The emission and excitation spectra were recorded on a modular double grating excitation spectrofluorimeter with a TRIAX 320 emission monochromator (Fluorolog-3, Horiba Scientific) coupled to a R928 or a H9170 Hamamatsu photomultipliers, for the detection on the visible and near infrared spectral ranges, respectively, using the front face acquisition mode. The excitation source was a 450 W Xe arc lamp. The emission spectra were corrected for detection and optical spectral response of the spectrofluorimeter and the excitation spectra were corrected for the spectral distribution of the lamp intensity using a photodiode reference detector. Time-resolved measurements were carried out with the pulsed Xe-Hg lamp excitation, in front face acquisition mode. The temperature was controlled by a helium-closed cycle cryostat with vacuum system measuring *ca.* 5×10^{-6} mbar and a Lakeshore 330 auto-tuning temperature controller with a resistance heater. The temperature can be adjusted from *ca.* 12 to 450 K with a maximum accuracy of 0.1 K. The sample temperature was fixed at a given value using the auto-tuning temperature controller; after waiting a minimum of 5 minutes to thermalize the sample, four consecutive steady-state emission spectra were measured for each temperature; the maximum temperature difference detected during the acquisitions was 0.1 K, the temperature accuracy of the controller.

2.3.6 NMR spectroscopy

NMR spectra were recorded on a Bruker Avance III 400 wide bore (400 MHz, ^1H Larmor frequency). A double-resonance MAS probe was employed to record the ^{29}Si spectra at 79.5 MHz Larmor frequency. The sample was spun in ZrO_2 rotors of 7 mm diameter at a spinning rate of 5 kHz. The ^{29}Si /MAS NMR spectrum was recorded with a recycle delay of 60 s and a pulse of 2.7 μs .

III RESULTS AND DISCUSSION

3.1 SYNTHESIS PARAMETERS VARIATION

From previous experiments [25], it was determined that the material composition requires a higher amount of Tb^{3+} than Eu^{3+} due to the energy transfer, and a minimum of 80% of Gd^{3+} obtain the best photoluminescence. Therefore, to determine the best protocol to obtain the compound $\text{Na}[\text{LnSiO}_4]$ with $\text{Ln}=\text{Gd}, \text{Eu}, \text{Tb}$, with tetragonal crystal structure, the sample $\text{Na}[(\text{Gd}_{0.8}\text{Eu}_{0.05}\text{Tb}_{0.15})\text{SiO}_4]$ was studied by changing the different synthesis parameters : temperature, time, ratio silicate (Si):lanthanide (Ln) and silicate (Si): sodium (Na). Syntheses were carried out in autoclaves of 12 mL and 21 mL, adding a variation of another parameter.

3.1.1- Temperature variation

To determine the best synthesis temperature, compounds were prepared in the condition 'Synthesis A' (annexe 1.2) at 4 different temperatures. Samples were studied by powder XRD and SEM.

Powder XRD

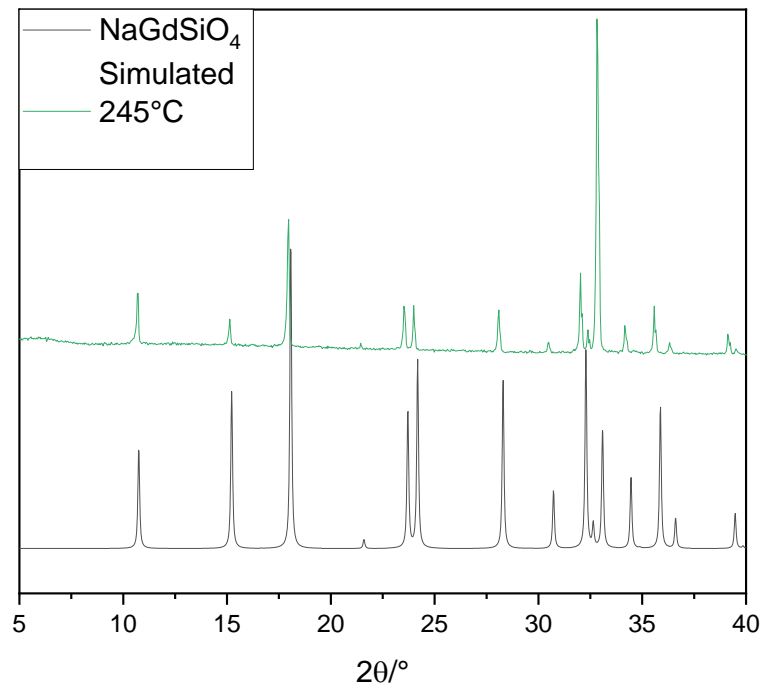


Figure 11 : Experimental and simulated powder XRD patterns of the sample synthesized at 245 °C and of tetragonal NaGdSiO_4 (ICSD 16188) [29].

The target phase is obtained for the sample synthesized at 245 °C.

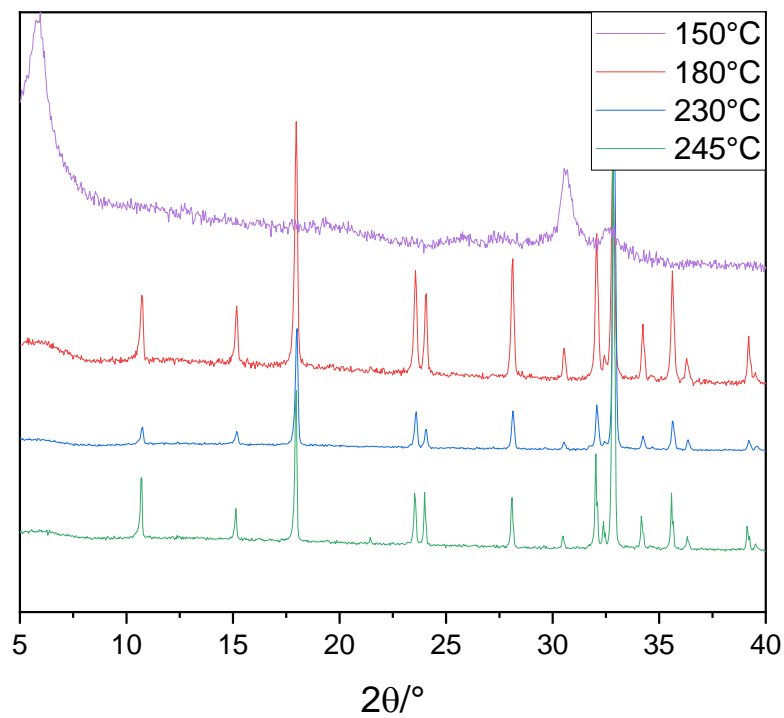


Figure 12: Powder XRD patterns of samples prepared at the oven temperatures depicted.

The right phase was obtained at 180 °C, 230 °C and 245 °C, but a different phase was obtained at 150 °C. Furthermore, the particles size decreases by decreasing the temperature (e.g., 180°C) leading to a broadening of the XRD peaks. The signal-to-noise ratio indicates an increase of crystallinity with increasing temperature. Therefore, by varying the synthesis temperature, we can obtain different size of particles.

SEM

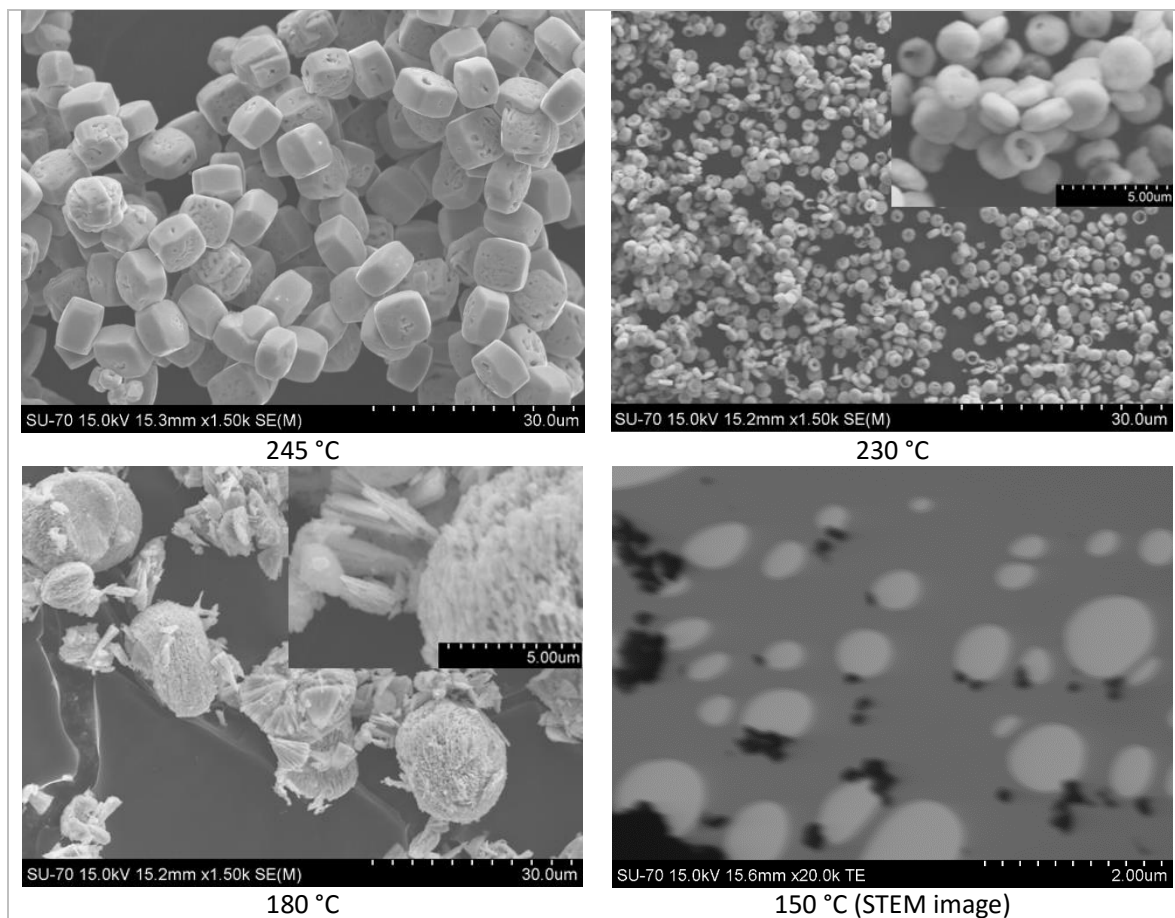


Figure 13: SEM and STEM images of the compounds synthesized at different temperatures.

At 245 °C the crystals are cuboid-shaped particles of homogenous size around 6-9 μm . When the temperature is decreased to 230 °C the particles are about three times smaller, 2-3 μm , and disk (or ring)-shaped. At lower synthesis temperature, the particles become smaller forming aggregates and thus the crystal morphology is not clear. To get better images of the particles, we performed STEM for the sample synthesized at 150 °C, however the image is not clear and doesn't allow us to distinguish the form but the particles reach the size of 0.2 μm . The higher the temperature, the larger the particles. At 180 °C the particles reach nanometre size.

To obtain particles in the micrometres range, the best oven time is 230 – 245 °C.

3.1.2- Time variation

To determine the best synthesis time, compounds were prepared in the condition 'Synthesis B' (annexe 1.2) at 7 different times, and characterized by powder XRD and SEM.

Powder XRD

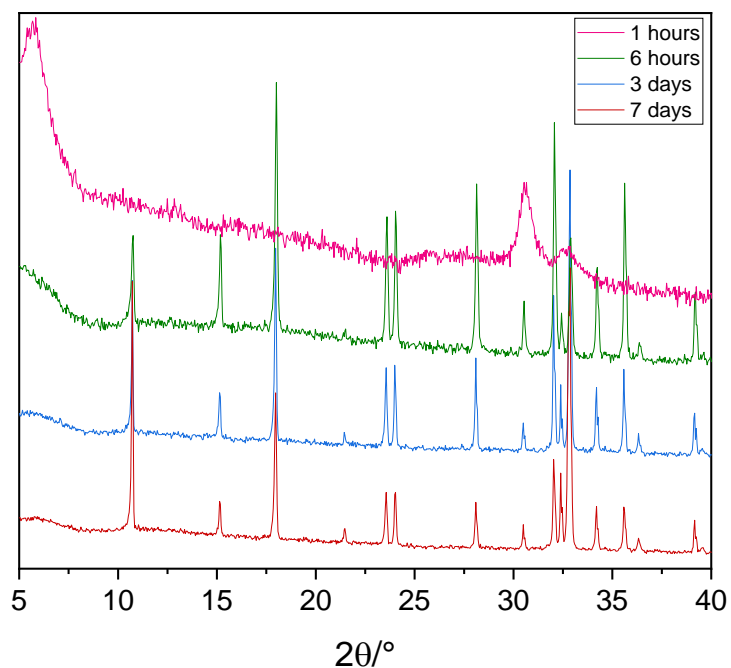
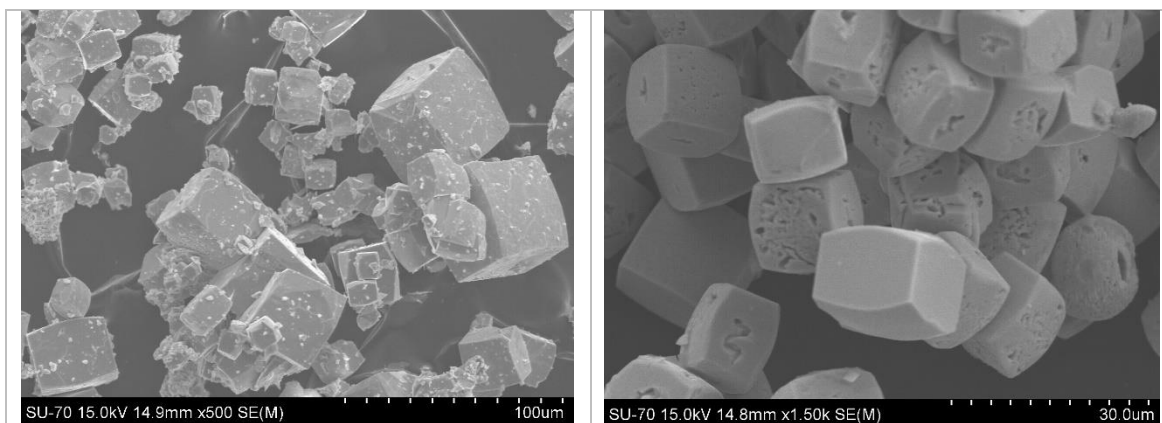


Figure 14: Powder XRD patterns of samples at different synthesis time.

The target phase is obtained from 7 days to 6 hours of synthesis time. After 1 hour, the phase obtained is similar to the one for a synthesis temperature of 150 °C.

SEM



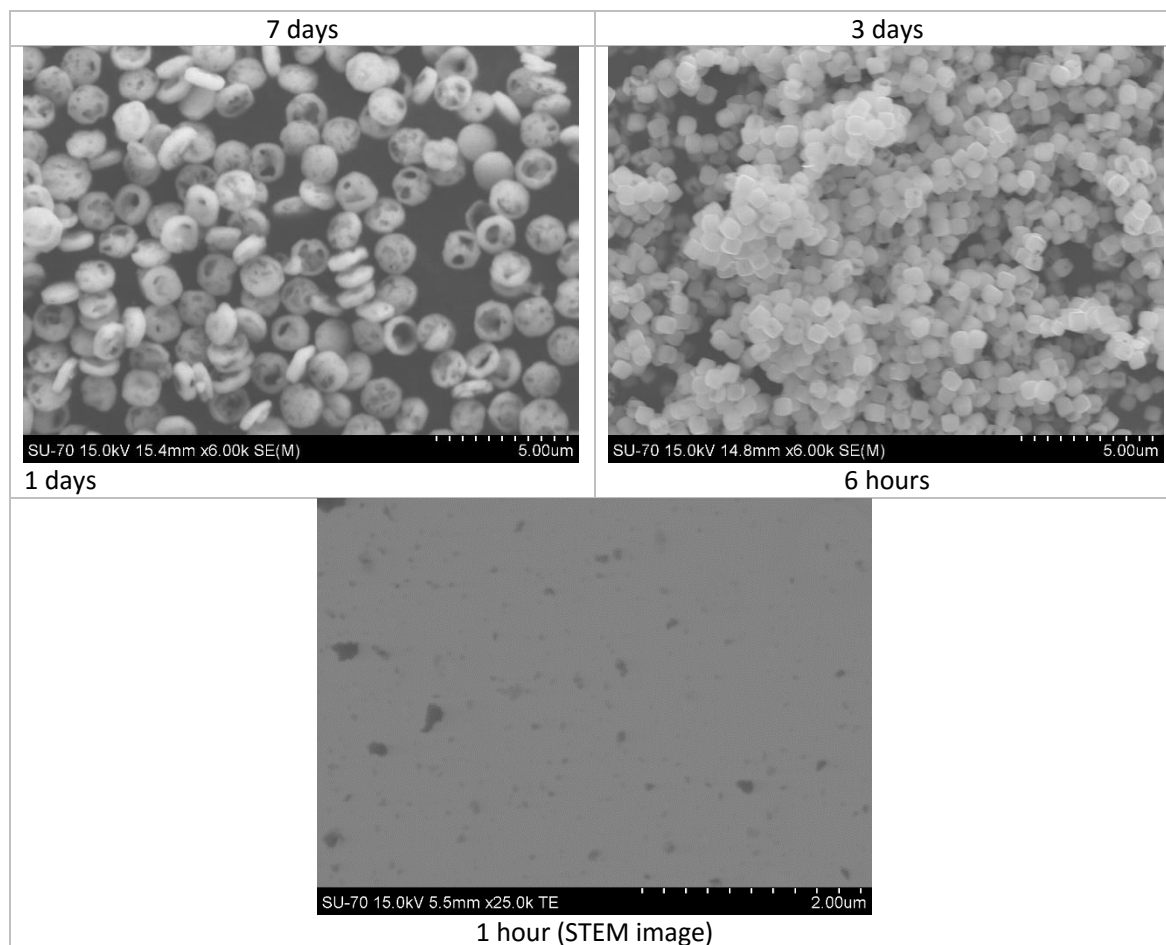


Figure 15: SEM and STEM images of the compounds synthesized a different times.

For each synthesis time the samples show a small narrow distribution of particles size, and no impurity, except for 7 days when the particle size shows a wide distribution, including the biggest particles reaching 50 μm . After 3 days, the particle size is 9-12 μm , whereas for 1 day synthesis time, the particle size is 1 – 1,5 μm , and for 6 hours 0.5–1 μm . The shape is also affected by the synthesis time: after 7 and 4 days the particles are cuboids-shaped, the latter presenting more defects. After 1 day, the particles are disk-shaped, some even ring-shaped, while some spheroid crystals are also present. Surprisingly, after 6 hours the particles are cuboid-shaped with almost no defects. After only 1 hour, the particles are very small and form aggregates, therefore we have also imaged them with STEM. Again, the image is not clear and doesn't allow ascertaining the shape, but the size is in the nanometric range.

The best synthesis time to obtain a small distribution of particle sizes is in the range 6 hours to 4 days.

3.1.3- Lanthanide: Silicon ratio

To determine the best Si:Ln ratio for the synthesis, 'Synthesis C' (annex 1.2) was used to prepare samples with 7 different ratios, which were characterised by XRD and SEM.

Powder XRD

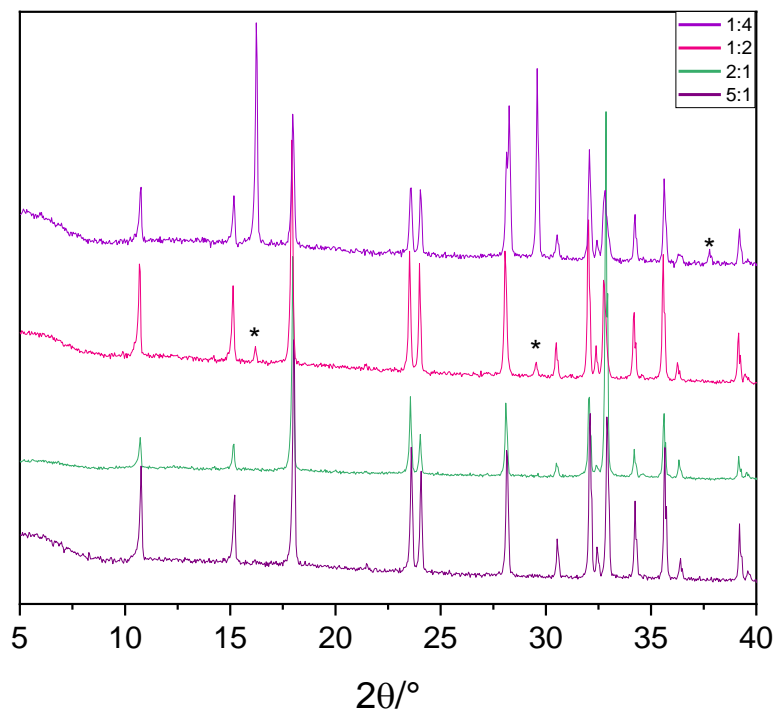


Figure 16 : Powder XRD patterns of samples with different Ln:Si ratios. (*) depict impurities.

The pure target phase is obtained for the ratios 5:1 and 1:1.

SEM

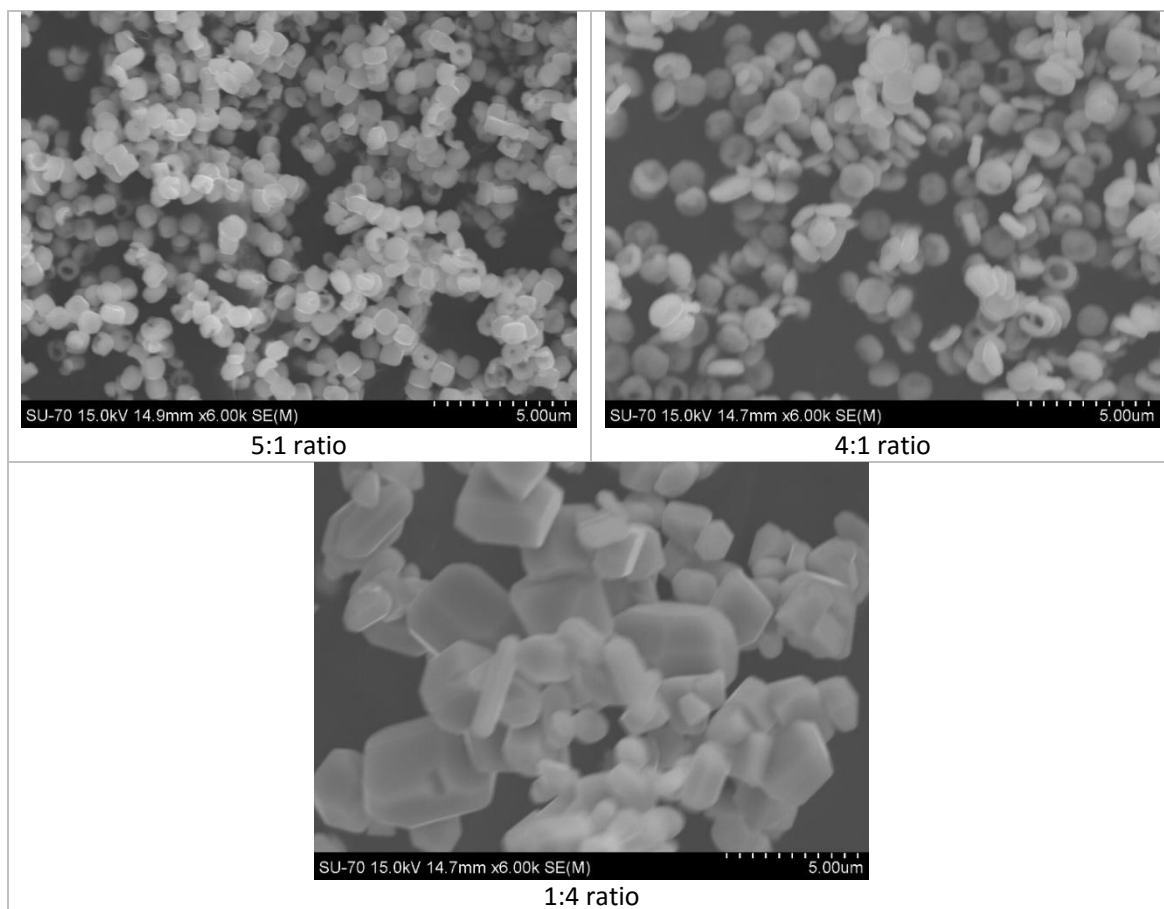


Figure 17: SEM images of the compounds with a Si:Ln ratio of 5:1, 4:1 and 1:4.

The compound with a ratio of 1:4 shows crystals with, at least, two different habits, confirming the impurities seen by XRD. The samples with a ratio of 5:1 and 4:1 show narrow size distributions, with average value 1 μm . The former exhibits cuboid crystals, the latter discs and some rings.

Considering those results, the target phase is obtained with a ratio from 5:1 to 1:1, with a change of shape depending on the ratio.

3.1.4- Silicate:sodium ratio

To determine the best Si:Na ratio, 'Synthesis D' (annex 1.2) was used to prepare samples with 5 different ratios, which were characterised by XRD and SEM.

Powder XRD

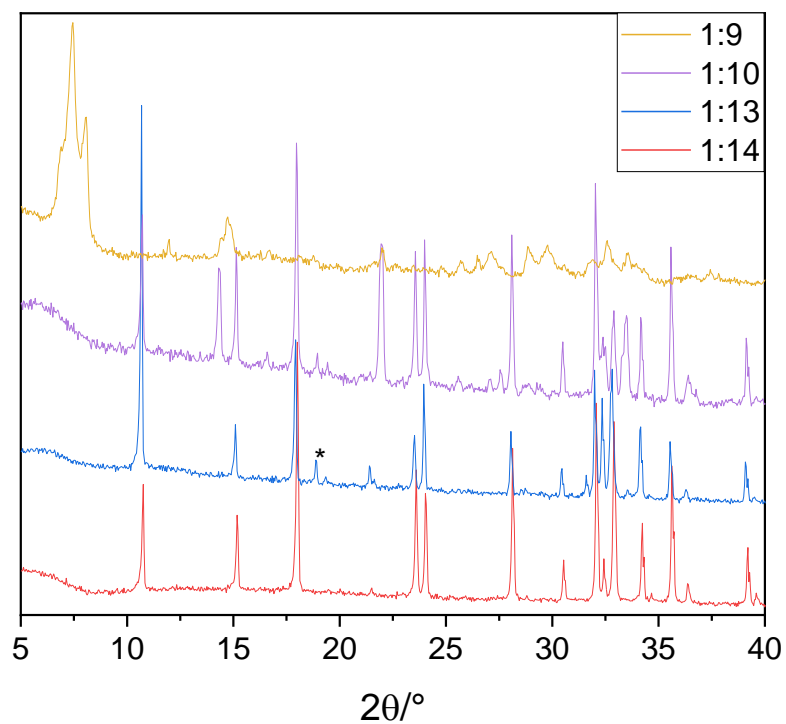
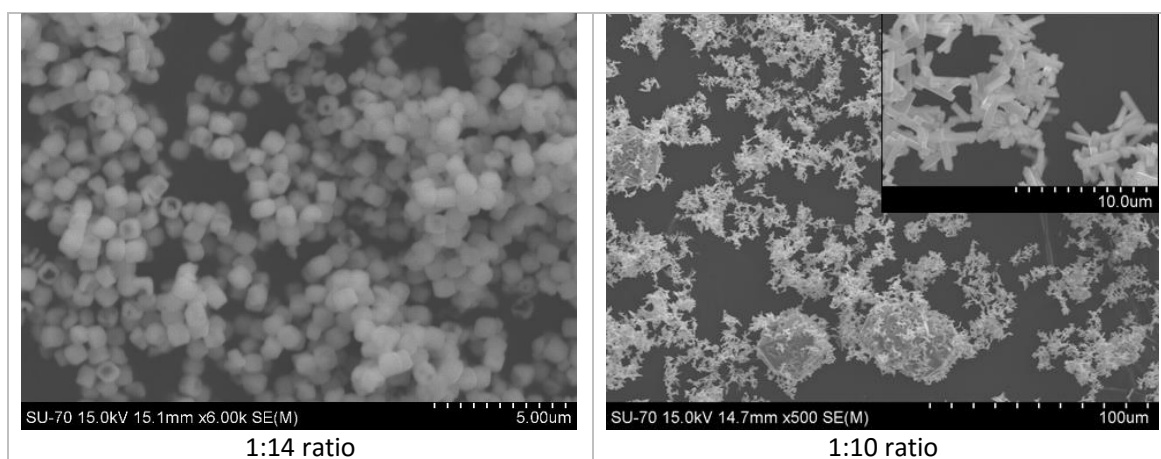


Figure 18 : Powder XRD patterns of samples prepared with different Si:Na ratios. (*) depicts impurities.

For ratio larger than 1:13, impurities appear and, eventually, a different phase is obtained at 1:10 and 1:9. Therefore, 1:14 is the best ratio.

SEM



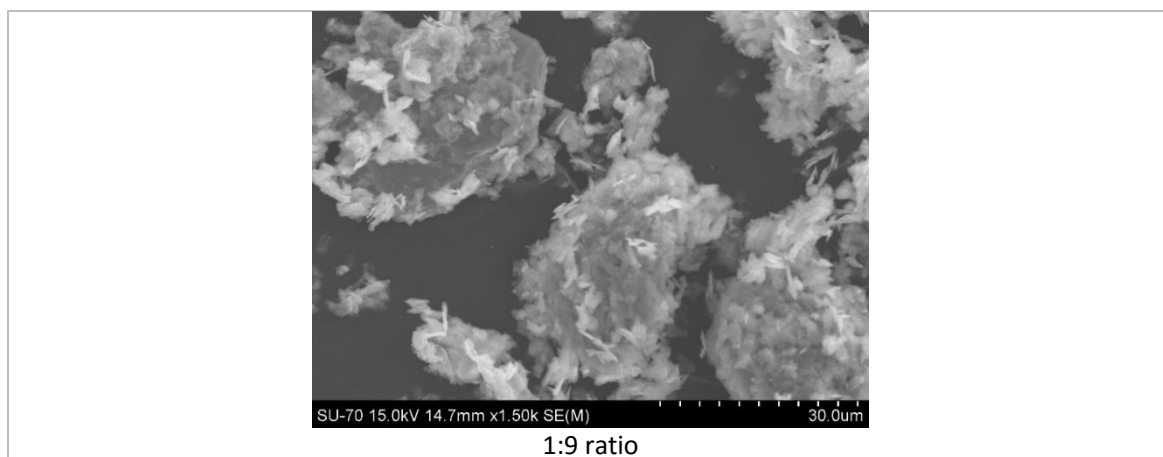


Figure 19: SEM images of the compounds with a Si:Na ratio of 1:14, 1:10, 1:9.

SEM images show that for the ratio 1:14, cuboid crystals are obtained with a narrow size distribution of 0.5-1 μm and no impurities are present. For 1:10, two different crystal types are present, spherical crystals around 30-40 μm and rods with a length of 3-4 μm . For 1:9 the particles aggregate, and are too small to ascertain size or shape. These results confirm XRD. A ratio of 1:14 is needed to obtain the target phase.

In conclusion, the best conditions to prepare the compound $\text{Na}[\text{LnSiO}_4]$ comprise a ratio from 1:1 to 5:1 for Si:Ln, 1:14 for Si:Na, and synthesis temperature and time 245-230 $^{\circ}\text{C}$, 6 hours-4 days.

3.1.5- $\text{Na}[\text{LnSiO}_4]$ with Ln = Gd, Eu, Tb

To obtain the best photoluminescent thermometer, samples with the following Gd:Eu:Tb compositions were prepared: 66.6/16.7/16.7; 82/9.0/9.0; 82/4.5/13.5; 66.6/4.2/29.2; 84/4/12; 80/5/15; 80/3.3/16.7; 85/5/10 (see 'synthesis E' in annex 1.2). The synthesis conditions are the following: 5:1 Si:Ln ratio, 1:14 Si:Na ratio, 245 $^{\circ}\text{C}$, 4 days. Samples were characterized by XRD and SEM.

Powder XRD

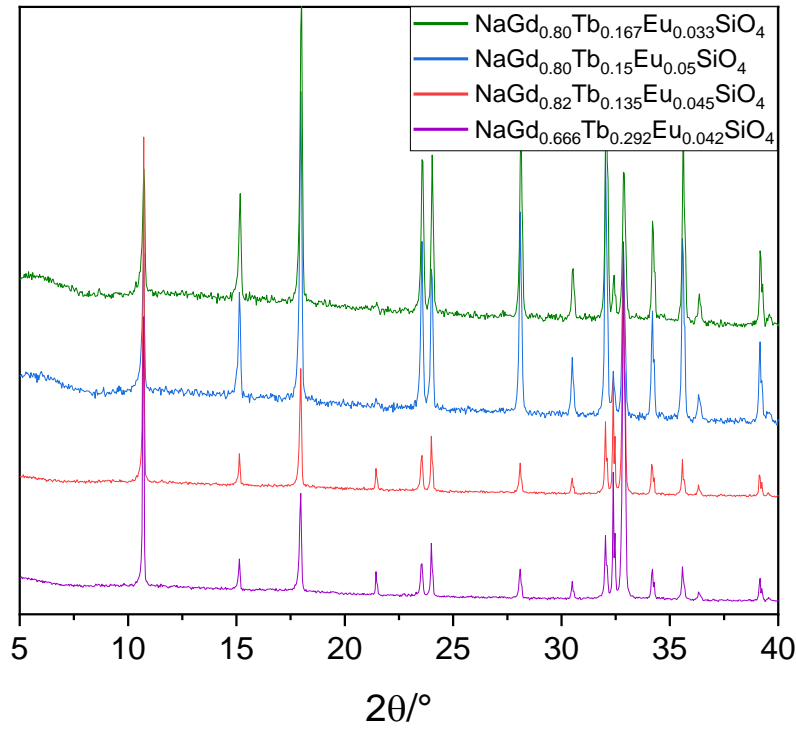


Figure 20: Powder XRD patterns of samples prepared with the indicated Gd:Eu:Tb ratios.

The powder XRD patterns of the obtained samples are identical to the pattern simulated for the tetragonal NaGdSiO₄ compound (ICSD 16188).

SEM

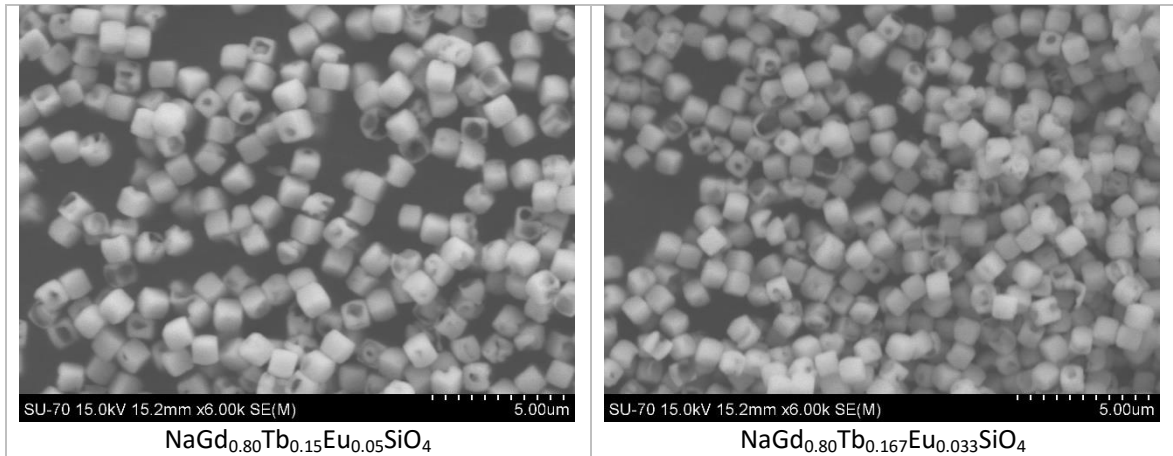


Figure 21: SEM images of NaGd_{0.80}Tb_{0.15}Eu_{0.05}SiO₄ and NaGd_{0.80}Tb_{0.167}Eu_{0.033}SiO₄.

SEM images show the obtained samples consist of cuboid crystals with a narrow size distribution. There is no evidence for the presence of any impurity phases. The average particle size of NaGd_{0.80}Tb_{0.15}Eu_{0.05}SiO₄ is around 1 μm, and 0,5-1 μm for NaGd_{0.80}Tb_{0.167}Eu_{0.033}SiO₄.

3.1.6- Na[LnSiO₄] with Ln = Gd, Er, Yb

To explore the possibility of photoluminescence in the infrared, Na[LnSiO₄] with Ln = Gd, Er, Yb were also studied. The same synthesis conditions (see 'Synthesis F' in annex 1.2) were used except for the Si:Ln ratio (2:1). 4 samples were synthesized with Gd/Er/Yb ratios: 80/5/15, 80/4/16, 80/6,67/12,33, 85/5/10.

Powder XRD

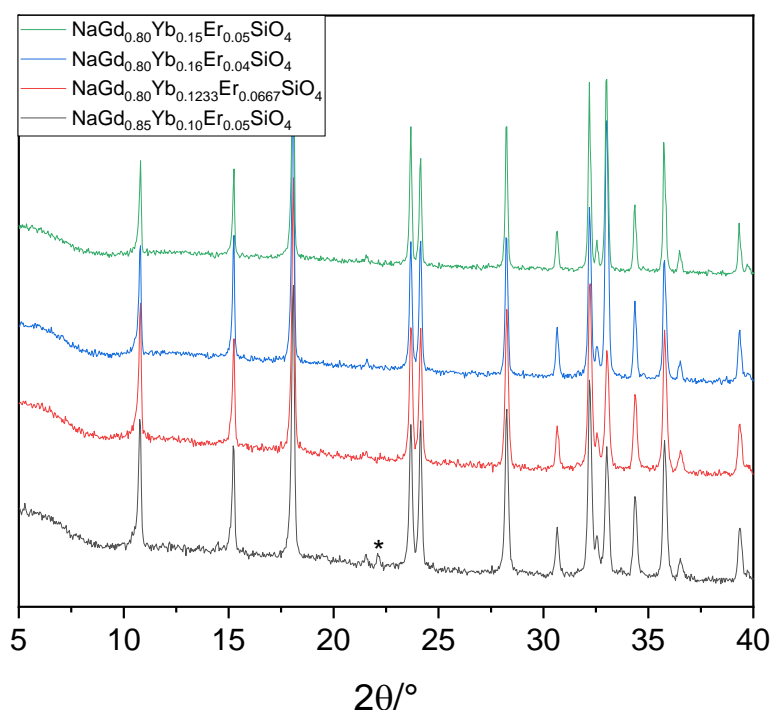


Figure 22: Powder XRD patterns of Na[LnSiO₄] with Ln = Gd, Er, Yb samples with Si:Ln ratio of 2:1. (*) depicts an impurity.

In all synthesis, the target phase is obtained, even if the compound NaGd_{0.80}Yb_{0.15}Eu_{0.05}SiO₄ is not pure.

SEM

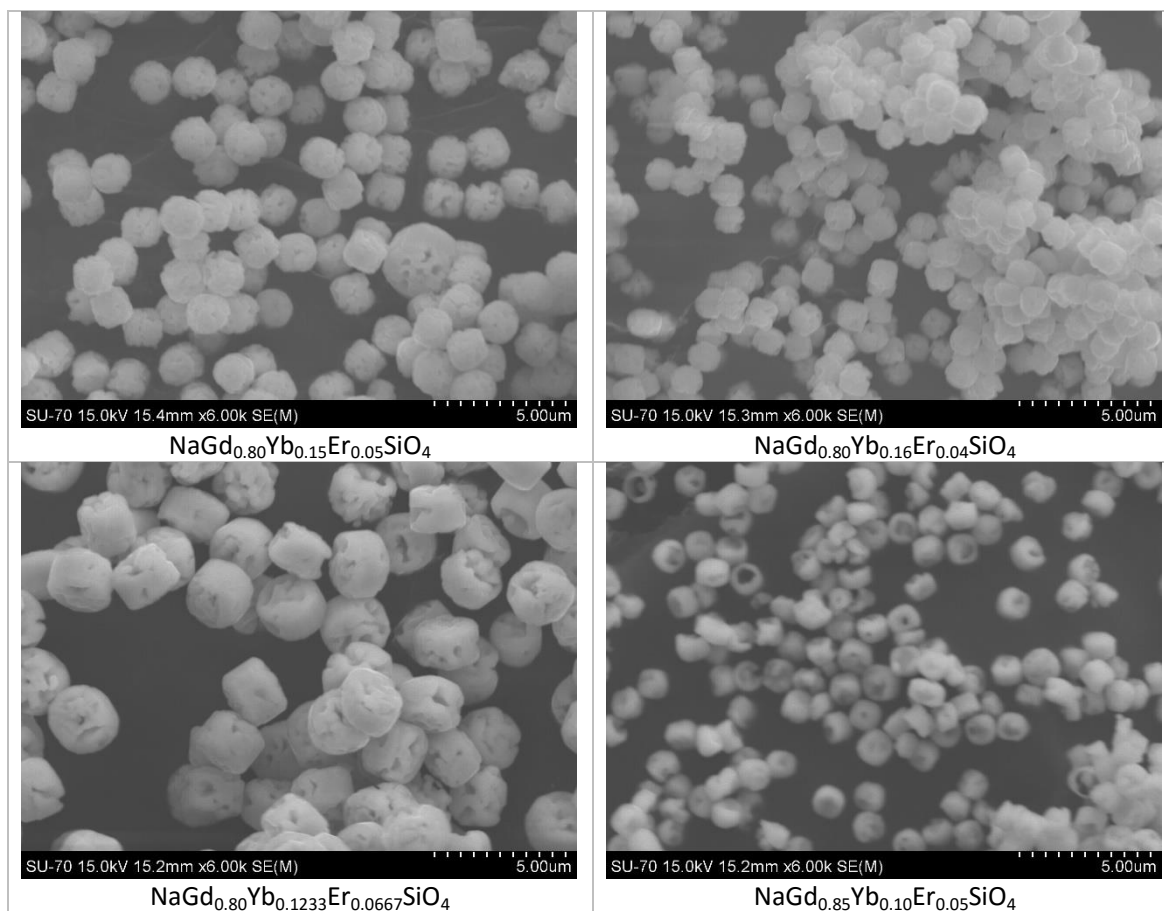


Figure 23 : SEM images of the $\text{Na}[\text{LnSiO}_4]$ with $\text{Ln} = \text{Gd}, \text{Er}, \text{Yb}$.

The SEM images show spherical and disc type habits with a narrow size distribution for all samples. The average particle size is 1-1.5 μm , for $\text{NaGd}_{0.80}\text{Yb}_{0.15}\text{Er}_{0.05}\text{SiO}_4$, $\text{NaGd}_{0.80}\text{Yb}_{0.16}\text{Er}_{0.04}\text{SiO}_4$ and $\text{NaGd}_{0.85}\text{Yb}_{0.10}\text{Er}_{0.05}\text{SiO}_4$. $\text{NaGd}_{0.80}\text{Yb}_{0.1233}\text{Er}_{0.0667}\text{SiO}_4$ particles are 2–3 μm . Except for $\text{NaGd}_{0.80}\text{Yb}_{0.16}\text{Er}_{0.04}\text{SiO}_4$, the crystals have many defects.

3.1.7- NaYSiO_4

In order to be able to record ^{29}Si NMR spectra, the material was synthesized with yttrium to obtain a diamagnetic compound. The material was prepared using 'Synthesis G'.

Powder XRD

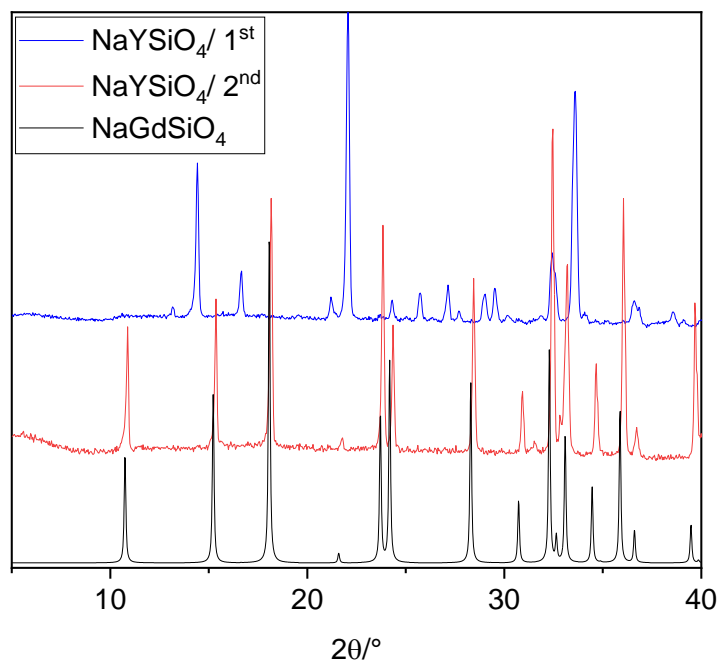


Figure 24 : Powder XRD patterns of $\text{NaYSiO}_4/1^{\text{st}}$ for the first synthesis and $\text{NaYSiO}_4/2^{\text{nd}}$ for the second synthesis. The simulated pattern of tetragonal NaGdSiO_4 is also shown (ICSD 16188) [29].

A first synthesis was realised in the following condition: 5:1 Si:Ln ratio, 1:14 Si:Na ratio, 245 °C, 4 days (see 'Synthesis G' in annex 1.2), and the product gave the XRD pattern $\text{NaYSiO}_4/1^{\text{st}}$ in figure 24 - a phase different from the target solid was obtained. Thus, a new synthesis was realised in the same conditions but with Si:Ln ratio of 2:1 and the target phase was obtained without impurity.

SEM

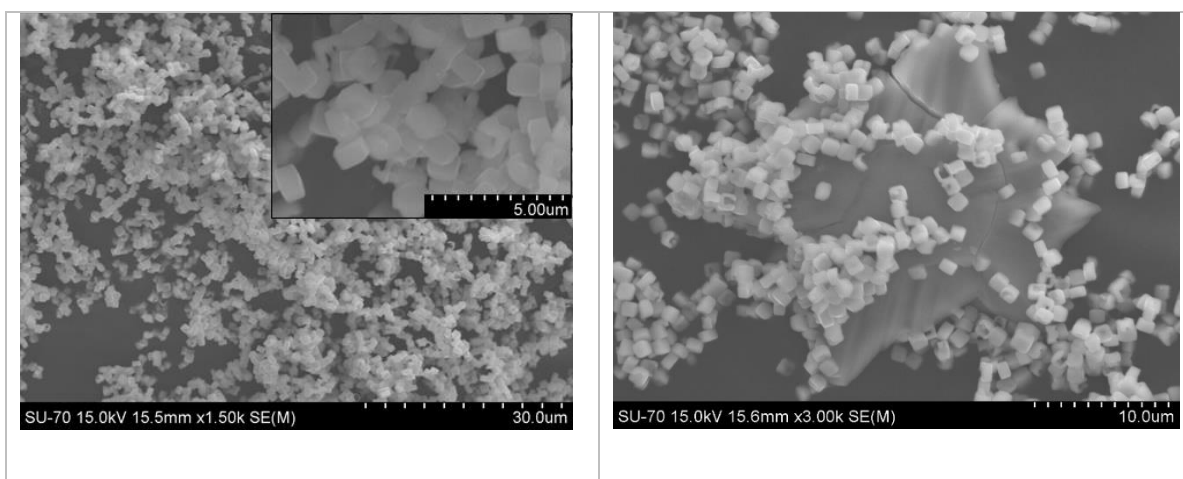


Figure 25: SEM images of NaYSiO_4 .

The SEM images of NaYSiO_4 show the presence of two phase, one comprising cuboid crystals with a narrow size distribution around 1 μm ,and the other an impurity that seems to be amorphous.

3.2 RAMAN AND INFRARED SPECTROSCOPIES

The infrared and Raman bands match closely those reported for NaSmSiO₄-0.25NaF that crystallizes in the tetragonal system, space group $I\bar{4}$ (S_4^2) [26]. The bands are assigned to the vibrations of the SiO₄ groups, which exhibit four normal modes of vibrations with three different symmetries: A₁(v₁), E(v₂) and F₂(v₃ and v₄).

3.2.1- Raman spectroscopy

All the vibrations modes of SiO₄ groups are Raman active.

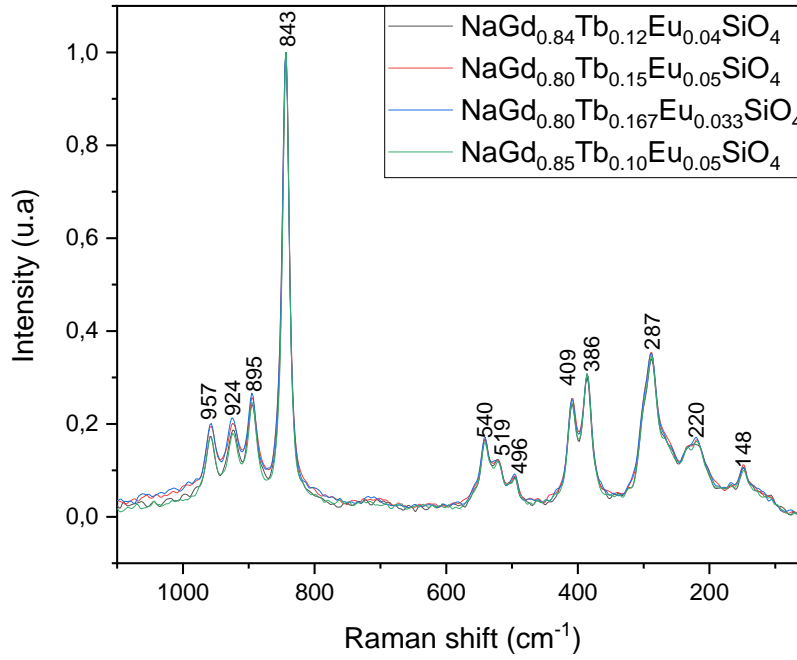


Figure 26 : Raman spectra of Na[(Gd_{0.84}Tb_{0.12}Eu_{0.04})SiO₄], of Na[(Gd_{0.80}Tb_{0.15}Eu_{0.05})SiO₄], of Na[(Gd_{0.80}Tb_{0.167}Eu_{0.033})SiO₄] and of Na[(Gd_{0.85}Tb_{0.10}Eu_{0.05})SiO₄].

The intense 843 cm⁻¹ band is assigned to the symmetric stretching mode v₁. The two bands at 386 and 409 cm⁻¹ are assigned to the symmetric bending mode v₂. The asymmetric stretching mode v₃ is found in the 887-995 cm⁻¹, therefore the bands at 895, 924 and 957 cm⁻¹ matches the v₃ frequency mode. Finally, the asymmetric bending mode v₄ is assigned to the bands at 540, 519 and 496 cm⁻¹[26]. The bands at 287, 220 and 148 cm⁻¹ may be vibrations related to Si-O-Ln bending [30], [31].

3.2.2- Infrared spectroscopy

In contrast with Raman, only the vibration modes ν_3 and ν_4 are in the infrared.

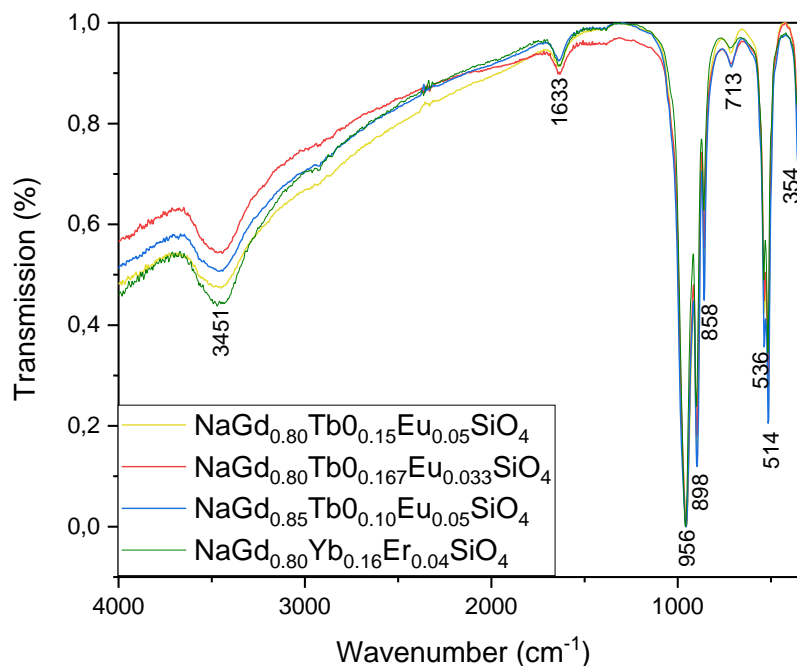


Figure 27: Infrared spectra of $\text{Na}[(\text{Gd}_{0.80}\text{Tb}_{0.15}\text{Eu}_{0.05})\text{SiO}_4]$, $\text{Na}[(\text{Gd}_{0.80}\text{Tb}_{0.167}\text{Eu}_{0.033})\text{SiO}_4]$, $\text{Na}[(\text{Gd}_{0.85}\text{Tb}_{0.10}\text{Eu}_{0.05})\text{SiO}_4]$ and $\text{Na}[(\text{Gd}_{0.80}\text{Yb}_{0.16}\text{Er}_{0.04})\text{SiO}_4]$.

The most intense bands correspond to the vibrations of the free SiO_4 group, ν_3 and ν_4 mode frequencies. Bands, at 898, 965 cm^{-1} are assigned to the asymmetric stretching mode ν_3 , as well as the small shoulder at 1033 cm^{-1} . The other intense bands appearing at 514 and 536 cm^{-1} correspond to the asymmetric bending mode ν_4 . $\text{NaSmSiO}_4\cdot 0.25\text{NaF}$ gives two other bands for this frequency mode at 558 and 495 cm^{-1} , and even though no intense bands are found in the infrared spectra of the $\text{Na}[\text{LnSiO}_4]$ with $\text{Ln} = \text{Gd}, \text{Eu}, \text{Tb}$, small shoulders are seen at 495 and 560 cm^{-1} . The peak at 858 cm^{-1} is assigned to the symmetric stretching mode ν_1 . The band at 354 cm^{-1} is ascribed to vibration ν_2 since the average wave number of this vibration mode for the free SiO_4 groups is around 340 cm^{-1} [26]. The bands at 3451 and 1633 cm^{-1} show the presence of surface water molecules [32]. No match has been found in the literature for the peak at 713 cm^{-1} , but it may be due to vibrations involving the lanthanide ions.

3.3 NMR SPECTROSCOPY

The ^{29}Si NMR spectrum of NaYSiO_4 shows one peak at -72.8 ppm with a shoulder at -75 ppm. Considering SEM results, the shoulder is probably due to an amorphous impurity phase. Therefore, the single peak observed is in accord with the crystal data of the target compound, which calls for the presence of a single Si site.

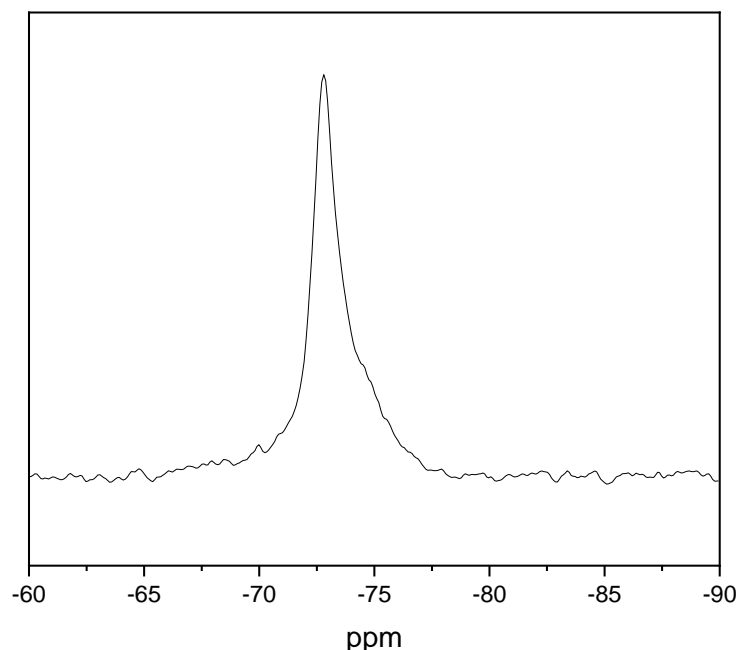


Figure 28: ^{29}Si MAS NMR spectrum of NaYSiO_4 .

3.4 PHOTOLUMINESCENCE CHARACTERIZATION

3.4.1 Photoluminescence characterization of $\text{NaGd}_{0.9}\text{Eu}_{0.1}\text{SiO}_4$, $\text{NaGd}_{0.5}\text{Eu}_{0.5}\text{SiO}_4$, NaEuSiO_4 and $\text{NaGd}_{0.9}\text{Tb}_{0.1}\text{SiO}_4$

The excitation spectra of $\text{NaGd}_{0.9}\text{Eu}_{0.1}\text{SiO}_4$ were recorded at room temperature (294 K) and 12 K, monitoring the strongest $\text{Eu}^{3+} {}^5\text{D}_0 \rightarrow {}^7\text{F}_2$ emission transition (Fig. 29). A broad UV band dominates the spectra, ranging from 210 to 270 nm, this broad band is tentatively attributed to the interconfigurational spin-forbidden $4f^6 \rightarrow 4f^5 5d^1$. The sharp lines (Fig. 29) are attributed to the typical excited levels of the Eu^{3+} ion and to ${}^7\text{S}_{7/2} \rightarrow {}^6\text{I}_{9/2, 11/2, 13/2}$ excited transitions of the Gd^{3+} originated from the Gd^{3+} -to- Eu^{3+} energy transfer [33].

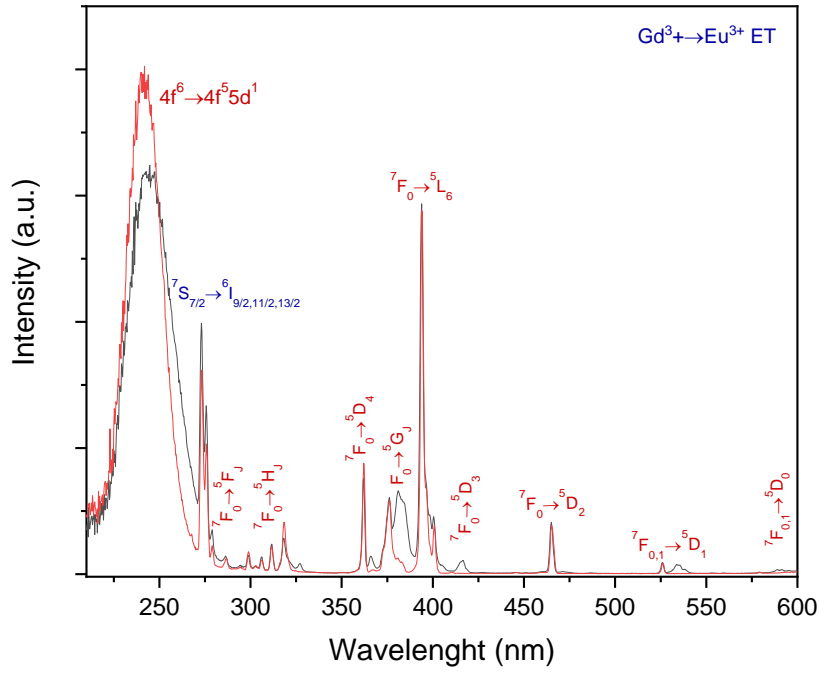


Figure 29: Excitation spectra of $\text{NaGd}_{0.9}\text{Eu}_{0.1}\text{SiO}_4$ ($\lambda_{\text{Em}}=614.5 \text{ nm}$) recorded at room temperature (black line) and 12 K (red line).

The emission spectra of $\text{NaGd}_{0.9}\text{Eu}_{0.1}\text{SiO}_4$ were recorded at room temperature (294 K) and 12 K, with the excitation fixed at 394 nm (Fig 30). The sharp Eu^{3+} emission lines are assigned to the typical $^5\text{D}_0 \rightarrow ^7\text{F}_{0-4}$ transitions [33]. The presence of a single $^5\text{D}_0 \rightarrow ^7\text{F}_0$ transition, and the ligand field split of the $^5\text{D}_0 \rightarrow ^7\text{F}_1$ and $^5\text{D}_0 \rightarrow ^7\text{F}_2$ transitions into, respectively, three and four Stark components indicates the presence of a single Eu^{3+} environment [25], [34], in perfect agreement in with the crystal structure of the tetragonal NaGdSiO_4 .

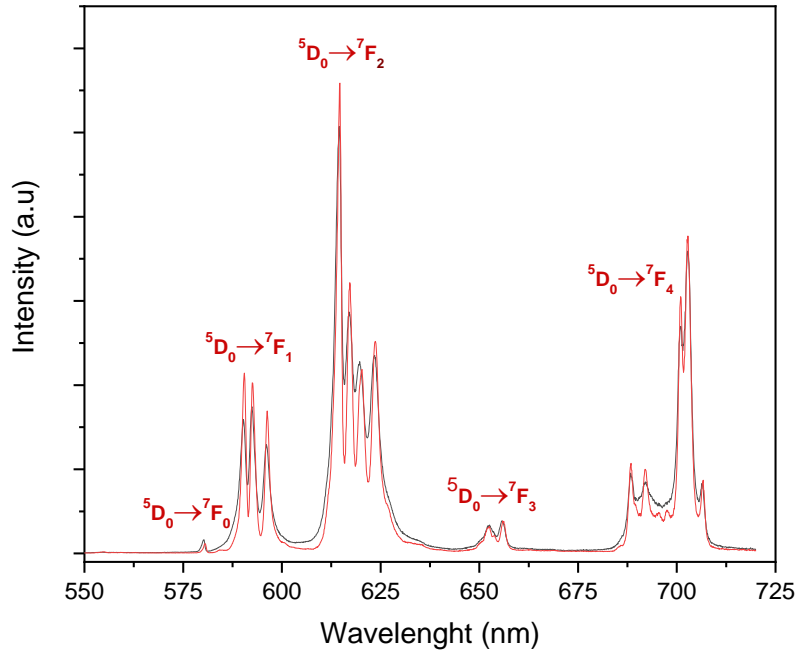


Figure 30 : Emission spectra of $\text{NaGd}_{0.9}\text{Eu}_{0.1}\text{SiO}_4$ ($\lambda_{\text{Ext.}} = 394 \text{ nm}$) recorded 294 K (black) and 12 K (red).

The $^5\text{D}_0$ decay curves of $\text{NaGd}_{0.9}\text{Eu}_{0.1}\text{SiO}_4$ for 12 K and room temperature are shown in Fig 31. These decay curves were fitted with first order exponential decay functions, yielding lifetimes of $0.98 \pm 0.01 \text{ ms}$ (12 K) and $0.82 \pm 0.01 \text{ ms}$ (294 K), confirming the presence of a single Eu^{3+} local site. The 16% decrease of the lifetime determined at 294 K relatively to the one at 12 K is due to thermal quenching, leading to stronger non-radiative emission processes.

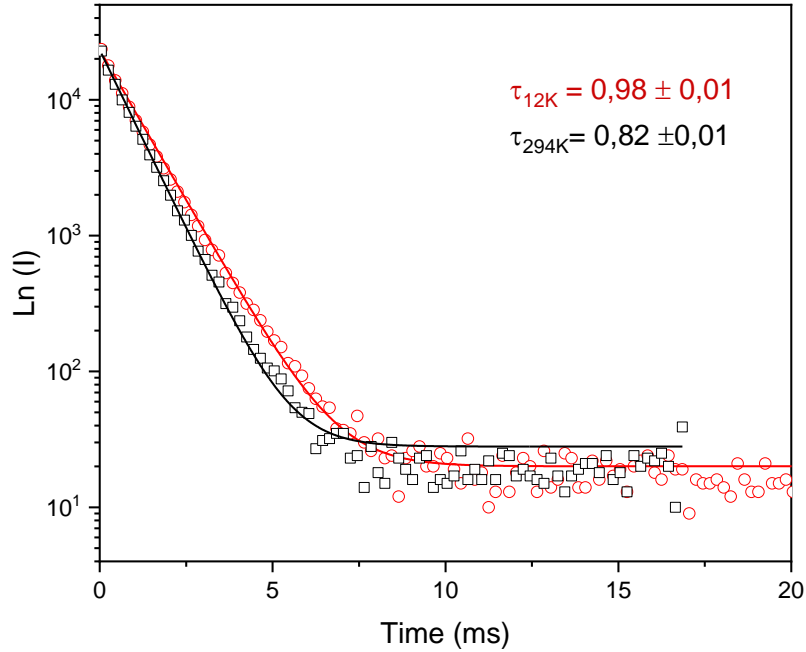


Figure 31 : $^5\text{D}_0$ decay curves of $\text{NaGd}_{0.9}\text{Eu}_{0.1}\text{SiO}_4$ recorded at 294 K (black) and 12 K (red) with excitation at 394 nm and emission at 614.5 nm. The solid lines are the best fits to a first order exponential decay functions ($I = I_0 + A_1 e^{-x/\tau}$).

Fig 32 compares the excitation spectrum of $\text{NaGd}_{0.9}\text{Eu}_{0.1}\text{SiO}_4$, $\text{NaGd}_{0.5}\text{Eu}_{0.50}\text{SiO}_4$ and NaEuSiO_4 recorded at 294 K, monitoring the strongest $\text{Eu}^{3+} {}^5\text{D}_0 \rightarrow {}^7\text{F}_2$ emission line at 614.5 nm. The broad UV bands of $\text{NaGd}_{0.5}\text{Eu}_{0.50}\text{SiO}_4$ and NaEuSiO_4 samples are sharply wider than the one of $\text{NaGd}_{0.9}\text{Eu}_{0.1}\text{SiO}_4$ which was attributed to interconfigurational spin-forbidden $4f^6 \rightarrow 4f^5 5d^1$ transition. This fact suggests also the presence of charge-transfer between the O^{2-} ligand and the Eu^{3+} , presumably partially overlapping with the $4f^6 \rightarrow 4f^5 5d^1$ transition. The relative intensity of the Eu^{3+} intra 4f excited sharp lines increases in accordance with the Eu^{3+} concentration [33]. As expected, the ${}^7\text{S}_{7/2} \rightarrow {}^6\text{I}_{9/2, 11/2, 13/2}$ excited transitions of the Gd^{3+} is more relevant for the $\text{NaGd}_{0.9}\text{Eu}_{0.1}\text{SiO}_4$, and is absent for the pure NaEuSiO_4 .

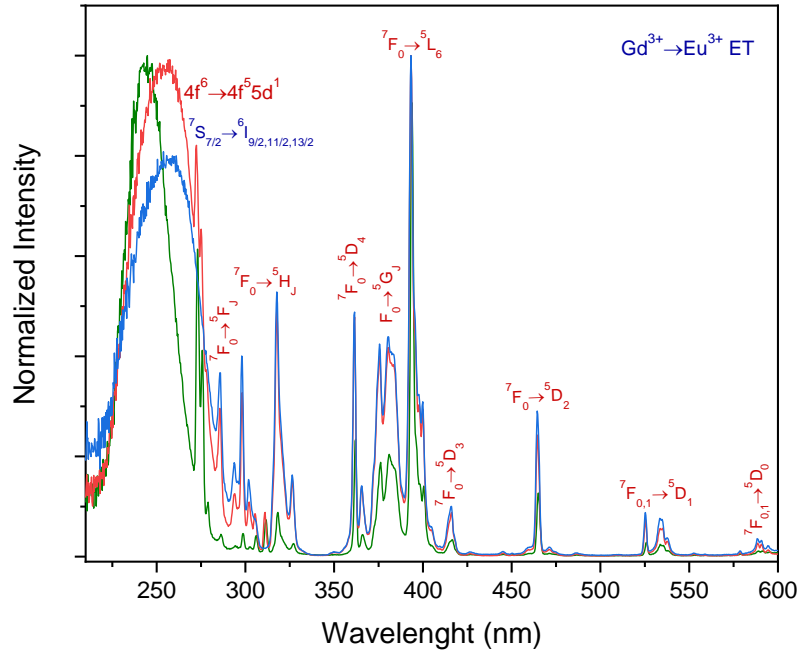


Figure 32: Excitation spectra of $\text{NaGd}_{0.9}\text{Eu}_{0.1}\text{SiO}_4$ (green line), $\text{NaGd}_{0.5}\text{Eu}_{0.50}\text{SiO}_4$ (red line) and NaEuSiO_4 (blue line) ($\lambda_{\text{em}}=614.5$ nm).

Fig. 33 shows the emission spectra of $\text{NaGd}_{0.9}\text{Eu}_{0.1}\text{SiO}_4$, $\text{NaGd}_{0.5}\text{Eu}_{0.50}\text{SiO}_4$ and NaEuSiO_4 recorded at 294 K with the excitation fixed at 394 nm. All these spectra present an identical profile, even the relative intensities of the corresponding Stark components did not change with the Eu^{3+} concentration of the samples. This is in accordance with the presence of a unique Eu^{3+} center in the tetragonal NaLnSiO_4 pure samples.

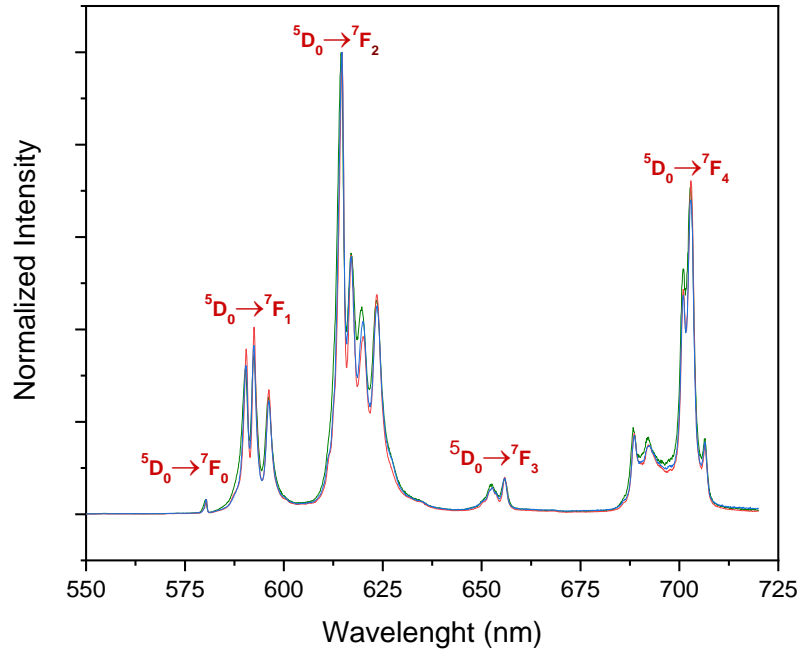


Figure 33: Emission spectra of $\text{NaGd}_{0.9}\text{Eu}_{0.1}\text{SiO}_4$ (green line), $\text{NaGd}_{0.5}\text{Eu}_{0.5}\text{SiO}_4$ (red) and NaEuSiO_4 (blue) ($\lambda_{\text{em}}=394 \text{ nm}$).

To demonstrate the dependence of emission efficiency on the Eu^{3+} concentration, the $^5\text{D}_0$ decay curves of $\text{NaGd}_{0.9}\text{Eu}_{0.1}\text{SiO}_4$, $\text{NaGd}_{0.5}\text{Eu}_{0.5}\text{SiO}_4$ and NaEuSiO_4 were recorded at room temperature (Fig. 34). The decay curves of the two former samples are well fitted by first-order exponential decay function and yield similar lifetimes of $0.82 \pm 0.01 \text{ ms}$ and $0.73 \pm 0.01 \text{ ms}$, respectively. However, the NaEuSiO_4 decay curve is only properly fitted by a second-order exponential decay function with an estimated averaged lifetime of $0.35 \pm 0.02 \text{ ms}$. The changes on NaEuSiO_4 decay curve profile, from mono-exponential to not mono-exponential, and the strong decrease of the determined lifetime relatively to the more diluted $\text{NaGd}_{0.9}\text{Eu}_{0.1}\text{SiO}_4$ sample, results from the well-known concentration quenching effect and demonstrates a self-energy migration between adjacent Eu^{3+} ions. This self-energy migration is strongly reduced for the Eu^{3+} concentration below 50%.

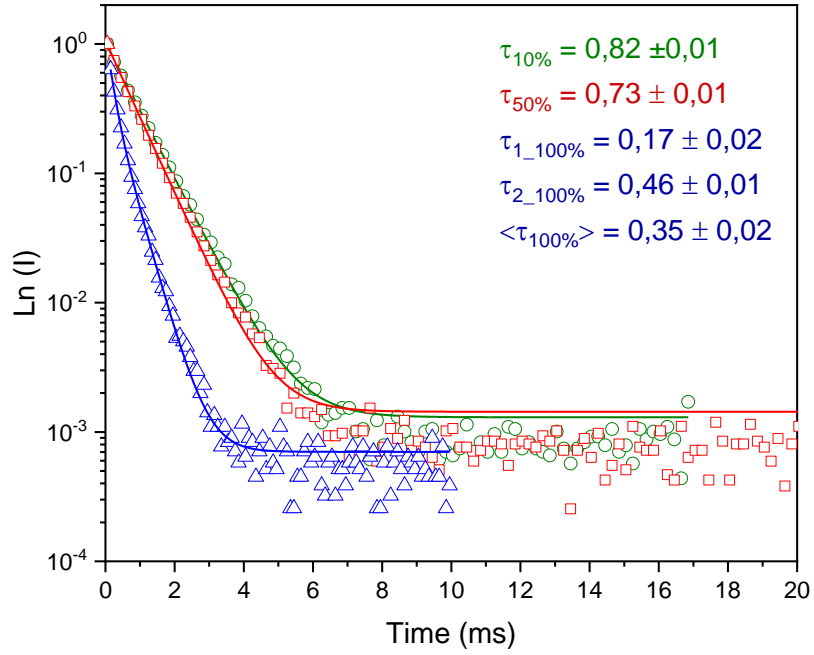


Figure 34 : 5D_0 decay curves of $\text{NaGd}_{0.9}\text{Eu}_{0.1}\text{SiO}_4$ (green), $\text{NaGd}_{0.5}\text{Eu}_{0.5}\text{SiO}_4$ (red) and NaEuSiO_4 (blue) recorded at 294 K, with excitation at 394 nm and emission at 614.5 nm. The solid lines are the best fits to first order ($I = I_0 + A_1 e^{-x/\tau}$) and second-order ($I = I_0 + A_1 e^{-x/\tau} + A_2 e^{-x/\tau}$) decay functions. The average lifetime is defined as $(A_1 \tau_1^2 + A_2 \tau_2^2) / (A_1 \tau_1 + A_2 \tau_2)$.

The photographs of $\text{NaGd}_{1-x}\text{Eu}_x\text{SiO}_4$ with $x=0.10$, 0.50 and 1 show the brightness of the sample emission as a function of the Eu^{3+} concentration (Fig 35). The brightness of the samples is in accordance to the corresponding 5D_0 decay curves (Fig 34). It increases from the 10% to 50% Eu^{3+} sample, where the lifetime is almost maintained, and strongly decreases for the 100% Eu^{3+} sample for which the 5D_0 decay curve demonstrates the self-energy migration associated with the concentration quenching effect.

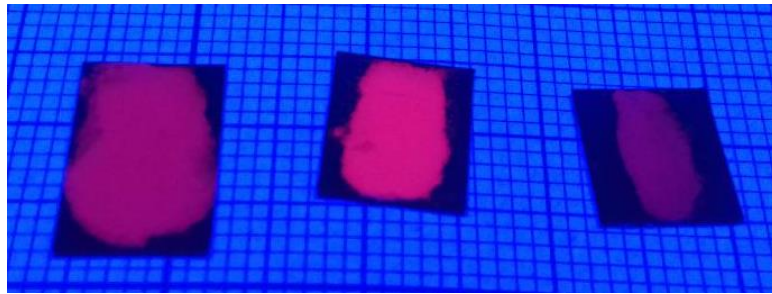


Figure 35: Photographs, from left to right, $\text{NaGd}_{0.9}\text{Eu}_{0.1}\text{SiO}_4$, $\text{NaGd}_{0.5}\text{Eu}_{0.5}\text{SiO}_4$ and NaEuSiO_4 luminescence under an excitation wavelength of 254 nm.

The excitation spectra of $\text{NaGd}_{0.9}\text{Tb}_{0.1}\text{SiO}_4$ recorded at 294 K and 12 K, monitoring the strongest Tb^{3+} $^5\text{D}_4 \rightarrow ^7\text{F}_5$ emission at 543.5 nm are presented in Fig. 37. A broad UV band dominates the spectra, ranging from 220 to 265 nm. This band is attributed to the interconfigurational spin-forbidden $4f^8 \rightarrow 4f^6 5d^1$, whereas the sharp lines around 275 nm are attributed to the $^7\text{S}_{7/2} \rightarrow ^6\text{I}_{9/2, 11/2, 13/2}$ excited transitions of the Gd^{3+} , originated from the Gd^{3+} -to- Tb^{3+} energy transfer, and the sharp lines between 300 nm and 490 nm are attributed to the typical emission lines of the Tb^{3+} ion [33].

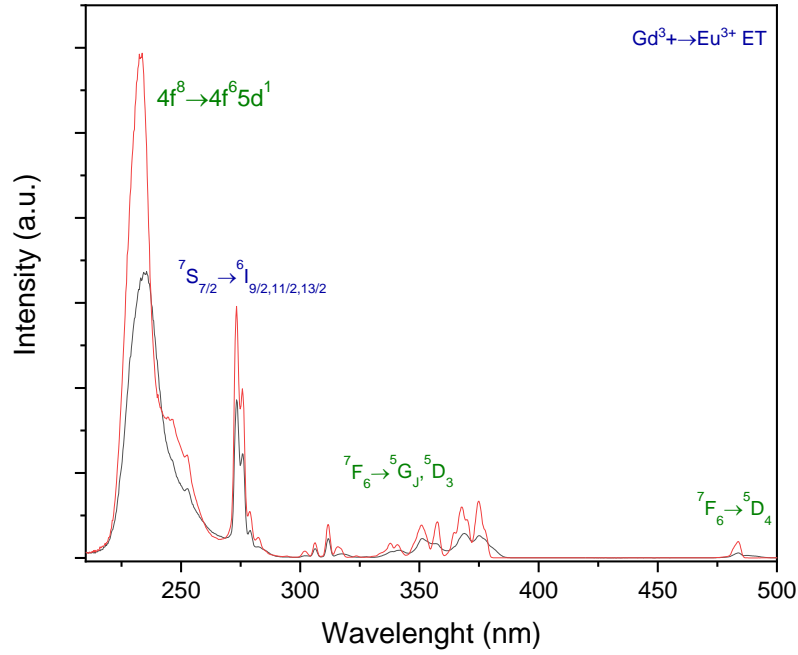


Figure 36: Excitation spectra of $\text{NaGd}_{0.9}\text{Tb}_{0.1}\text{SiO}_4$ ($\lambda_{\text{Em}} = 543.5$ nm) recorded at room temperature (black line) and 12 K (red line).

The emission spectra of $\text{NaGd}_{0.9}\text{Tb}_{0.1}\text{SiO}_4$ recorded at room temperature (ca. 294 K) and 12 K, excited at 375 nm, are presented in Fig. 37. The sharp Tb^{3+} emission lines are assigned to the typical $^5\text{D}_4 \rightarrow ^7\text{F}_{0-6}$ transitions [33]. At high temperature the emission intensities are weaker due to thermal quenching.

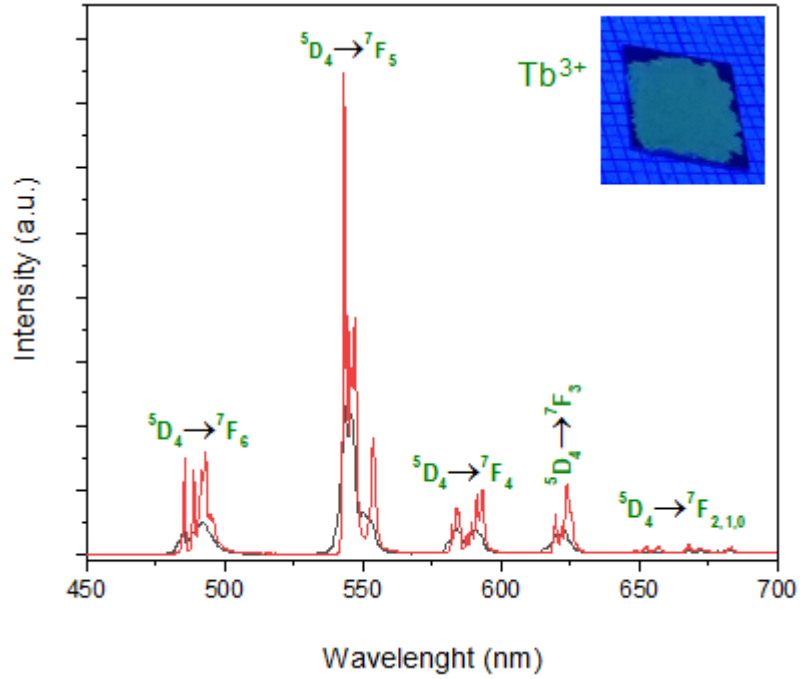


Figure 37: Emission spectra of $\text{NaGd}_{0.9}\text{Tb}_{0.1}\text{SiO}_4$ ($\lambda_{\text{Ext}} = 375 \text{ nm}$) recorded at 294 K (black line) and 12 K (red line). The inset depicts, a photograph of $\text{NaGd}_{0.9}\text{Tb}_{0.1}\text{SiO}_4$ under 254 nm irradiation.

The $^5\text{D}_4$ decay curves of $\text{NaGd}_{0.9}\text{Tb}_{0.1}\text{SiO}_4$ recorded 12 K and 294 K (Fig. 38) were fitted with a first-order exponential decay function, yielding lifetimes of $2.06 \pm 0.01 \text{ ms}$ and $1.79 \pm 0.01 \text{ ms}$, respectively. Thus, from 12 K to 294 K the emission lifetime decreases only 13% due to the thermal quenching promoted higher non-radiative emission processes.

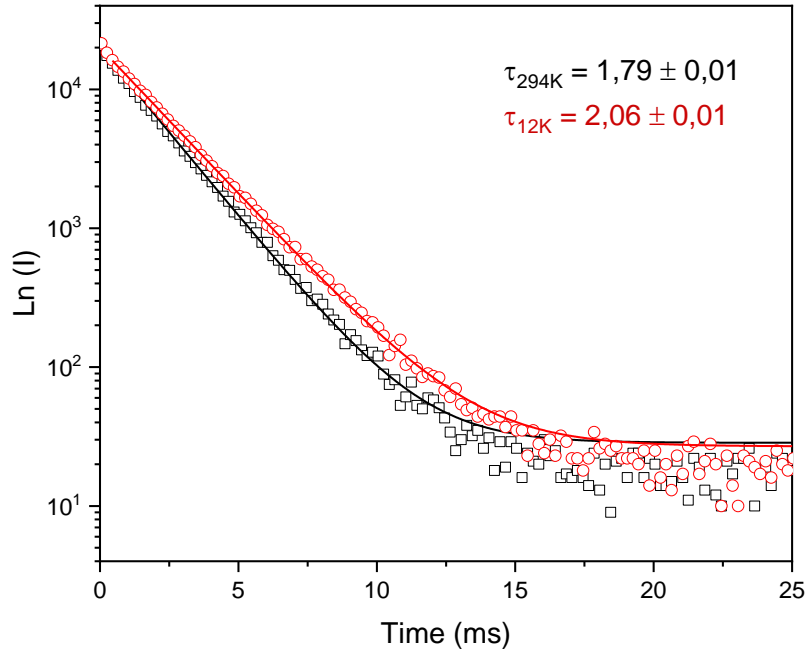


Figure 38 : $^5\text{D}_4$ decay curves of $\text{NaGd}_{0.9}\text{Tb}_{0.1}\text{SiO}_4$ recorded at 294K (black) and 12K (red) with excitation at 375 nm and emission at 543.5 nm. The solid lines are the best fits to first-order exponential functions ($I = I_0 + A_1 e^{-x/\tau}$).

3.4.2 Visible ratiometric luminescent thermometers

The emission spectra of several mixed $\text{Gd}^{3+}/\text{Tb}^{3+}/\text{Eu}^{3+}$ samples were recorded at room-temperature (Fig. 39) with the aim to select the most promising for the visible ratiometric luminescent thermometry. Under excitation at 368 nm ($^5\text{G}_6$ excited level of Tb^{3+}), all these samples display the characteristic emission transitions of Eu^{3+} and Tb^{3+} [25], [35]. It is evident that, the relative intensities of the Eu^{3+} and Tb^{3+} emissions are very sensitive to the corresponding Ln^{3+} contents presented on the compounds. $\text{NaGd}_{0.82}\text{Tb}_{0.135}\text{Eu}_{0.045}\text{SiO}_4$ presents the best balance between the Tb^{3+} and Eu^{3+} emissions, whereas the $\text{NaGd}_{0.666}\text{Tb}_{0.167}\text{Eu}_{0.167}\text{SiO}_4$ sample presents the lower relative Tb^{3+} emission. It is also clear that, the concentration decreases of the optically active Eu^{3+} and Tb^{3+} , for samples with identical $\text{Tb}^{3+}/\text{Eu}^{3+}$ ratios ($\text{NaGd}_{0.666}\text{Tb}_{0.167}\text{Eu}_{0.167}\text{SiO}_4$ and $\text{NaGd}_{0.82}\text{Tb}_{0.09}\text{Eu}_{0.09}\text{SiO}_4$ samples), induces a relative increase of the Tb^{3+} emission, resulting from a decrease of the Tb^{3+} -to- Eu^{3+} energy transfer process due to the increase of averaged distances between neighbouring Eu^{3+} and Tb^{3+} .

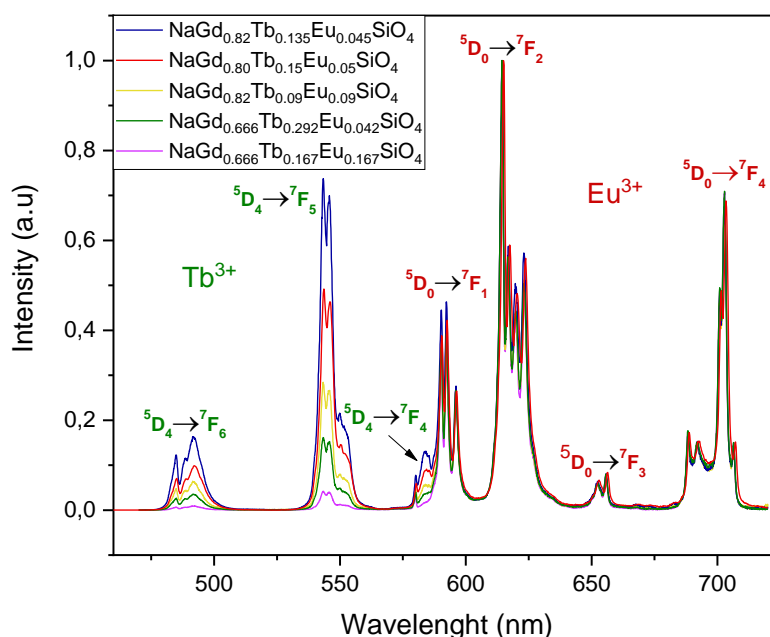


Figure 39: Room-temperature emission spectra of compounds NaLnSiO_4 with $\text{Ln}=\text{Gd}, \text{Tb}, \text{Eu}$, under excitation at 368 nm.

To have an efficient thermometer a compound with maximized intensity variation of Eu^{3+} and Tb^{3+} transitions with temperature changes is needed. In a $\text{Tb}^{3+}/\text{Eu}^{3+}$ mixed system the Tb^{3+} transition intensities it is expected to decrease with increasing temperature due to thermally activated Tb^{3+} -to- Eu^{3+} energy transfer process. In the present work, $\text{Na}[(\text{Gd}_{0.666}\text{Tb}_{0.292}\text{Eu}_{0.042})\text{SiO}_4]$ and $\text{Na}[(\text{Gd}_{0.82}\text{Tb}_{0.135}\text{Eu}_{0.045})\text{SiO}_4]$ samples were selected to be evaluated as ratiometric luminescent thermometers. At room-temperature these samples shows, respectively, the second worse and the best balance between the Tb^{3+} and Eu^{3+} emissions (See Fig. 39).

Under UV irradiation (254 nm) the mixed Tb³⁺/Eu³⁺ samples display different emitting colour tone (Fig. 40) which depending in the Tb/Eu composition can approach from the red Eu³⁺ to the green Tb³⁺ emissions.



Figure 40: Photographs, from left to right, NaGd_{0.90}Eu_{0.10}SiO₄, NaGd_{0.82}Tb_{0.09}Eu_{0.09}SiO₄, NaGd_{0.82}Tb_{0.135}Eu_{0.045}SiO₄ and NaGd_{0.90}Tb_{0.10}SiO₄ luminescence under an excitation wavelength of 254 nm.

Fig. 41 shows the excitation spectra of Na[(Gd_{0.82}Tb_{0.135}Eu_{0.045})SiO₄] recorded at 294 K and 12 K, monitoring the strongest Eu³⁺ ⁵D₀→⁷F₂ and Tb³⁺ ⁵D₄→⁷F₅ emission lines. Broad UV bands dominates these spectra, ranging from ca. 220 to 270 nm. Such bands are attributed to the interconfigurational spin-forbidden 4f⁸→4f⁷5d¹ of Tb³⁺ and 4f⁶→4f⁵5d¹ of Eu³⁺ for the spectra monitored at the Eu³⁺ emission. For the 12 K excitation spectrum monitoring the Tb³⁺ emission, the broad band shows a resolved shoulder in the low energy range which can be attributed to the spin-allowed interconfigurational 4f⁸→4f⁷5d¹ transition of Tb³⁺. The additional sharp lines are attributed to the typical intra-4f excited transitions of Eu³⁺ and Tb³⁺ for the spectra monitored at the Eu³⁺ emission and only the Tb³⁺ excited transitions for the spectra monitor at the Tb³⁺ emission [33]. This clearly shows the Tb³⁺-to-Eu³⁺ energy transfer, which is slightly more efficient at room temperature than at 12 K. Around 275 nm the ⁸S_{7/2}→⁶I_{9/2,11/2,13/2}, Gd³⁺ transitions can be seen in both spectra, which are due to the Gd³⁺-to-Eu³⁺ and/or Gd³⁺-to-Tb³⁺ energy transfer processes [25].

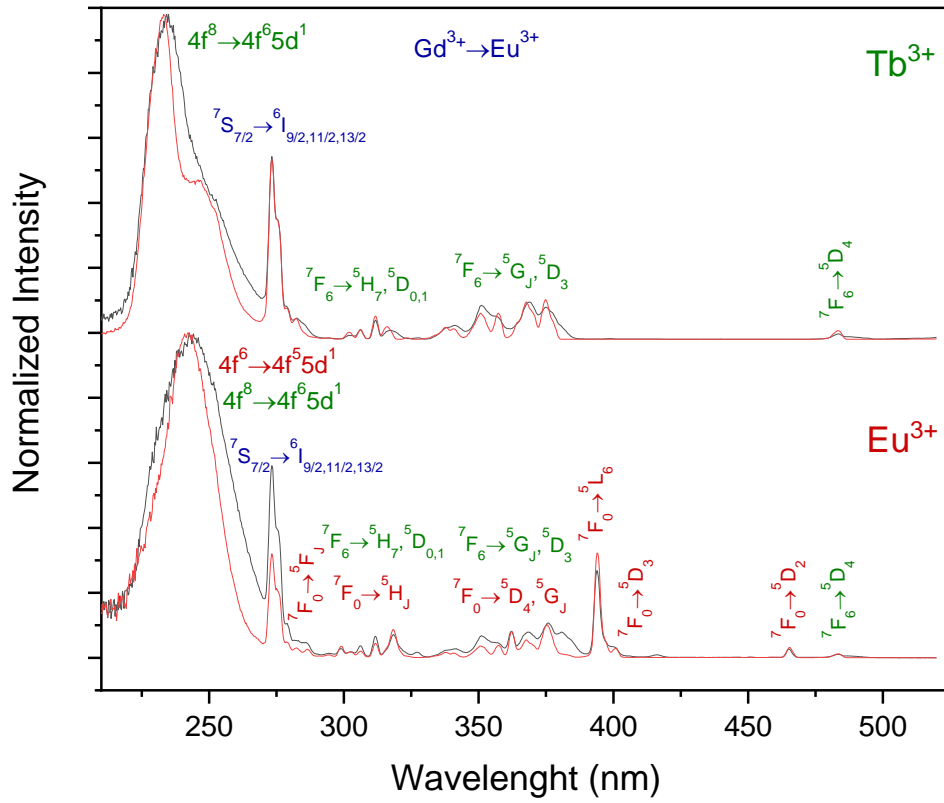


Figure 41: Excitation spectra of $\text{Na}[(\text{Gd}_{0.82}\text{Tb}_{0.135}\text{Eu}_{0.045})\text{SiO}_4]$ at 294 K (black lines) and 12 K (red lines) with the emission fixed at 614.5 nm (bottom) and 543.5 nm (top).

Next, we have assessed the potential of $\text{Na}[(\text{Gd}_{0.666}\text{Tb}_{0.292}\text{Eu}_{0.042})\text{SiO}_4]$ and $\text{Na}[(\text{Gd}_{0.82}\text{Tb}_{0.135}\text{Eu}_{0.045})\text{SiO}_4]$ to be used as visible ratiometric luminescent thermometers. The integrated areas of $^5\text{D}_4 \rightarrow ^7\text{F}_5$ (I_{Tb}) and $^5\text{D}_0 \rightarrow ^7\text{F}_2$ (I_{Eu}) emission transitions were used to define the thermometric parameter $\Delta = I_{\text{Tb}} / I_{\text{Eu}}$ (see eq. 4) and to convert the emission intensities into absolute temperature through the calibration curve (see below). The emission intensity was monitored in the range 12 K – 450 K and 12 K– 410 K for $\text{Na}[(\text{Gd}_{0.666}\text{Tb}_{0.292}\text{Eu}_{0.042})\text{SiO}_4]$ and $\text{Na}[(\text{Gd}_{0.82}\text{Tb}_{0.135}\text{Eu}_{0.045})\text{SiO}_4]$, respectively, with the excitation fixed at 375 nm (Fig. 42).

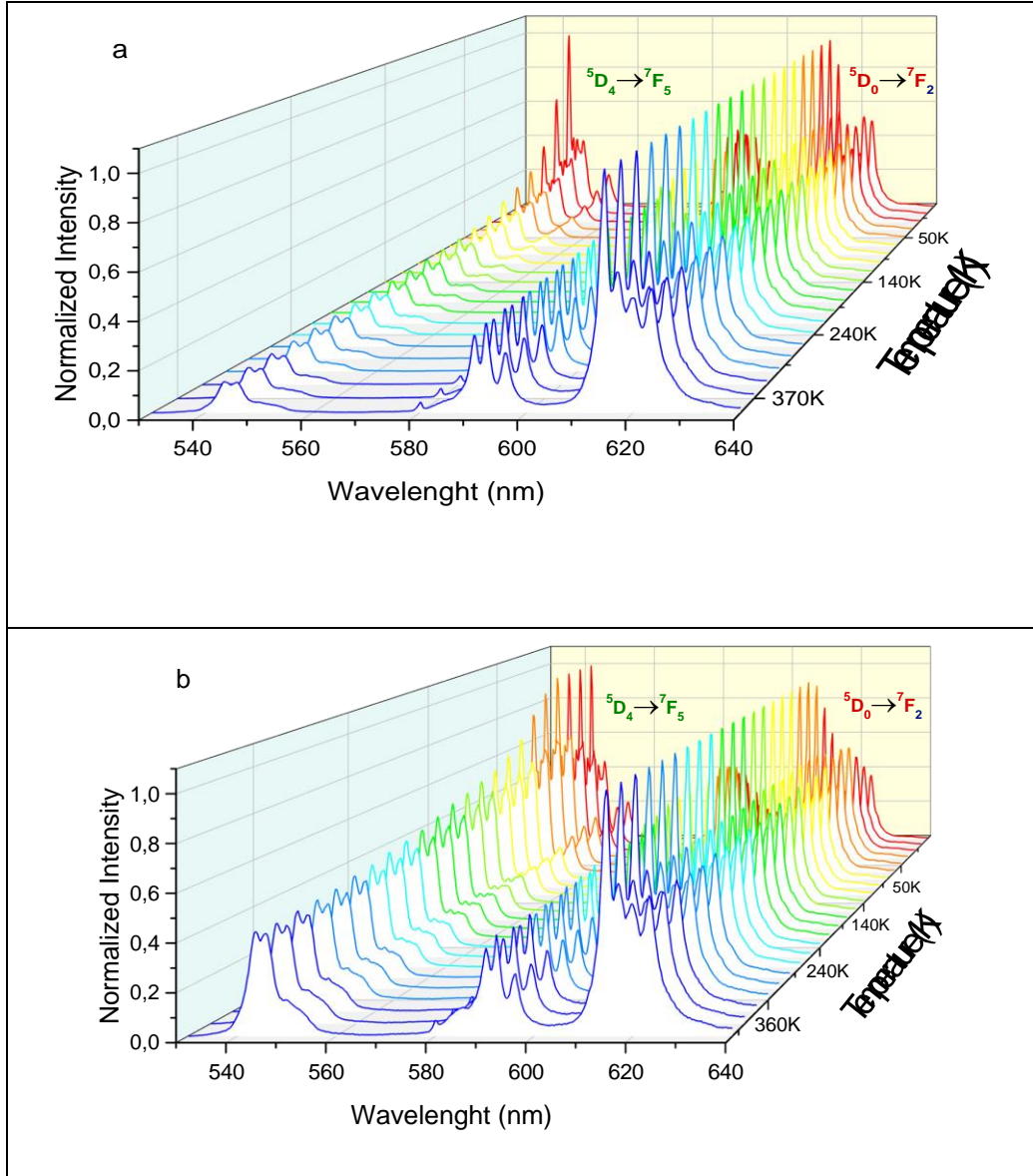


Figure 42: a) Emission spectra of $\text{Na}[(\text{Gd}_{0.666}\text{Tb}_{0.292}\text{Eu}_{0.042})\text{SiO}_4]$ in the range 12 – 410 K with the excitation fixed at 375 nm. b) Emission spectra of $\text{Na}[(\text{Gd}_{0.82}\text{Tb}_{0.135}\text{Eu}_{0.045})\text{SiO}_4]$ in the range 12 – 450 K with the excitation fixed at 375 nm.

To determine the average thermometric parameter, four consecutive emission spectra were collected at each temperature. The errors were calculated from the corresponding standard deviation. I_{Tb} and I_{Eu} were calculated by integrating the emission spectra in the 535 nm - 565 nm and 607 nm - 621 nm ranges, respectively. Fig. 43 plots the I_{Tb} and I_{Eu} temperature dependence.

For $\text{Na}[(\text{Gd}_{0.666}\text{Tb}_{0.292}\text{Eu}_{0.042})\text{SiO}_4]$, the Eu^{3+} emission increases in the 12 K – 60 K range reaching at 60 K 1.1 times the 12 K value. Then, the integrated emission decreased attaining at 410 K 78% of the 12 K value. Tb^{3+} emission decreases with increasing temperature, the integrated emission attaining at 410 K, 14% of the 12 K value. However, at 60 K the integrated emission already decreases to 36% of the 12 K value.

For $\text{Na}[(\text{Gd}_{0.82}\text{Tb}_{0.135}\text{Eu}_{0.045})\text{SiO}_4]$, the Eu^{3+} emission increases in the 12 K – 60 K range reaching at 60 K 1.2 times the 12 K value. Then, the integrated emission decreases attaining at 450 K 75% of the 12 K value. Tb^{3+} emission decreases more smoothly than for $\text{Na}[(\text{Gd}_{0.666}\text{Tb}_{0.292}\text{Eu}_{0.042})\text{SiO}_4]$ with increasing temperature, the integrated emission attaining at 450 K, 23% of the 12 K value and at 60 K the integrated emission decreases to only 76% of the 12 K value.

Both samples have a very similar temperature dependence of the integrated emissions, except for the decrease of Tb^{3+} integrated emission, which is more drastic for $\text{Na}[(\text{Gd}_{0.666}\text{Tb}_{0.292}\text{Eu}_{0.042})\text{SiO}_4]$.

The decrease of the Tb^{3+} emission and the increase of the Eu^{3+} emission evidence the thermally activated Tb^{3+} -to- Eu^{3+} energy transfer process. For both samples, the changes in the integrated emission changes poorly for Eu^{3+} .

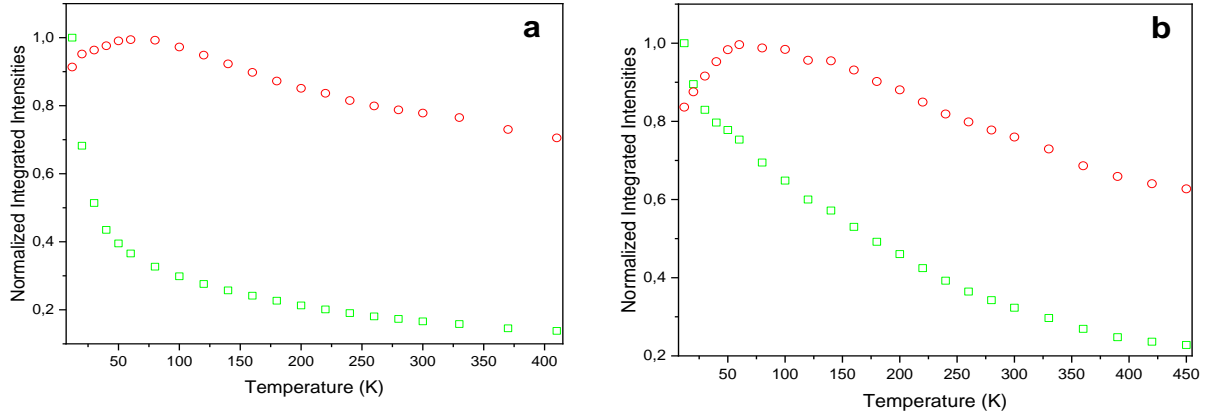


Fig. 43 - Temperature dependence of the I_{Tb} (green) and I_{Eu} (red) parameters of $\text{Na}[(\text{Gd}_{0.666}\text{Tb}_{0.292}\text{Eu}_{0.042})\text{SiO}_4]$ in the range 12K-410K (a) and $\text{Na}[(\text{Gd}_{0.82}\text{Tb}_{0.135}\text{Eu}_{0.045})\text{SiO}_4]$ in the range 12 – 450 K (b) .

Fig. 44 depicts the temperature dependence of the thermometric parameter Δ in the range 12 - 410 K for $\text{Na}[(\text{Gd}_{0.666}\text{Tb}_{0.292}\text{Eu}_{0.042})\text{SiO}_4]$, and 12 – 450 K for $\text{Na}[(\text{Gd}_{0.82}\text{Tb}_{0.135}\text{Eu}_{0.045})\text{SiO}_4]$. The data are described by the classical Mott-Seitz model involving two competitive non-radiative recombination channels [25] :

$$\Delta(T) = \frac{\Delta_0}{1 + \alpha_1 \exp(-\Delta E_1/k_B T) + \alpha_2 \exp(-\Delta E_2/k_B T)} \quad (11)$$

Where Δ_0 is the Δ parameter at $T = 0$ K, $\alpha = W_0/W_R$ is the ratio between the non-radiative (W_0 at $T = 0$ K) and radiative (W_R) rates, and ΔE_1 and ΔE_2 are the activation energies for the two non-radiative channels.

fit of the experimental Δ values with equation 11 yields $\Delta_0 = 1.05 \pm 0.01$; $\alpha_1 = 5.29 \pm 0.04$; $\alpha_2 = 5.83 \pm 0.35$; $\Delta E_1 = 21.5 \pm 0.2 \text{ cm}^{-1}$; $\Delta E_2 = 310 \pm 15 \text{ cm}^{-1}$ for $\text{Na}[(\text{Gd}_{0.666}\text{Tb}_{0.292}\text{Eu}_{0.042})\text{SiO}_4]$ and $\Delta_0 = 2.17 \pm 0.03$;

$\alpha_1 = 1.22 \pm 0.02$; $\alpha_2 = 3.75 \pm 0.12$; $\Delta E_1 = 20.4 \pm 0.8 \text{ cm}^{-1}$; $\Delta E_2 = 282 \pm 9 \text{ cm}^{-1}$ for $\text{Na}[(\text{Gd}_{0.82}\text{Tb}_{0.135}\text{Eu}_{0.045})\text{SiO}_4]$. The non-radiative recombination channels characterized by the activation energy ΔE_2 presumably involves the $\text{Tb}^{3+} {}^5\text{D}_4$ and $\text{Eu}^{3+} {}^5\text{D}_2$ excited levels involved in the Tb^{3+} -to- Eu^{3+} energy transfer. The much smaller activation energy ΔE_1 probably involves energy migration between neighbouring Ln^{3+} ions [25].

The activation energies of $\text{Na}[(\text{Gd}_{0.666}\text{Tb}_{0.292}\text{Eu}_{0.042})\text{SiO}_4]$ are slightly higher than for $\text{Na}[(\text{Gd}_{0.82}\text{Tb}_{0.135}\text{Eu}_{0.045})\text{SiO}_4]$ but still very similar.

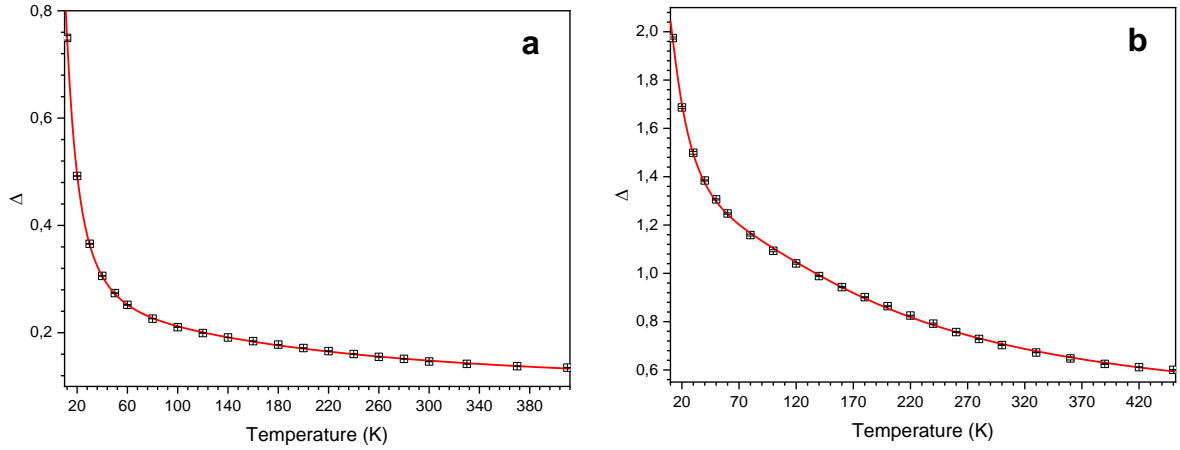


Figure 44: Temperature dependence of the parameter Δ from 12 K to 410 K for $\text{Na}[(\text{Gd}_{0.666}\text{Tb}_{0.292}\text{Eu}_{0.042})\text{SiO}_4]$ (a) and from 12 K to 450 K for $\text{Na}[(\text{Gd}_{0.82}\text{Tb}_{0.135}\text{Eu}_{0.045})\text{SiO}_4]$ (b) excited at 375nm. The solid lines are the calibration curves resulting from the fits considering a Mott-Seitz model.

Figure 45 shows that for $\text{Na}[(\text{Gd}_{0.666}\text{Tb}_{0.292}\text{Eu}_{0.042})\text{SiO}_4]$, the determined relative thermal sensitivity (see eq. 6) shows that the material performs in the cryogenic temperature range as a visible ratiometric thermometer, with a maximum sensitivity (S_m) of 6.08 \%K^{-1} at 12 K and relative sensitivities higher than 1 \%K^{-1} in the temperature range of 12 - 50 K (Fig 45b). However, the relative sensitivity at higher temperature is very small, reaching 0.3 \%K^{-1} at 100 K and 0.08 \%K^{-1} at 410 K.

For $\text{Na}[(\text{Gd}_{0.82}\text{Tb}_{0.135}\text{Eu}_{0.045})\text{SiO}_4]$ the determined relative thermal sensitivity shows a maximum sensitivity (S_m) of 1.92 \%K^{-1} at 14.4 K and relative sensitivities higher than 1 \%K^{-1} in the temperature range of 12-30 K (Fig 45b). However, the relative sensitivity at higher temperature is very small, reaching 0.2 \%K^{-1} at 100 K and 0.09 \%K^{-1} at 410 K.

Table 1: Representative cryogenic luminescent ratiometric thermometers; S_m is the maximum relative sensitivity at temperature T_m , ΔT is the temperature range with a relative sensitivity $S_r > 1.0 \text{ \%K}^{-1}$ for a specified temperature range [36].

Materials	$S_m (\text{ \%K}^{-1})$	$T_m (\text{ K})$	$\Delta T (\text{ K}) (S_r > 1.0 \text{ \%K}^{-1})$
$\text{Tb}_{0.95}\text{Eu}_{0.05}\text{HY}^{[a]}$	31.0	4	4–48

$\text{Eu}_{0.02}\text{Gd}_{0.98}(\text{dsb})^{[b]}$	7.14	65	20–35; 65–145
$\text{Na}[(\text{Gd}_{0.8}\text{Eu}_{0.1}\text{Tb}_{0.1})\text{SiO}_4]$	2.00	20	12–47
$[(\text{Tb}_{0.914}\text{Eu}_{0.086})(\text{pda})_3(\text{H}_2\text{O})] \cdot 2\text{H}_2\text{O}^{[c]}$	5.96	25	12–80
$[\text{Eu}_{0.102}\text{Tb}_{0.898}(\text{notpH}_4)(\text{NO}_3)(\text{H}_2\text{O})] \cdot 8\text{H}_2\text{O}^{[d]}$	3.90	38	18–245
$\text{Tb}_{0.95}\text{Eu}_{0.05}(\text{btb})$	2.85	14	14–177
$[\text{Tb}_{0.9}\text{Eu}_{0.1}(1,3\text{-bdc})_3(\text{H}_2\text{O})_2] \cdot \text{H}_2\text{O}$	3.30	36	12–101 K
$\text{Na}_2\text{K}[(\text{Lu}_{0.75}\text{Yb}_{0.20}\text{Er}_{0.05})_3\text{Si}_6\text{O}_{18}]$	2.60	27	12–86 K

$\text{Na}[(\text{Gd}_{0.82}\text{Tb}_{0.135}\text{Eu}_{0.045})\text{SiO}_4]$ is less efficient than $\text{Na}[(\text{Gd}_{0.666}\text{Tb}_{0.292}\text{Eu}_{0.042})\text{SiO}_4]$ regarding both S_m and S_r . So far seven cryogenic luminescent thermometer have been reported, their thermal sensitivity figures of merit are collected in table 2. $\text{Na}[(\text{Gd}_{0.82}\text{Tb}_{0.135}\text{Eu}_{0.045})\text{SiO}_4]$ is the less efficient cryogenic luminescent ratiometric thermometer reported concerning both S_m and S_r . In turn, regarding S_m , $\text{Na}[(\text{Gd}_{0.666}\text{Tb}_{0.292}\text{Eu}_{0.042})\text{SiO}_4]$ is only outperformed by two of the reported thermometers.

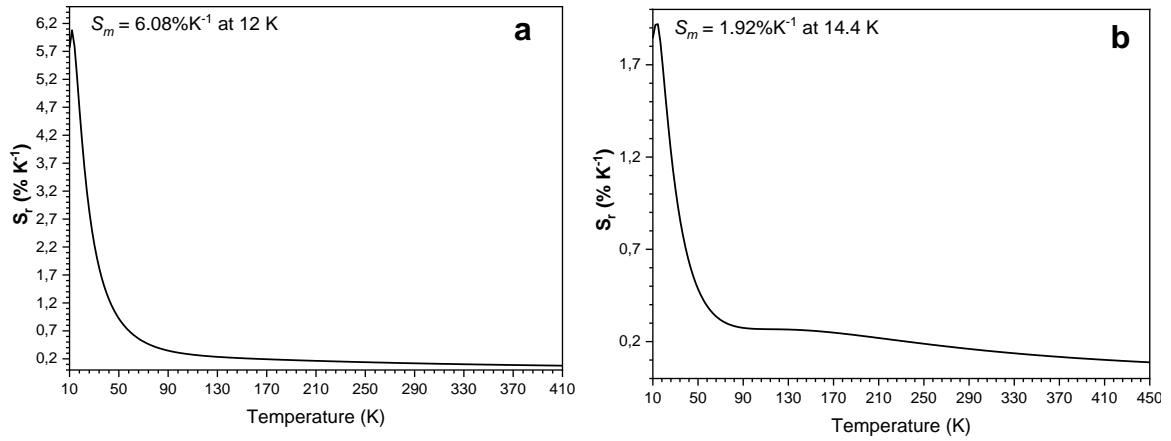


Figure 45: Relative thermal sensitivities from 12 K to 410 K for $\text{Na}[(\text{Gd}_{0.666}\text{Tb}_{0.292}\text{Eu}_{0.042})\text{SiO}_4]$ (a) and from 12 K to 450 K for $\text{Na}[(\text{Gd}_{0.82}\text{Tb}_{0.135}\text{Eu}_{0.045})\text{SiO}_4]$ (b).

Figure 46 and 47 show the $^5\text{D}_4$ decay and $^5\text{D}_0$ decay curves of $\text{Na}[(\text{Gd}_{0.82}\text{Tb}_{0.135}\text{Eu}_{0.045})\text{SiO}_4]$ and $\text{Na}[(\text{Gd}_{0.666}\text{Tb}_{0.292}\text{Eu}_{0.042})\text{SiO}_4]$ recorded at 294 K and 12 K. These curves were all fitted with second order exponential decay functions except for the $^5\text{D}_0$ decay curve of $\text{Na}[(\text{Gd}_{0.82}\text{Tb}_{0.135}\text{Eu}_{0.045})\text{SiO}_4]$ at 12 K. For $\text{Na}[(\text{Gd}_{0.666}\text{Tb}_{0.292}\text{Eu}_{0.042})\text{SiO}_4]$ (Fig. 46) the Tb^{3+} lifetime is equal to 0.36 ± 0.03 ms at 294 K and 1.22 ± 0.03 ms at 12 K. The lifetime is four times larger at 12 K than at room temperature due to the higher efficiency of Tb^{3+} -to- Eu^{3+} energy transfer at high temperature. The $^5\text{D}_0$ decay curves are very similar, with Eu^{3+} lifetimes of 0.91 ± 0.01 ms at 294 K and of 1.05 ± 0.01 ms at 12 K. The Tb^{3+} -to- Eu^{3+} energy transfer can be observed at the start of the curves, where a slight increase of the level population can be seen.

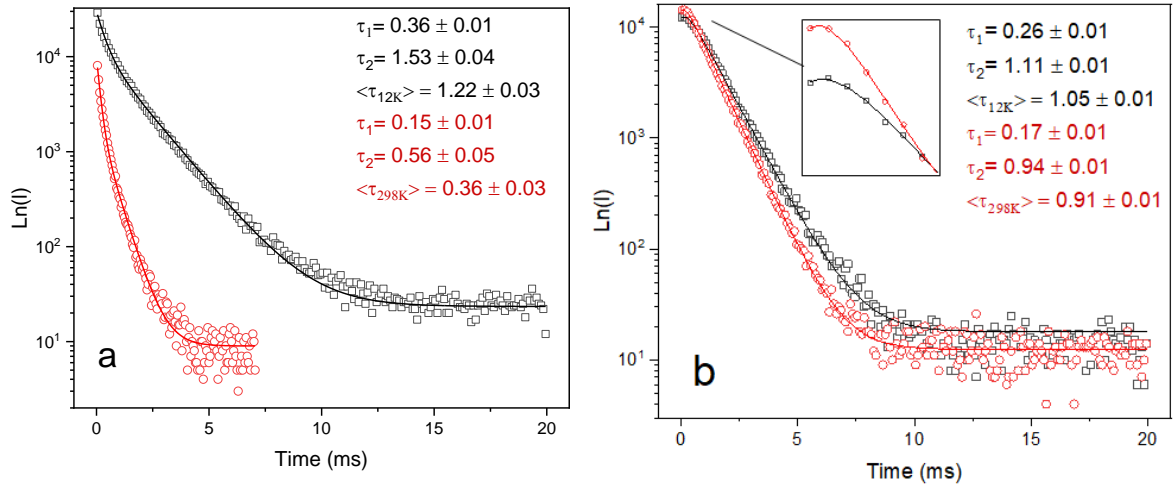


Figure 46: Decay curves of $\text{Na}[(\text{Gd}_{0.666}\text{Tb}_{0.292}\text{Eu}_{0.042})\text{SiO}_4]$ recorded at 543 nm (a), 5D_4 decay, and 614 nm (b), 5D_0 decay, with a fixed excitation at 375 nm. The black curves were measured at 12 K while the red ones at 294 K. The lines are best fits to first-order ($I = I_0 + A_1 e^{-x/\tau}$) and second-order ($I = I_0 + A_1 e^{-x/\tau} + A_2 e^{-x/\tau}$) decay functions. Average lifetime defined as $(A_1 \tau_1^2 + A_2 \tau_2^2)/(A_1 \tau_1 + A_2 \tau_2)$.

For $\text{Na}[(\text{Gd}_{0.82}\text{Tb}_{0.135}\text{Eu}_{0.045})\text{SiO}_4]$ (fig. 46), the Tb^{3+} lifetime is 1.05 ± 0.02 ms at 294 K and 1.66 ± 0.02 ms at 12 K. The lifetime is 1.7 times larger at 12 K than at room temperature due to the higher efficiency of Tb^{3+} -to- Eu^{3+} energy transfer at 294 K. The 5D_0 decay curves are very similar, with the Eu^{3+} lifetime of 1.02 ± 0.01 ms at 294 K and 1.17 ± 0.01 ms at 12 K.

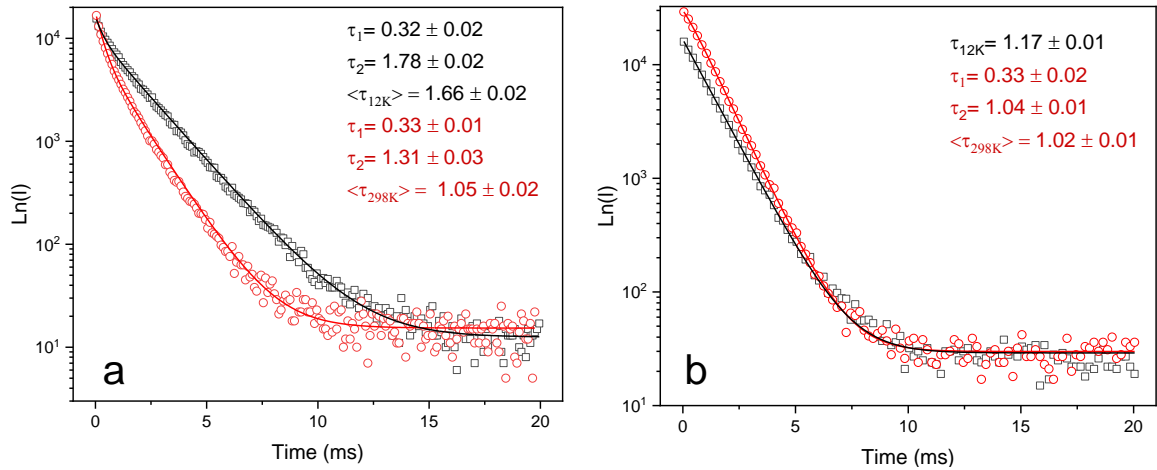


Figure 47: Decay curves of $\text{Na}[(\text{Gd}_{0.82}\text{Tb}_{0.135}\text{Eu}_{0.045})\text{SiO}_4]$ recorded at 543 nm (a), 5D_4 decay, and 614 nm (b), 5D_0 decay, with a fixed excitation at 375 nm. The black curves are the decay measured at 12 K while the red ones at 294 K. The lines are best fits to first-order ($I = I_0 + A_1 e^{-x/\tau}$) and second-order ($I = I_0 + A_1 e^{-x/\tau} + A_2 e^{-x/\tau}$) decay functions. Average lifetime defined as $(A_1 \tau_1^2 + A_2 \tau_2^2)/(A_1 \tau_1 + A_2 \tau_2)$.

The temperature sensing capability of the ratiometric $\text{Na}[(\text{Gd}_{0.666}\text{Tb}_{0.292}\text{Eu}_{0.042})\text{SiO}_4]$ and $\text{Na}[(\text{Gd}_{0.82}\text{Tb}_{0.135}\text{Eu}_{0.045})\text{SiO}_4]$ thermometers is due to the temperature dependence of the Tb^{3+} -to- Eu^{3+} energy transfer processes, occurring mainly via the dipole-quadrupole and quadrupole-quadrupole mechanism [25].

Considering a Förster-type multipolar mechanism, the efficiency, η_{ET} , and probability, k_{ET} , of the Tb^{3+} -to- Eu^{3+} energy transfer may be determined from the experimental donor (Tb^{3+}) lifetime in the presence (τ_{DA}) and in the absence of the acceptor Eu^{3+} (τ_D) [25]:

$$\eta_{ET} = 1 - \frac{\tau_{DA}}{\tau_D} \quad (12)$$

$$k_{ET} = \tau_{DA}^{-1} - \tau_D^{-1} \quad (13)$$

Considering the $^5\text{D}_4$ lifetimes measured in the presence and absence of the acceptor, respectively $\text{Na}[(\text{Gd}_{0.666}\text{Tb}_{0.292}\text{Eu}_{0.042})\text{SiO}_4]$ and $\text{Na}[(\text{Gd}_{0.9}\text{Tb}_{0.1})\text{SiO}_4]$ (fig. 38), an energy transfer efficiency and probability of, respectively, 40% and 334 s^{-1} at 12 K, and 80% and 2220 s^{-1} at 294 K are obtained. For $\text{Na}[(\text{Gd}_{0.82}\text{Tb}_{0.135}\text{Eu}_{0.045})\text{SiO}_4]$, an energy transfer efficiency and probability of, respectively, 29% and 117 s^{-1} at 12 K, and 41% and 394 s^{-1} at 294 K are obtained. Because the decay curves are biexponential, τ_{DA} is an average value. Those results match the relative thermal sensitivity obtained, $\text{Na}[(\text{Gd}_{0.666}\text{Tb}_{0.292}\text{Eu}_{0.042})\text{SiO}_4]$ have better efficiency and probability of energy transfer than $\text{Na}[(\text{Gd}_{0.666}\text{Tb}_{0.292}\text{Eu}_{0.042})\text{SiO}_4]$.

3.4.3 Infrared ratiometric luminescent thermometer

The compound $\text{Na}[(\text{Gd}_{0.85}\text{Yb}_{0.10}\text{Er}_{0.05})\text{SiO}_4]$ was also evaluated as an infrared ratiometric luminescent thermometer.

Fig. 48 depicts the Er^{3+} excitation spectra of $\text{Na}[(\text{Gd}_{0.85}\text{Yb}_{0.10}\text{Er}_{0.05})\text{SiO}_4]$ detecting the Er^{3+} near-infrared emission at room temperature and 12 K. The sharp lines are ascribed to the typical intra $4f^{11}$ Er^{3+} transitions, and to the $^2\text{F}_{7/2} \rightarrow ^2\text{F}_{5/2}$ Yb^{3+} transition (from 880 to 1000 nm) [33]. This clearly shows that, the Yb^{3+} -to- Er^{3+} energy transfer is much more efficient at room temperature than 12 K. The Yb^{3+} -to- Er^{3+} energy transfer arises between two resonant excited level, $^2\text{F}_{5/2}$ of Yb^{3+} and $^4\text{I}_{11/2}$ of Er^{3+} [33], leading to an efficient energy transfer. The line at 760 nm depicts the half order of the detection fixed at 1520 nm.

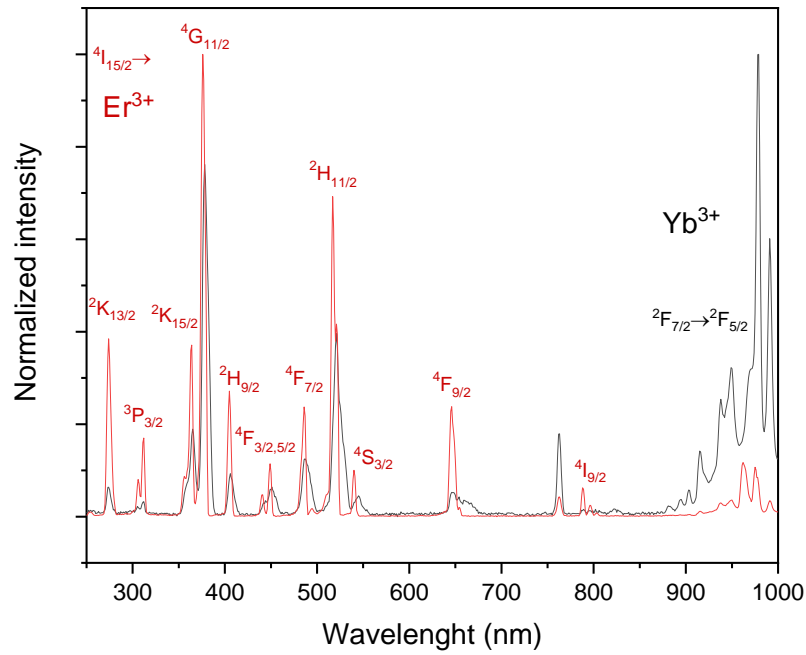


Figure 48: Excitation spectra of $\text{Na}[(\text{Gd}_{0.85}\text{Yb}_{0.10}\text{Er}_{0.05})\text{SiO}_4]$ at 294 K (black) and 12 K (red) with the emission fixed at 1520 nm.

Fig. 49 show the near-infrared emission spectra of $\text{Na}[(\text{Gd}_{0.85}\text{Yb}_{0.10}\text{Er}_{0.05})\text{SiO}_4]$ recorded at 294 K and 12 K. The emission lines are assigned to the ${}^2\text{F}_{7/2} \rightarrow {}^2\text{F}_{5/2}$ emission transition of Yb^{3+} and to the ${}^4\text{I}_{13/2} \rightarrow {}^4\text{I}_{15/2}$ emission transition of Er^{3+} . The latter significantly increases, relatively to the Yb^{3+} , upon raising the temperature from 12 K to 294 K due to the progressive thermal intensification of the Yb^{3+} -to- Er^{3+} energy transfer process.

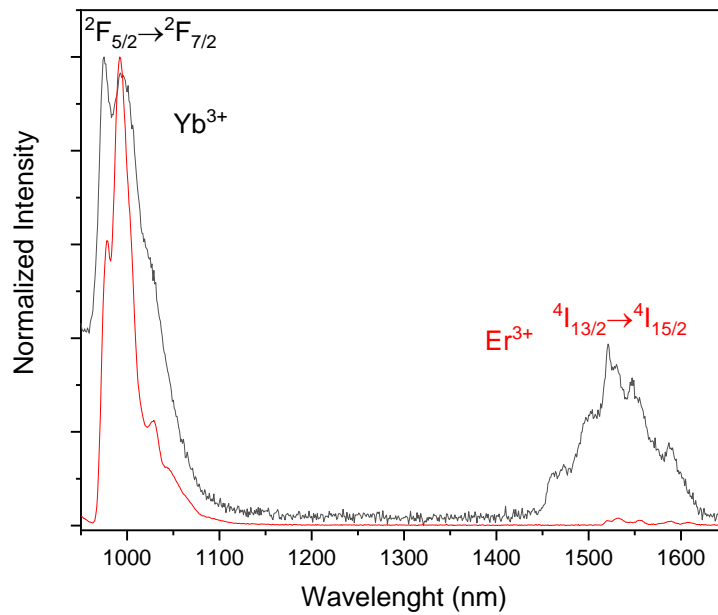


Figure 49: Emission spectra of $\text{Na}[(\text{Gd}_{0.85}\text{Yb}_{0.10}\text{Er}_{0.05})\text{SiO}_4]$ at 294 K (black) and 12 K (red) with the excitation fixed at 961 nm.

Then, we assessed the potential of $\text{Na}[(\text{Gd}_{0.85}\text{Yb}_{0.10}\text{Er}_{0.05})\text{SiO}_4]$ to be used as a near-infrared ratiometric luminescent thermometer. To do that, the integrated areas of the $^2\text{F}_{7/2} \rightarrow ^2\text{F}_{5/2}$ (I_{Yb}) and $^4\text{I}_{13/2} \rightarrow ^4\text{I}_{15/2}$ (I_{Er}) emissions were used to define the thermometric parameter $\Delta = I_{\text{Yb}} / I_{\text{Er}}$ and to convert the emission intensities into absolute temperature. The emission intensity was monitored in the range 12 - 390 K, with the excitation fixed at 916 nm, in the $^2\text{F}_{7/2}$ excited level of Yb^{3+} (fig. 50).

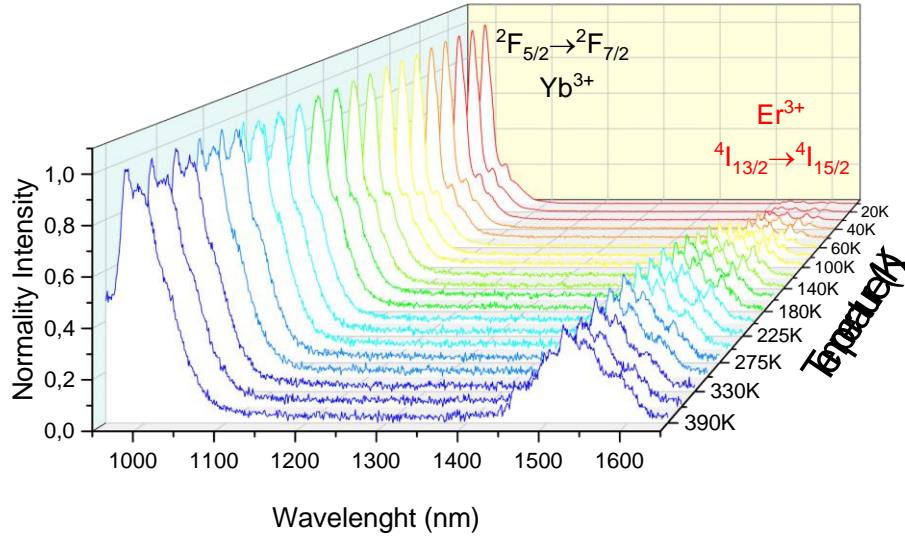


Figure 50: Emission spectra of $\text{Na}[(\text{Gd}_{0.85}\text{Yb}_{0.10}\text{Er}_{0.05})\text{SiO}_4]$ in the range 12 – 390 K with the excitation fixed at 916 nm.

To determine the average thermometric parameter, four consecutive emission spectra were collected at each temperature. The errors were calculated from the corresponding standard deviation. I_{Yb} and I_{Er} were calculated by integrating the emission spectra in the 950 - 1105 nm and 1444 - 1623 nm ranges, respectively. Figure 51 plots the I_{Yb} and I_{Er} temperature dependence. Yb^{3+} emission decreases with increasing temperature, the integrated emission attaining at 390 K 19% of the 12 K value. Er^{3+} emission increases drastically with temperature, reaching 27.5 times the 12 K value. The decrease of the Yb^{3+} emission and the drastic increase of the Er^{3+} emission is evidence for the Yb^{3+} -to- Er^{3+} energy transfer process.

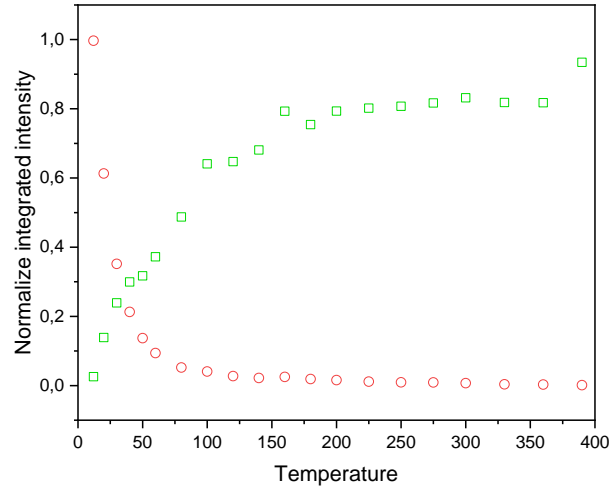


Figure 51 : Temperature dependence of the I_{Yb} (red) and I_{Er} (green) parameters of $Na[(Gd_{0.85}Yb_{0.10}Er_{0.05})SiO_4]$.

Fig. 52a depicts the temperature dependence of the thermometric parameter Δ in the range 12 – 390 K. The data is described by by a first-order classical Mott-Seitz model:

$$\Delta(T) = \frac{\Delta_0}{1 + \alpha \exp(-\Delta E/k_B T)} \quad (14)$$

The fit of the experimental Δ values with equation 14 yields $\Delta_0 = 47.62 \pm 0.72$; $\alpha = 23.03 \pm 0.76$; $\Delta E = 43.38 \pm 0.88 \text{ cm}^{-1}$. The non-radiative channel is characterized by the activation energy ΔE is associated to the Yb^{3+} -to- Er^{3+} energy transfer.

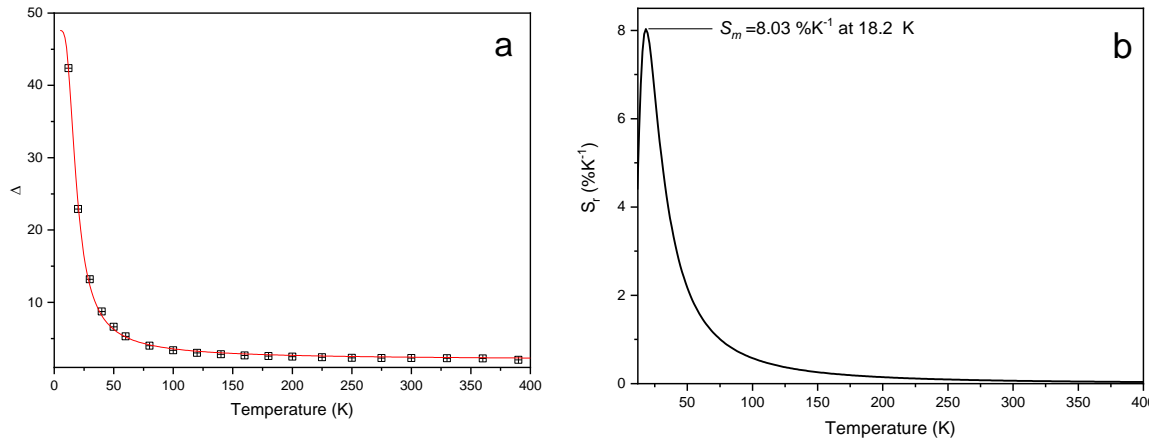


Figure 52: a) Temperature dependence of the parameter Δ from 12K to 390K for $Na[(Gd_{0.85}Yb_{0.10}Er_{0.05})SiO_4]$ excited at 916 nm. The solid line is the calibration curve, resulting from the fit considering a Mott-Seitz model. b) Corresponding relative thermal sensitivity in the same temperature range.

The determined relative thermal sensitivity (fig. 52b) shows that the material performs well in the cryogenic temperature range as a near-infrared ratiometric thermometer, with a maximum sensitivity (S_m) of $8.03 \%K^{-1}$ at 18.2 K and relative sensitivities higher than $1 \%K^{-1}$ in the temperature range of 12 - 75 K. However, as the infrared emitters, the relative sensitivity at higher temperature is small, reaching $0.15 \%K^{-1}$ at 200 K and $0.04 \%K^{-1}$ at 390 K.

From the seven cryogenic luminescent thermometers reported so far (table 2) and the two visible studied previously, only one outperforms $Na[(Gd_{0.85}Yb_{0.10}Er_{0.05})SiO_4]$ regarding S_m . Again, S_r is poor. However concerning the only two Ln-silicate cryogenic ratiometric thermometers, outperforms them both concerning S_m and S_r , even though for the only near-infrared cryogenic thermometer reported, S_r are very similar.

IV CONCLUSION

Lanthanide silicates are newly discovered structures, whose potential is still not fully evaluated. Their greatest potential lays in their optical properties, as structures emitting visible light, UV light and X-rays have been reported. This potential can be used in photoluminescent thermometry. An accurate and non-invasive thermometer is required in many fields and would greatly expand our understanding of numerous working processes. Lanthanide silicates hold promise to achieve for such a thermometer.

Experimental data show $\text{Na}[\text{LnSiO}_4]$ with $\text{Ln}=\text{Gd}, \text{Eu}, \text{Tb}$ or $\text{Gd}, \text{Er}, \text{Yb}$ is readily obtained by hydrothermal synthesis and its luminescence properties are promising. The best conditions to prepare the compound $\text{Na}[\text{LnSiO}_4]$ are: 1:1 to 5:1 for $\text{Si}:\text{Ln}$, 1:14 for $\text{Si}:\text{Na}$, and synthesis temperature and time 245 – 230 °C, 6 hours to 4 days. XRD, SEM, IR, Raman and NMR confirm the target $\text{Na}[\text{LnSiO}_4]$ with $\text{Ln}=\text{Gd}, \text{Eu}, \text{Tb}$ phase was obtained.

The study of the photoluminescence temperature dependence of $\text{Na}[\text{LnSiO}_4]$ shows this system holds promise for thermometry at cryogenic temperature. While $\text{Na}[(\text{Gd}_{0.82}\text{Tb}_{0.135}\text{Eu}_{0.045})\text{SiO}_4]$ performs very poorly when compared with other reported materials, the results are much better for $\text{Na}[(\text{Gd}_{0.666}\text{Tb}_{0.292}\text{Eu}_{0.042})\text{SiO}_4]$, outperforming the only reported visible Ln-silicate cryogenic luminescent ratiometric thermometer reported so far. Regarding the infrared ratiometric thermometer $\text{Na}[(\text{Gd}_{0.85}\text{Yb}_{0.10}\text{Er}_{0.05})\text{SiO}_4]$, it presents the best results in this study and outperforms the two Ln-silicate cryogenic luminescent ratiometric thermometer reported.

More experiments with different composition in gadolinium, erbium and yttrium should be done considering the results, but it would be necessary to improve the synthesis conditions to obtain pure samples.

Furthermore, the amount of europium/terbium used was between 15 to 35% comparable to the gadolinium amount, composition which was based on previous work on $\text{Na}[\text{LnSiO}_4]$ with $\text{Ln} = \text{Gd}, \text{Eu}, \text{Tb}$ in an orthorhombic structure [25]. Moreover, the photographs of the emission of our compounds with 10%, 50% and 100% Eu^{3+} show that the highest brightness is obtained with 50% europium. Therefore, further research on this compound with a higher amount of both europium and terbium is necessary.

This study also showed the possibility of tuning the optical properties in lanthanide silicates, by varying the ratio or the lanthanides themselves. More research is necessary to explore the full potential of photoluminescent lanthanides silicates.

V BIBLIOGRAPHY

- [1] G. Blasse and B. C. Grabmaier, *Luminescent Materials*. Berlin: Springer-Verlag, 1994.
- [2] D. A. Cleary, A. H. Francis, and E. Lifshitz, "Photoluminescence studies of layered transition metal phosphorus chalcogenides and their pyridine intercalation compounds," *J. Lumin.*, vol. 35, pp. 163–170, 1986.
- [3] Y. C. Lin, K. Delello, H. T. Zhang, K. Zhang, Z. Lin, M. Terrones, R. Engel-Herbert and J. A. Robison, "Photoluminescence of monolayer transition metal dichalcogenides integrated with VO₂," *J. Phys. Condens. Matter*, vol. 28, p 504001, 2016.
- [4] H. Maas, A. Currao, and G. Calzaferri, "Encapsulated lanthanides as luminescent materials," *Angew. Chemie - Int. Ed.*, vol. 41, pp. 2495–2497, 2002.
- [5] R. I. Laming, "Efficient Pump Wavelengths of Erbium Doped Fibre Optical Amplifiers," *Ieee*, vol. 25, pp. 12–14, 1989.
- [6] C. D. S. Brites, P. P. Lima, N. J. O. Silva, A. Millan, V. S. Amaral, F. Palacio and L. D. Carlos, "Lanthanide-based luminescent molecular thermometers," *New J. Chem.*, vol. 35, p. 1177, 2011.
- [7] J. R. Lakowicz, *Principles of Fluorescence Spectroscopy*, New York, Springer, 3rd edition, 2006.
- [8] J. Rocha, D. Ananias, and F. A. A. Paz, "Photoluminescent Zeolite-Type Lanthanide Silicates," *Compr. Inorg. Chem. II*, vol. 4, pp. 87–110, 2013.
- [9] S. S. Skourtis, C. Liu, P. Antoniou, A. M. Virshup, and D. N. Beratan, "Dexter energy transfer pathways," *Proc. Natl. Acad. Sci.*, vol. 113, pp. 8115–8120, 2016.
- [10] W. H. Fonger and C. W. Struck, "Eu+35D Resonance Quenching to the Charge-Transfer States in Y₂O₂S, La₂O₂S, and LaOCl," *J. Chem. Phys.*, vol. 52, pp. 6364–6372, 1970.
- [11] K. Binnemans, "Interpretation of europium(III) spectra," *Coord. Chem. Rev.*, vol. 295, pp. 1–45, 2015.
- [12] D. Ananias, A. Ferreira; L. Carlos, J. Rocha, C. M. Morais, "Novel microporous europium and terbium silicates," *J. Am. Chem. Soc.*, vol. 123, pp. 5735–5742, 2001.
- [13] B. R. Figueiredo, A. A. Valente, Z. Lin, and C. M. Silva, "Photoluminescent porous and layered lanthanide silicates: A review," *Microporous Mesoporous Mater.*, vol. 234, pp. 73–97, 2016.
- [14] D. Ananias, F. A. A. Paz, L. D. Carlos, and J. Rocha, "Photoluminescent microporous and layered lanthanide silicates," *Cienc. e Tecnol. dos Mater.*, vol. 24, pp. 134–137, 2012.
- [15] B. R. Figueiredo, M. M. R. de Melo, I. Portugal, D. Ananias, J. Rocha, and C. M. Silva, "Cs⁺ removal and optical detection by microporous lanthanide silicate Eu-AV-20 in a fixed-bed column," *Chem. Eng. J.*, vol. 286, pp. 48–58, 2016.
- [16] I. Dr. and M. Luqman, Eds., *Ion Exchange Technology I*. Dordrecht: Springer Netherlands, 2012.
- [17] C. D. S. Brites, A. Millán, and L. D. Carlos, "Lanthanides in Luminescent Thermometry," *Handb. Phys. Chem. Rare Earths*, vol. 49, pp. 339–427, 2016.
- [18] X. Wang, O. S. Wolfbeis, and R. J. Meier, "Luminescent probes and sensors for temperature," *Chem. Soc. Rev.*, vol. 42, p. 7834, 2013.
- [19] J. Rocha, C. D. S. Brites, and L. D. Carlos, "Lanthanide Organic Framework Luminescent

- Thermometers," *Chem. - A Eur. J.*, vol. 22, pp. 14782–14795, 2016.
- [20] B. R. Figueiredo, D. Ananias, I. Portugal, J. Rocha, and C. M. Silva, "Tb/Eu-AV-9: A lanthanide silicate for the sensing and removal of cesium ions from aqueous solutions," *Chem. Eng. J.*, vol. 286, pp. 679–688, 2016.
- [21] J. Rocha, P. Ferreira, L. D. Carlos, and A. Ferreira, "The first microporous framework cerium silicate," *Angew. Chemie - Int. Ed.*, vol. 39, pp. 3276–3279, 2000.
- [22] A. Ferreira, D. Ananias, L. D. Carlos, C. M. Morais, and J. Rocha, "Novel Microporous Lanthanide Silicates with Tobermorite-Like Structure," *J. Am. Chem. Soc.*, vol. 125, pp. 14573–14579, 2003.
- [23] H. K. Jeong, A. Chandrasekaran, and M. Tsapatsis, "Synthesis of a new open framework cerium silicate and its structure determination by single crystal X-ray diffraction," *Chem. Commun.*, pp. 2398–2399, 2002.
- [24] G. Wang, J. Li, K. Qian, J. Yu, and R. Xu, *A family of luminescent microporous lanthanide silicates*, vol. 170. Elsevier B.V., 2007.
- [25] D. Ananias, F. A. A. Paz, D. S. Yufit, L. D. Carlos, and J. Rocha, "Photoluminescent thermometer based on a phase-transition lanthanide silicate with unusual structural disorder," *J. Am. Chem. Soc.*, vol. 137, pp. 3051–3058, 2015.
- [26] A. Dakhlaoui, M. Toumi, L. S. Smiri, and A. Bulou, "Infrared and polarized Raman spectra of a noncentrosymmetric compound 'sodium samarium fluorosilicate' NaSmSiO₄·0.25NaF," *Spectrochim. Acta - Part A Mol. Biomol. Spectrosc.*, vol. 61, pp. 193–198, 2005.
- [27] B. Y. Gary, "Refinement of the Structure of 'Sodium Gadolinium Silicate', NaGdSiO₄·xNaOH (x ~ 0-2)," *Acta Cryst.*, vol. 36446, pp. 919–920, 1982.
- [28] E. I. Avetisyan, A. V. Chichagov, and N. V. Belov, "Crystal structure of sodium gadolinium orthosilicate," *Krystallografiya*, vol. 15, pp. 1066–1067, 1970.
- [29] E. I. Avetisyan, A. V. Chichagov, and N. V. Belov, "Crystal structure of sodium gadolinium orthosilicate," in *Krystallografiya*, 1970, pp. 1066–1067.
- [30] B. Mihailova, V. Valtchev, S. Mintova, and L. Konstantinov, "Vibrational spectra of ETS-4 and ETS-10," *Zeolites*, vol. 16, pp. 22–24, 1996.
- [31] G. D. Del Cul, S. E. Nave, G. M. Begun, and J. R. Peterson, "Raman Spectra of Tetragonal Lanthanide," *J. Raman Spectrosc.*, vol. 23, pp. 267–272, 1992.
- [32] S. Ferdov, R. A. Sá Ferreira, and Z. Lin, "Hydrothermal synthesis, structural investigation, photoluminescence features, and emission Quantum yield of Eu and Eu-Gd silicates with apatite-type structure," *Chem. Mater.*, vol. 18, pp. 5958–5964, 2006.
- [33] D. Ananias, A. A. Paz, L. D. Carlos, and J. Rocha, "Rare-Earth Germanate Visible, Near-Infrared, and Up-Conversion Emitters," *Eur. J. Inorg. Chem.*, pp. 1–9, 2018.
- [34] D. Ananias, M. Kostova, F. A. A. Paz, A. N. C. Neto, R. T. De Moura, and L. D. Carlos, "Molecule-Like Eu 3 + -Dimers Embedded in an Extended System Exhibit Unique Photoluminescence Properties," *J. Am. Chem. Soc.*, vol. 131, pp. 8620–8626, 2009.
- [35] W.-R. Liu, C. C. Lin, Y.-C. Chiu, Y.-T. Yeh, S.-M. Jang, R.-S. Liu and B.-M. Cheng, "Versatile phosphors BaY₂Si₃O₁₀:RE (RE = Ce³⁺, Tb³⁺, Eu³⁺) for light-emitting diodes," *Opt. Express*, vol. 17, pp. 18103–9, 2009.
- [36] D. Ananias, F. A. A. Paz, L. D. Carlos, and J. Rocha, "Near-Infrared Ratiometric Luminescent Thermometer Based on a New Lanthanide Silicate," in *submitted*, .

VI ANNEXES

6.1 CRYSTAL DATA

Table 2: Crystal data of NaGdSiO₄.

Crystal data		Atom	Ox.	Wyck.	x	y	z
Formula sum	NaGdSiO ₄	Gd1	+3	8h	0.18400	0.11700	0
Crystal system:	tetragonal	Si1	+4	8h	0.10600	0.24600	1/2
Space group:	I 4/m (no. 87)	Na1	+1	8h	0.42000	0.10900	1/2
Unit cell dimensions:	$a = 11.6300 \text{ \AA}$	O1	-2	8h	0.38500	0.11300	0
	$c = 5.4100 \text{ \AA}$	O2	-2	8h	0.24000	0.21000	1/2
		O3	-2	16i	0.04100	0.19000	0.260

6.2 SYNTHESIS

- Synthesis A:

Table 3: Synthesis conditions of the compounds synthesized at different temperatures.

	Sodium silicate solution (SSS) (g)	Water (g)	NaOH (g)	Tb (0.5 mol/mL)	Eu (0.5mol/mL)	Gd (0.4mol/mL)	Oven temperature (°C)
CMEuTb32	4.42	5.12	5.09	0.6	0.2	4	150
CMEuTb20	2.23	2.54	2.85	0.3	0.1	2	180
CMEuTb21	2.20	2.54	2.82	0.3	0.1	2	230
CMEuTb22	2.20	2.53	2.92	0.3	0.1	2	245

Synthesis were carried out in 12 mL and 21 autoclaves, synthesis time 4 days.

- Synthesis B:

Table 4: Synthesis conditions of the compounds synthesized with different oven times.

	SSS (g)	Water (g)	NaOH (g)	Tb (0.5 mol/m)	Eu (0.5mol)	Gd (0.4mol)	Oven time
--	---------	-----------	----------	----------------	-------------	-------------	-----------

				L)	/mL)	/mL)	
CMEuTb38	4.45	5.11	5.71	0.6	0.2	4	1 hour
CMEuTb37	4.41	5.11	5.7	0,6	0.2	4	6 hours
CMEuTb35	2.26	2.54	2.89	0.3	0.1	2	1 days
CMEuTb36	2.25	2.55	2.93	0.3	0.1	2	2 days
CMEuTb17	4.46	5.10	5.83	0.6	0.2	4	3 days
CMEuTb18	4.43	5.12	5.81	0.6	0.2	4	4 days
CMEuTb19	4.46	5.19	5.75	0.6	0.2	4	7 days

Synthesis were carried out in 21 mL and 12 mL autoclaves at 245 °C.

- Synthesis C:

Table 5: Synthesis conditions of the compounds synthesized with different Si:Ln ratios.

	SSS (g)	Water (g)	NaOH (g)	Tb (0.5 mol/mL)	Eu (0.5mol/mL)	Gd (0.4mol/mL)	Ratio Si:Ln
CMEuTb41	0.23	5.10	5.71	0.6	0.2	4	1:4
CMEuTb40	0.44	5.13	5.66	0.6	0.2	4	1:2
CMEuTb39	0.93	5.09	5.71	0.6	0.2	4	1:1
CMEuTb30	1.81	5.09	5.67	0.6	0.2	4	2:1
CMEuTb29	2.71	5.08	5.72	0.6	0.2	4	3:1
CMEuTb28	3.62	5.21	5.83	0.6	0.2	4	4:1
CMEuTb27	4.41	5.10	5.74	0.6	0.2	4	5:1

Synthesis were carried out in 21 mL and 12 mL autoclaves at 245°C for 4 days.

- Synthesis D:

Table 6: Synthesis conditions of the compounds synthesized with different Si:Na ratios.

	SSS (g)	Water (g)	NaOH (g)	Tb (0.5 mol/mL)	Eu (0.5mol/mL)	Gd (0.4mol/mL)	Ratio Si:Na
CMEuTb14	4.43	5.10	5.86	0.6	0.2	4	1:14
CMEuTb15	4.43	5.23	5.25	0.6	0.2	4	1:13
CMEuTb16	4.39	5.11	4.66	0.6	0.2	4	1:12
CMEuTb33	4.44	5.11	4.28	0.6	0.2	4	1:10
CMEuTb34	4.39	5.08	3.74	0.6	0.2	4	1:9

Synthesis were carried out in 21 mL autoclaves at 245°C for 4 days.

- Synthesis E:

Table 7: Synthesis conditions of the compounds synthesized with different Gd:Eu:Tb ratios.

	SSS (g)	Water (g)	NaOH (g)	Tb (0.5 mol/mL)	Eu (0.5mol/mL)	Gd (0.4mol/mL)	Gd/Eu/Tb
CMEuTb5	4.38	5.16	5.86	0.72	0.72	3.60	66.6/16.7/16.7
CMEuTb6	4.40	5.16	5.68	0.36	0.36	4.05	82/9.0/9.0
CMEuTb7	4.39	5.19	5.70	0.54	0.18	4.05	82/4.5/13.5
CMEuTb8	4.39	5.12	5.86	1.26	0.18	3.60	66.6/4.2/29.2
CMEuTb23	4.43	5.09	5.82	0.48	0.16	4.20	84/4/12
CMEuTb24	4.42	5.09	5.73	0.60	0.20	4.00	80/5/15
CMEuTb25	4.38	5.16	5.73	0.67	0.13	4.00	80/3,3/16,7
CMEuTb26	4.42	5.08	5.72	0.40	0.20	4.25	85/5/10

Synthesis were carried out in 21 mL and 12 mL autoclaves at 245°C for 4 days.

- Synthesis F:

Table 8: Synthesis conditions of the compounds synthesized with different Gd:Er:Yb ratios.

	SSS (g)	Water (g)	NaOH (g)	Yb (0.4)	Er (0.4)	Gd	Gd/Er/Yb
--	---------	-----------	----------	----------	----------	----	----------

				mol/mL)	mol/mL)	(0.4/mL)	
CMErYb5	1.83	5.10	5.66	0.75	0.25	3.2	80/5/15
CMErYb6	1.81	5.10	5.63	0.80	0.20	3.2	80/4/16
CMErYb7	1.82	5.09	5.77	0.62	0.34	3.2	80/6,67/12.33
CMErYb8	1.85	5.12	5.79	0.5	0.25	3.4	85/5/10

Synthesis were carried out in 21 mL autoclaves at 245°C for 4 days.

- Synthesis G:

Table 9: Synthesis conditions of the compounds NaYSiO₄.

	SSS (g)	Water (g)	NaOH (g)	Y (0.4 mol/mL)	Si:Ln ratio
CMY1	4.40	5.08	5.80	5	5:1
CMY2	1.82	5.08	5.71	5	2:1

Synthesis was carried out in 21 mL autoclaves at 245°C for 4 days.